Modelling and Validation of Slit-Homogenizers for Space-Based Imaging Spectrometers

Modellierung und Validierung von Spalt-Homogenisierern für

weltraumgestütze abbildende Spektrometer

Timon Fabian Hummel

Fakultät für Physik

Modelling and Validation of Slit-Homogenizers for Space-Based Imaging Spectrometers

Modellierung und Validierung von Spalt-Homogenisierern für
weltraumgestütze abbildende Spektrometer

Timon Fabian Hummel

Dissertation

an der Fakultät für Physik

der Ludwig–Maximilians–Universität

München

vorgelegt von

Timon Fabian Hummel

aus Freiburg

München, den 25.04.2022

Erstgutachter: Prof. Dr. Mark Wenig

Zweitgutachter: Prof. Dr. Thomas Birner

Tag der mündlichen Prüfung: 17.06.2022

Abstract

Increasing recent demands for climate awareness require accurate measurement and monitoring of the atmospheric composition. A suitable method for this is the measurement via spaceborne passive imaging spectrometers. The analysis of Earth radiance spectra allows to determine the concentration of absorbing gases in the atmosphere. The measurement accuracy of recent and future spaceborne imaging spectrometers with a high spectral and spatial resolution suffers from the inhomogeneity of the radiance of the observed Earth scene. The scene heterogeneity creates a pseudo-random deformation of the instrument's spectral response function (ISRF), which is the direct link between the forward radiative transfer model, used to retrieve the atmospheric state, and the radiance measured by the instrument. Consequently, heterogeneous scenes will degrade the precision of the retrieved column concentration of the atmospheric components. The present thesis aims to investigate a hardware solution called slit homogenizer (SH), which is used to mitigate the impact of heterogeneous scenes. Several new design considerations, performance predictions and further implications of employing a SH are presented. First, a mirror-based 1D-slit homogenization solution (1DSH) that homogenizes the scene in along-track direction is investigated. To this end, the performance of the 1DSH is modelled by a comprehensive propagation model based on scalar diffraction theory. In the context of the Sentinel-5/UVNS mission, the specific mission requirements on spectral accuracy with respect to applicable heterogeneous scene test cases are evaluated for the 1DSH.

Second, a next-generation SH concept based on waveguides is presented. In the context of the upcoming CO_2 Monitoring Mission (CO2M), a slit concept based on rectangular optical fibres is investigated. In this concept, the scene heterogeneity is scrambled in both along-track direction and across-track direction and is therefore referred to as 2D-Slit Homogenizer (2DSH). Particular emphasis is put on the study of the influence of the length and arrangement of the fibres on the scrambling performance. A specific bending routine is proposed to homogenize the far field after the fibre, which further stabilizes the spectral performance. Replacing a

classical slit by a 2DSH also changes other than spectral aspects of the instrument like modified signal-to-noise ratios or co-registration schemes.

Finally, using the 1DSH as an example, the impact of the stabilized spectral performance in the UV-VIS spectral range on the accuracy of the retrieved NO_2 column density is investigated. For this, the artificially generated heterogeneous Earth radiance scene is propagated through a model of the Sentinel-5/UVNS instrument. The instrument propagation was performed for an instrument equipped with a SH and one with a classical slit. The resulting deviation in the retrieved column density from the ground truth is compared for both cases. The result of the enhanced retrieval accuracy underlines the advantages of employing a SH in spaceborne imaging spectrometers.

Kurzfassung

Die zunehmenden aktuellen Anforderungen an die Erfassung wichtiger Klimaparameter erfordern eine genaue Messung und Überwachung der atmosphärischen Zusammensetzung. Eine geeignete Methode hierfür ist die Messung mit weltraumgestützten passiven abbildenden Spektrometern. Mit Hilfe der von der Erde reflektierten Spektren lässt sich die Konzentration der absorbierenden Gase in der Atmosphäre bestimmen. Die Messgenauigkeit aktueller und künftiger weltraumgestützter abbildender Spektrometer mit hoher spektraler und räumlicher Auflösung leidet unter der Heterogenität der Radianz der beobachteten Erdszene. Die Heterogenität der Szene führt zu einer pseudo-zufälligen Deformierung der spektralen Pulsantwort des Instruments (ISRF), die das Strahlungstransportmodell, das zur Rekonstruktion der atmosphärischen Parameter verwendet wird, mit der vom Instrument gemessenen Strahldichte verknüpft. Infolgedessen beeinträchtigen heterogene Szenen die Genauigkeit der ermittelten Säulenkonzentrationen der atmosphärischen Komponenten. In der vorliegenden Arbeit soll eine Hardware-Lösung namens Slit Homogenizer (SH) untersucht werden, die verwendet wird, um die Auswirkungen heterogener Szenen abzuschwächen. In dieser Arbeit werden mehrere neue Designüberlegungen, Effizienzvorhersagen und weitere Implikationen des Einsatzes eines SH vorgestellt. Zunächst wird eine spiegelbasierte 1D-Slit Homogenizer (1DSH) Lösung untersucht, die die Erdszene entlang der Flugrichtung des Satelliten homogenisiert. Dazu wird die Effizienz des 1DSH durch ein umfassendes Propagationsmodell auf der Grundlage skalarer Beugungstheorie modelliert. Im Kontext der Sentinel-5/UVNS-Mission werden die spezifischen Anforderungen der Mission an die spektrale Genauigkeit in Bezug auf mehrere relevenate heterogenen Szenen für den 1DSH evaluiert.

Anschließend wird ein weiteres SH-Konzept vorgestellt, das auf optischen Wellenleitern basiert. Im Kontext der bevorstehenden CO_2 Monitoring Mission (CO2M) wird ein Spaltkonzept auf der Basis von rechteckigen optischen Fasern untersucht. Dieses Konzept mischt die Heterogenität der Szene sowohl entlang der Flugrichtung des Satelliten als auch senkrecht dazu und wird daher als 2D-Slit Homogenizer (2DSH)

bezeichnet. Insbesondere wird der Einfluss von Länge und Anordnung der Fasern auf die Homogenisierung der Szenen untersucht. Es wird eine spezielle Krümmung der Fasern vorgeschlagen, um das Fernfeld nach der Faser zu homogenisieren, was die spektrale Pulsantwort des Instruments weiter stabilisiert. Das Ersetzen eines klassischen Spalts durch einen 2DSH führt zu weiteren Konsequenzen für das Instrument, wie z.B. veränderte Signal-Rausch-Verhältnisse oder neue Methoden der co-Registrierung.

Als letztes wird am Beispiel des 1DSH die Auswirkung der stabilisierten spektralen Leistung des Instruments auf die Genauigkeit der berechneten NO_2 Säulenkonzentration im UV-VIS-Wellenlängenkanal untersucht. Zu diesem Zweck wird eine künstlich erzeugte heterogene Erdszene durch ein Modell des Sentinel-5/UVNS-Instruments propagiert. Die Instrumentenpropagation wurde für ein mit SH ausgestattetes Instrument und ein Instrument mit einem klassischen Spalt durchgeführt. Die aus der heterogenen Szene resultierende Abweichung der berechneten Säulenkonzentration von der tatsächlichen Säulenkonzentration wird für beide Fälle verglichen. Das Ergebnis der verbesserten Übereinstimmung zwischen berechneter und tatsächlicher Säulenkonzentration für ein Instrument mit SH unterstreicht die Vorteile der Verwendung eines SH in weltraumgestützten abbildenden Spektrometern.

Contents

List of Figures

List of Tables

List of publications

Parts of the content presented in this thesis have been published in the following articles:

Hummel, T., Meister, C., Keim, C., Krauser, J., and Wenig, M.: Slit homogenizer introduced performance gain analysis based on the Sentinel-5/UVNS spectrometer, Atmospheric Measurement Techniques, 14, 5459–5472, doi: 10.5194/amt-14-5459-2021, 2021b

Hummel, T., Coatantiec, C., Gnata, X., Lamour, T., Riviere, R., Riviere, C., Krauser, J., Weise, D., and Wenig, M.: Experimental validation of a 2D-slit homogenizer for space based imaging spectrometers, in: International Conference on Space Optics — ICSO 2020, edited by Cugny, B., Sodnik, Z., and Karafolas, N., vol. 11852, pp. 254 – 262, International Society for Optics and Photonics, SPIE, 2021a

Hummel, T., Coatantiec, C., Gnata, X., Lamour, T., Rivière, R., Meister, C., Stute, A., Krauser, J., Weise, D., and Wenig, M.: A fibre-based 2D-slit homogenizer concept for high-precision space-based spectrometer missions, CEAS Space Journal, doi: 10.1007/s12567-021-00419-8, 2022

1   Introduction

Since the beginning of industrialization, humans have been changing the natural composition of the atmosphere and the underlying processes that govern the Earth's system. The system is a complex interaction of various chemical, physical and biological processes and its delicate balance is paramount for the life on Earth. The steady growth of the global population and the increasing urbanization resulted in an appreciable deterioration of air quality. According to the World Health Organization (WHO), the poor air quality causes millions of deaths and lost years of healthy life annually (WHO, 2021). The source of the pollution is a result of the increasing economic and industrial development, combustion processes in the transport sector as well as coal fired power plants. Some trace gases in the atmosphere are also required to maintain habitable conditions on the Earth such as the ultra-violet-protecting ozone layer. The amount of ozone (O_3) in the atmosphere is vital to shield the Earth from incoming highly energetic ultra-violet radiation. In the mid-1970s it was discovered that due to the emission of ozone-depleting substances (ODS), the O_3 layer is depleted globally (Fahey and Hegglin, 2011). ODS summarize a set of manufactured chemicals, as for example chlorofluorocarbons, which are catalysing the conversion of O_3 into O_2. Besides the decreasing global ozone concentration another effect was observed. In a recurring event within a few weeks in springtime, the O_3 concentration in Antarctica over the south pole collapses and recovers within a few months. This is caused by the reaction of pollutants stored on the ice crystals of stratospheric clouds, which then evaporate with the ozone after the long cold polar night. This phenomenon became known as the Antarctic ozone hole and was first discovered by Farman et al. (1985). After successfully banning ODS in the frame of the Montreal Protocol (UNO, 1993) and its amendments, the O_3 layer is recovering. However, due to the long lifetime of some ODS it will take decades until the ozone layer is fully restored. Another vivid reminder of the vulnerability of the Earths ecosystem is climate change. Due to human activities, the atmospheric concentration of carbon dioxide (CO_2), methane

(CH_4) and other greenhouse gases (GHG) has been substantially increased. The growth of the GHG concentration causes an unequivocal change of the Earth's energy flux induced by positive radiative forcing, i.e. Earth receives more incoming energy than it releases into space. This causes more and more visible and threatening phenomena such as warming and rising oceans, diminished ice on the poles and glaciers as well as global warming. Compared to levels prior to the industrial age, the atmospheric CO_2 and CH_4 concentrations increased by 47% and 156% respectively (IPCC, 2021). Among other effects, this leads to a global increase of temperature of estimated $1.1°C$ since 1850, unprecedented global mean sea level rising and average Arctic sea ice area reaching its lowest since at least 1850. These alarming signals of the Earth's ecosystem make the reduction of GHG emissions one of the most important social and environmental issues of the 21st century.

Measuring and monitoring the changes in the Earth system and the impact that human activities has on its delicate balance is of paramount importance. In particular the observation by satellite-based remote sensing from space offers several crucial advantages. In order to provide policy makers and communities actionable information on the effectiveness of their measures to reduce human emissions, accurate quantification on various spatial scales are required. Compared to ground-based monitoring stations, satellite-based missions have the advantage of high spatial resolution and a global coverage necessary to monitor and track trace gas emissions on a global scale. In order to do so, several mission concepts are possible. Besides active ways of measuring the atmospheric composition from space with active light sources such as Light Detection and Ranging (LIDAR) instruments, passive remote-sensing payloads have been widely developed. This thesis focusses particularly on passive grating-based imaging spectrometers and effects that occur in them.

The measurement principle of push-broom Earth observation platforms relies on capturing sunlight reflected from the Earth surface. In order to cover the most prominent absorbing molecules of our atmosphere, the spectral window of recent Earth observation missions ranges from the ultraviolet ($\sim$270 nm) to the short

wave infrared ($\sim$2350 nm). This range is particularly interesting as in this spectral window the atmosphere is not opaque and therefore provides information of the absorption magnitude and consequently concentration of the molecules. Figure 1.1a
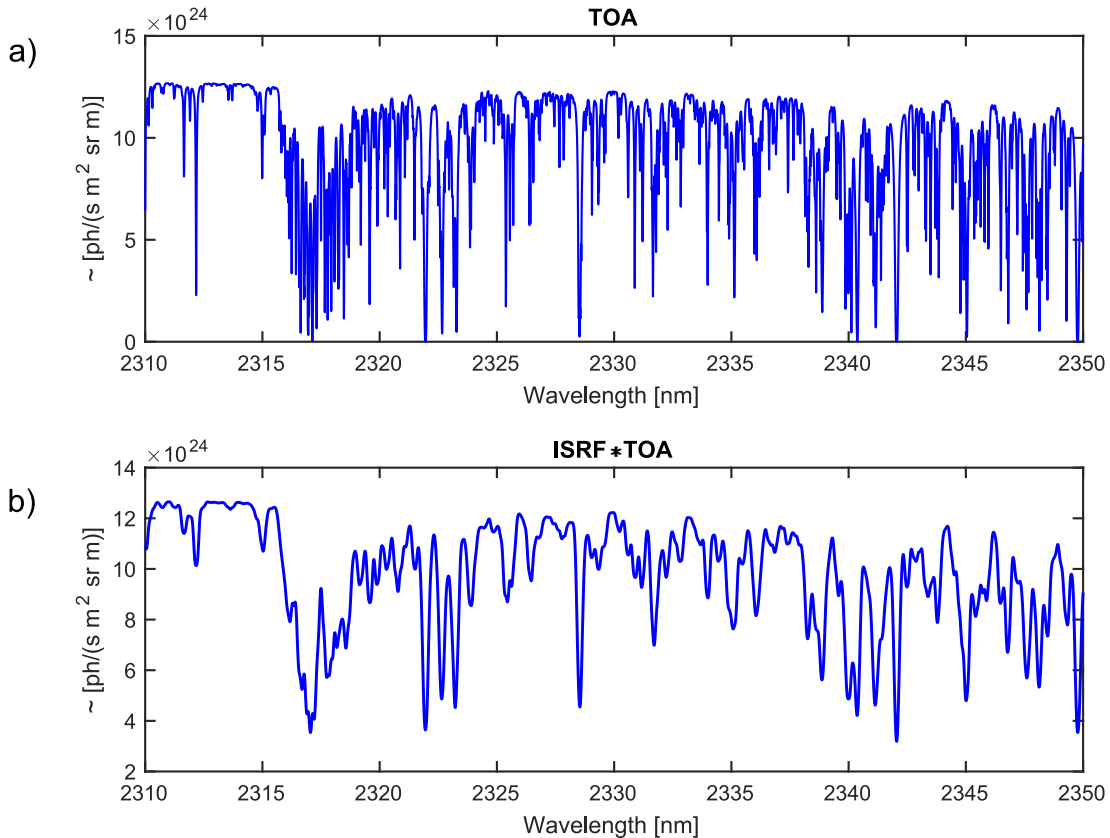
Figure 1.1: (a) High-resolution Earth top-of-atmosphere (TOA) spectrum as it would enter a spaceborne instrument in the short wave infrared (SWIR) channel. The spectrum represents the Earth radiance and accounts for the absorption features of the molecules therein. The structure in the depicted spectral window originates from the absorbing molecules CH_4, CO, and H_2O. (b) Spectrum convolved with a constant Instrument Spectral Response Function (ISRF). Any instability in the ISRF has an immediate impact on the captured spectrum and hence on the concentration measurement accuracy of the trace gases. Adapted from Hummel et al. (2021b).

depicts a representative simulated high-resolution spectrum as it would arrive at a spaceborne instrument in the short wave infrared (SWIR). The Earth top-of-atmosphere (TOA) spectrum was simulated with a solar zenith angle of 10° and

a surface albedo of 0.05 at infinite spectral resolution. The structures present in the spectrum originate from the absorption features of CH_4, CO and H_2O. During the measurement process of the instrument, the high-resolution spectrum will be influenced by the Instrument Spectral Response Function (ISRF). The ISRF describes the spectral response of an instrument to a monochromatic stimulus and is a key quantity of slit-based spectroscopy. The ISRF is determined by optical properties of the instrument, such as entrance slit illumination, spectrometer point spread function and detector properties. It establishes a direct link between the forward radiative transfer model of the retrieval algorithm and the spectra captured by the instrument (see section 6). Consequently, any instability or uncertainty of the ISRF leads to an immediate impact on the measured gas concentration accuracy.

The Ozone Monitoring Instrument (OMI) was the first instrument that recognized a spurious effect on the measured spectra caused by heterogeneous slit illumination (Voors et al., 2006b). Heterogeneous slit illumination can be induced by variations in the atmospheric layer properties by clouds or aerosols as well as variations of the ground albedo. Since then, the influence of inhomogeneous Earth scenes has been an integral part of the performance and design requirements of subsequent spectrometer missions. Landgraf et al. (2016) assessed the impact of heterogeneous illumination of the instrument entrance slit for the Tropospheric Monitoring Instrument (TROPOMI) on board the Copernicus Sentinel-5 Precursor satellite (launched 2017). They characterize errors for vertically integrated column density CO biases with up to 2 %. On larger spatial scales, this error usually manifests itself with pseudo-random characteristics. Hu et al. (2016) concluded that of all instrument errors, instabilities in the ISRF are the largest error contributors to the CH_4 retrieval of the Tropomi mission. Noël et al. (2012) quantified the impact of heterogeneous scenes on the Sentinel-4 UVN imaging spectrometer data products, namely tropospheric O_3, NO_2, SO_2, and HCHO. They observe significant tropospheric column errors with up to 5 % mean error, 50 % maximum error, and 8 % standard deviation of the errors.

To some extent and in certain wavelength regimes, this effect of heterogeneous scenes can be compensated by software correction algorithms based on temporally oversampled data containing information about the heterogeneity of the scene. However, for particularly strong molecular absorption bands, as typically and predominantly occur in the SWIR, such software correction fails. For this reason, among others, a new possibility of correction was investigated in the form of a hardware solution. The upcoming Sentinel-5/UVNS (Ultraviolet/Visible/Near-infrared/SWIR) (Irizar et al., 2019) instrument is the first spaceborne push-broom spectrometer that employs an on-board concept to mitigate the effect of hetero-geneous scenes in the direction of the satellite motion. The hardware solution is called slit homogenizer (SH) and replaces the classical spectrometer entrance slit with a pair of two parallel extended mirrors, which effectively scramble the scene radiance contrast in along-track direction (ALT). As the SH is not affecting the imaging in across-track direction (ACT) it is also called 1D Slit Homogenizer (1DSH). Compared to previous instruments that relied only on software correction, the 1DSH effectively removes the heterogeneity from the Earth radiance scene. However, due to complex interference effects of the coherent light inside the SH, the 1DSH cannot perfectly homogenize the scene.

The upcoming CO_2 Monitoring Mission (CO2M) (Sierk et al., 2021) aims to quantify sources and sinks of CO_2 and CH_4 by measuring their concentration in the atmosphere. Identifying plumes of elevated CO_2 requires high single-sounding precision without regional and temporal averaging (Kuhlmann et al., 2020). The stringent precision and accuracy corresponds to only 0.1% of today's typical CO_2 background values around $400\,\mathrm{ppm}$. Along with the small ground sampling distance ($2\,\mathrm{km}$) corresponding to a significant fraction of the instantaneous field of view (IFOV) in ALT direction, this leads to a higher sensitivity of the CO2M mission to ISRF distortion than atmospheric chemistry missions like Sentinel-5/UVNS. For this reason, CO2M uses a next generation technology of SH, called 2D-Slit Homogenizer (2DSH). In this concept the classical entrance slit is replaced by a bundle of rectangular core multimode fibres. Besides other advantages, the

unprecedented scrambling properties of multimode fibres allows to almost perfectly desensitize the instrument for radiometric and spectral errors with respect to the heterogeneity of the Earth scene radiance.

This thesis adds to the discourse on the application and development of the SH technology two individual case studies, which aim to model the performance of currently existing SH for spaceborne applications. The thesis begins with an introduction to the fundamental concepts of push-broom imaging spectrometers (section 2.1). After introducing and describing the instrument spectral response function (ISRF) as one of the key parameters in imaging spectrometers in section 2.2, the impact of heterogeneous scenes on the ISRF stability is discussed in section 2.3. Section 3 summarizes the theoretical mathematical prerequisites for describing the light propagation through the optical instruments. A comprehensive performance prediction model of the 1DSH based on Huygens-Fresnel diffraction theory is presented in section 4. The achievable ISRF stability is simulated with respect to several input scenes (section 4.3) and the impact of second-order effects is discussed and quantified (section 4.4). A second SH concept based on fibre waveguides is outlined in section 5. The proposed SH concept contains trade-offs on the fibre size, the fibre configuration and signal-to-noise (SNR) considerations. In section 6, the 1DSH performance model is used to simulate the measurement process using the Sentinel-5/UVNS instrument as an example. The improved accuracy of the retrieved NO_2 column density is evaluated. Finally, section 7 summarizes the results of the thesis and holds the conclusion drawn from this work as well as an outlook on the development of SHs.

2 Push-broom imaging spectrometer

This work deals specifically with push-broom scanning methods, although the methods are generally applicable to whisk broom scanning concepts as well. In this section, the general concept of hyperspectral push-broom imaging spectrometers is presented. First, the basic measurement procedure is described in section 2.1. Afterwards, the ISRF is introduced as a key quantity in spectrometers. In section 2.3 the impact of heterogeneous scenes on the stability of the ISRF in push-broom imaging spectrometers is discussed and motivates the necessity for mitigation techniques.

2.1 Instrument principle

To detect and analyze the Earth's spectral radiance, a grating based push-broom imaging concept is an effective way. This technique has been widely used to analyze the Earth radiance in the solar bands and has a lot of heritage of previous Earth observation missions such as the OMI mission (Levelt et al., 2018) launched in 2015, the Sentinel-5 Precursor (S5P) (Veefkind et al., 2012) launched in 2017 or the upcoming Sentinel-5/UVNS instrument (Irizar et al., 2019) and CO2M mission (Sierk et al., 2021). Push-broom spectrometer are used for passive remote sensing and record the electromagnetic field that is reflected from the surface of the Earth. The measurement principle is illustrated in fig. 2.1. The Earth ground scene is imaged by a telescope onto the entrance slit of the spectrometer. The projection of the slit on-ground in ACT defines the swath width, which corresponds to the spatial coverage of the instrument. After the slit, the light is collimated, and the slit image perpendicular to the satellite's flight motions is spectrally dispersed by a dispersive element, such as a diffraction grating or prism. The slit is finally imaged on a 2D sensor referred to as the focal plane array (FPA). The slit width in conjunction with the spectral dispersion of the spectrometer determines the spectral resolution. A 2D image of the Earth is created by exploiting the satellite platform motion in ALT. The distance covered by the satellite during the image

sensor exposure time defines the spatial sampling distance in ALT. The spatial sampling distance in ACT on-ground is determined by the IFOV, which is the angle at satellite level subtended by a detector element.
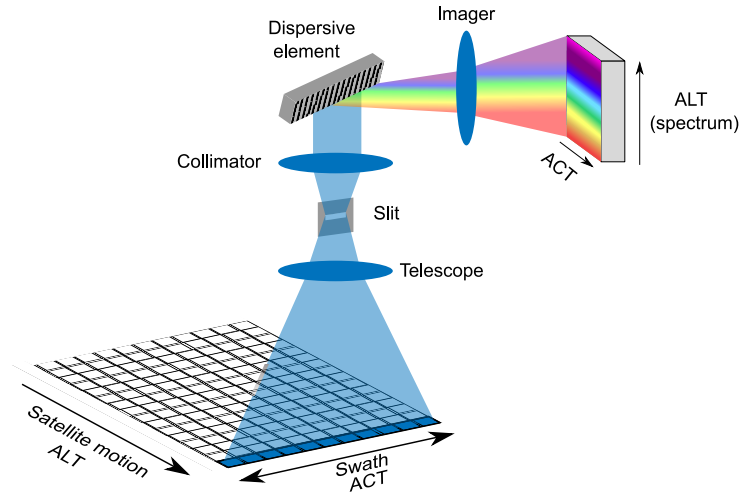
Figure 2.1: Observation principle of a push-broom imaging spectrometer. A ground scene is imaged through a telescope onto the entrance slit of the spectrometer. In the downstream spectrometer, the light is spectrally dispersed and finally imaged on a 2D array detector. One dimension of the detector represents the spectral information of the light, while the other represents the spatial information of the ground scene in ACT.

Design considerations

Several aspects must be considered in the development of an optical spaceborne push-broom spectrometer, depending in particular on the specific mission objectives. Typically, the requirements of the end user, the scientific user community, are translated into system requirements for the optical instrument. Some design parameters that are important in the context of this work and their design features are described below:

- **Telescope optics:** The telescope has the purpose to collect the radiation of the Earth from the desired viewing angle of the instrument. It images the Earth scene on-ground onto the entrance slit of the spectrometer. One of the most important parameters of the telescope is the F-number ($F\#$). It is a

measure of the capability of a lens to collect light for an optical image. The F-number, or often called F-ratio, is given by:

$$F\# = \frac{f}{D} \tag{2.1}$$

where f is the focal length of the telescope and D is the aperture diameter. Lower F-numbers are also referred to as "fast" because a sufficient signal can be achieved with shorter exposure times. The F-number is also a measure of the maximum angles of the rays incident on the image plane.

- **Slit:** The field-of-view (FoV) of a push-broom spectrometer is constrained by the slit size. In combination with the focal length of the telescope, the respective ground scene is imaged onto the slit plane. The slit image, after being spectrally dispersed in the spectrometer, is re-imaged on the detector. The dimension of the slit, the spectrometer magnification and the dispersion relation of the grating determine the spectral resolution. The narrower the slit, the higher the resolution.

- **Spectrometer:** The spectrometer consists of a collimator after the slit, a dispersive element and the imager camera. The ratio between the collimator and camera focal length and the grating resolution determines the magnification of the slit dimension on the FPA.

- **Focal plane array (FPA):** The focal plane array is an image sensor located in the focal plane of the camera. The detectors of the FPA for high quality spaceborne instruments are non-standard equipment. In general, its development starts together with the instrument. The associated spectral sampling interval (SSI), which defines the spectral difference between two adjacent spectral channels, is defined by the pixel size on the FPA, the focal length of the camera and the dispersion of the diffraction grating. The ratio of the number of pixels and the slit size in spectral direction determines the spectral oversampling.

2.2   Instrument Spectral Response Function (ISRF)

Assuming a monochromatic homogenous slit illumination and no imaging blur by the spectrometer optics, the slit would be imaged as a sharp area on the FPA. In fact, in realistic spectrometers, a narrow spectral line or absorption band is broadened by diffraction effects of the spectrometer optics and sampled by multiple pixels on the detector in spectral direction (ALT). This response function of the system is called the Instrument Spectral Response Function (ISRF). It is the radiometric response of a single spectral channel as a function of the wavelength of light incident on the instrument. It follows that a captured monochromatic spectrum is modified by the imaging properties of the spectrometer. The resulting recorded spectrum of the optical system is the monochromatic spectrum convolved with the ISRF of the instrument. As the ISRF fully describes the spectral response of the instrument, and establishes a direct link between the forward radiative transfer model of the retrieval algorithm and the spectra measured by the instrument, it is a key quantity of the spectral performance in terms of precision and accuracy. It also determines several critical mission parameters as for example the spectral resolution of the instrument $\Delta\lambda$, defined as the Full Width at Half Maximum (FWHM) of the ISRF or the association of the spectral channel, which is the barycentre of the ISRF.

2.2.1   ISRF definitions

Although it is a key variable, there is debate about the exact definition of the ISRF. As discussed by Caron et al. (2017), there are two different existing definitions. One has been particularly used for evaluating ISRF requirements during early industrial feasibility studies (Phase A/B1) of Earth observation (EO) instruments. The other definition was established by the European Space Agency (ESA) and is specified in the System Requirement Documents (SRD) of several recent EO missions. The first definition describes the ISRF as the instrument response to a monochromatic

stimulus at a fixed wavelength. The ISRF then calculates as:

$$\text{ISRF}(x) = \text{Slit}(x) \otimes \text{PSF}(x) \otimes \text{Pixel}(x) \tag{2.2}$$

where $\otimes$ is the convolution symbol, x the spectral dimension on the FPA, *Slit* the slit illumination scaled to the FPA, PSF is the optical point spread function (PSF) of the spectrograph and *Pixel* is the detector response characteristics. A schematic representation of the ISRF convolution kernels is given in fig. 2.2. The conversion of ISRF units from spatial ALT position on the FPA to wavelength is done by applying a scaling factor that depends on the dispersion relation of the diffractive element. The incident Earth radiance spectrum as measured by the instrument (i.e. accounting for blurring by the ISRF) is then given as:

$$L'(\lambda_i) = \int_0^\infty ISRF_1 (\lambda_i - \lambda, \lambda) \ L(\lambda) \ d\lambda \tag{2.3}$$

where $L'(\lambda_i)$ is the spectrally integrated radiance in spectral channel i as measured by the instrument and $ISRF_1$ the associated response of the instrument to a monochromatic λ. The practical advantage of this very intuitive definition is that
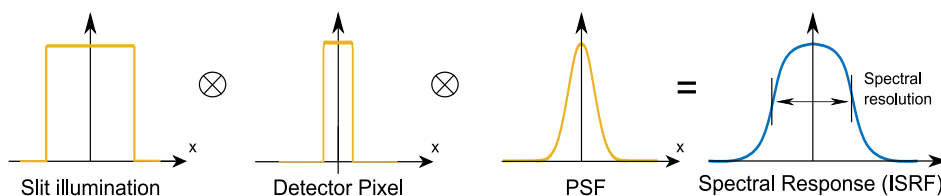
Figure 2.2: The typical definition of the ISRF of an imaging spectrometer is given by the convolution of the slit illumination, the pixel response and the optical PSF of the spectrograph optics.

it can be measured experimentally with a single monochromatic illumination. It is also used by scientists to translate the Earth's spectral radiance into the spectra measured by the instrument. The drawback of this definition is that the ISRF is a continuous function, but the sampling is limited by the detector pixels. Therefore, the ISRF cannot be assigned to a single spectral channel either, since it is effectively

covered by several pixels. Further, there will exist an infinite amount of ISRFs over the spectral range of the instrument, as each incident delta wavelength impulse $\delta(\lambda - \lambda_0)$ is associated to a specific ISRF. In principle, this would mean that there are an infinite number of ISRFs, making a complete and comprehensive characterization of the ISRFs impossible.

The second definition interprets the ISRF as the spectral origin of the photons detected in a given elementary spectral sample. In this definition, the spectrally integrated radiance as observed by the instrument is given as:

$$L'(\lambda_i) = \int_0^\infty ISRF_2(\lambda - \lambda_i, \lambda_i) \ L(\lambda) \ d\lambda \qquad (2.4)$$

where this time, the ISRF is associated to a spectral channel i instead of a monochromatic λ. In this definition, the ISRF belongs to a spectral channel and can be sampled as a continuous function using a tunable light with arbitrarily fine step size. Furthermore, there is only a finite number of ISRFs which is given by the number of elementary spectral samples. This definition is therefore used in ISRF instrument characterization campaigns.

Both interpretations of the ISRF are valid, but have different implications on some ISRF distortion and performance aspects, particularly in the presence of scene heterogeneity in ACT as discussed in section 2.3. Without scene heterogeneity in ACT direction, van Hees et al. (2018) found the two definitions of the ISRF to be mirror images of each other in certain scenarios. They also propose a fitting routine that shows satisfactory convergence from one ISRF definition to another. Throughout this thesis, the first definition of the ISRF is used and it is defined as the spectral response to a monochromatic stimulus. The reason for this is that the experiments and simulations conducted in this thesis are not limited by the lack of sampling of the ISRF. A monochromatic treatment of the problem provides more flexibility in measurement procedures and, in particular, allows measurements to be made in intermediate positions of the spectrometer, i.e. especially without using a dispersive element. Performance evaluation and critical parameter identification

are generally only slightly affected by the choice of definition.

2.2.2   ISRF characterization

In general, the ISRF is a wavelength- and FoV dependent instrument characteristic and hence may vary over the FPA position. It is experimentally determined prior to launch in on-ground calibration campaigns as part of the ISRF Calibration Key Data (CKD), which is then used for trace gas retrieval. In order to relate the measured spectra with the monochromatic TOA radiance, the ISRF needs to be known across the full spectral range and FoV. To obtain the ISRF, measurements are executed with a tunable laser source and the respective pixel response is recorded (Kleipool et al., 2018). The optical ground support equipment (OGSE) also has to provide an accurate and precise pointing of the illuminaton system in order to track the ISRF variation in spatial direction. The finite sampled ISRF is then parametrized with suitable complex functions, as for example a simple Gaussian (Munro et al., 2016), a super-Gaussian (Beirle et al., 2017) or a weighted sum of multiple functions (van Hees et al., 2018). Once in-orbit, the previously characterized ISRF needs to be validated and monitored. The deviation of the ISRF in-orbit with respect to the ISRF on-ground can have several reasons. The main source of ISRF deviations are thermal and mechanical ground-to-orbit displacements of the spectrometer optics. Thermal and mechanical displacements occur due to gravity release or moisture release and changes of temperature in combination with the respective coefficient of thermal expansion. Any shift in the position of the optical elements of the spectrometer results in a shift along the focal plane as well as transverse to it, which is directly reflected in a change in the shape and position of the ISRF. Previous missions as SCIAMACHY (Hamidouche and Lichtenberg, 2018) or OMI (Voors et al., 2006a) relied almost solely on the on-ground ISRF CKD. This required extremely mechanically stable and bulky optical bench constructions with corresponding effects on mass and cost. In addition to that, recent and upcoming EO mission like Tropomi (Veefkind et al., 2012) or Sentinel-5/UVNS

(Irizar et al., 2019) aim to monitor and validate the ISRF in-orbit by dedicated on-board calibration units. These include distributed feedback lasers that can be spectrally tuned by changing the operating temperature. The laser sources homogeneously illuminate the entrance slit of the spectrometer by means of a diffuser. Compared to the thorough on-ground calibration, this technique only allows to characterize very narrow wavelength bands constrained by the tunable range of the laser source. The primary goal of on-board coherent light sources is the monitoring of potential degradations and validation of the expected ISRF performance rather than to perform comparable measurements as done on-ground.

2.3   Heterogeneous Earth radiance scenes

The previously described ISRF on-ground characterization and the respective in-orbit monitoring and validation is limited by systematic effects in terms of instrument thermo-mechanical stability as well as limitations of the in-flight calibration. Yet, there are other sources that can affect ISRF stability and knowledge. The impact of Earth radiance heterogeneity on the ISRF was first recognized and identified by Voors et al. (2006a) in the context of the OMI mission. As part of scientific sensitivity studies, OMI determined that the accuracy of the wavelength scale is expected to vary smoothly in the order of 100th of a pixel over an orbit. In fact, a deviation of half a pixel was measured that could not be associated with either mechanical stability changes in the optical bench nor temperature shifts. Closer investigation could eventually relate the results to the Earth radiance contrast of the observed scenes. While the ISRF on-ground is characterized under the assumption of homogeneous slit illumination, this is not the case in realistic Earth scenes. Especially near clouds, snow, ice and coastlines, there are strong variations in the slit illumination, as the radiance is directly dependent on the albedo and ground topography. Since the slit illumination is a convolution kernel of the ISRF, the ISRF will differ depending on the respective illumination (see fig. 2.3). Most trace gas retrievals are only possible under cloud-free conditions, and thus
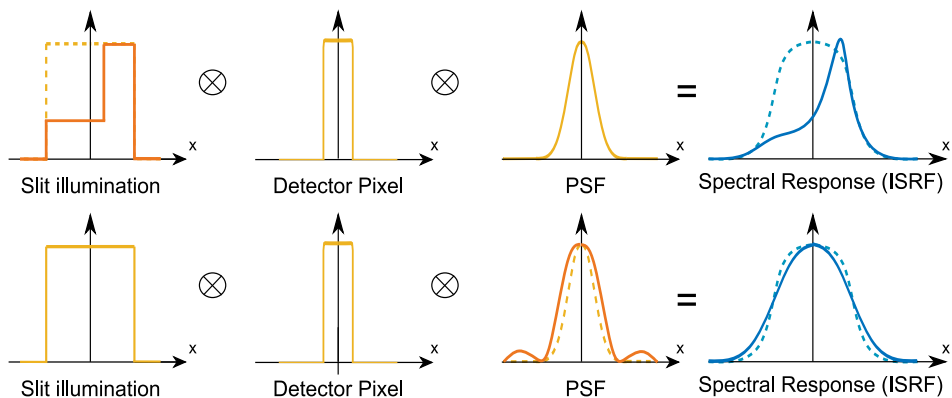
Figure 2.3: In the context of heterogeneous scenes, the ISRF can be altered by non-uniform slit illumination. In addition, the ISRF is also affected by instabilities in the optical PSF of the spectrometer.

cloudy scenes are usually discarded, which is why albedo variations are generally the largest contributor to heterogeneous scenes. Figure 2.4 shows an albedo map of the coal-fired power plant Jänschwalde, as captured by the Sentinel-2 instrument with a resolution of $20\,\mathrm{m}$ in the SWIR band ($2202\,\mathrm{nm}$). Imaging emission plumes from power plants is one of the primary goals of the upcoming CO2M mission (Kuhlmann et al., 2020; Sierk et al., 2021), which requires particularly high single-sounding precisions also over heterogeneous scenes (see section 5.1). The mission provides for a spatial resolution of $2\,\mathrm{km} \times 2\,\mathrm{km}$, whereby the spatial expansion of the contrast pattern can be found very noticeably in the slit illumination, and therefore create distortions in the ISRF. In a push-broom spectrometer, the scene contrast in ALT is not directly converted to slit illumination, because the ALT motion of the satellite during the integration times results in a temporal averaging of the scene contrast, which reduces the scene heterogeneity. The remaining variations in the slit illumination depend on the ratio of the IFOV and the sampling distance on-ground in ALT. The sampling distance is given as the distance travelled in ALT during the sensor integration time. Therefore, instantaneous albedo transitions are impossible to be observed on-ground and will be smoothed during the integration time. For this reason, spectrometers with a large scan area like GOME (Burrows et al., 1999) or SCIAMACHY (Burrows et al., 1995; Bovensmann et al., 1999) are

less vulnerable to contrasts in the Earth scene due to the small ratio between the slit footprint and the smear distance. In contrast, more recent spatially high-resolution spectrometer missions, such as Sentinel-5/UVNS or CO2M, are much more affected.
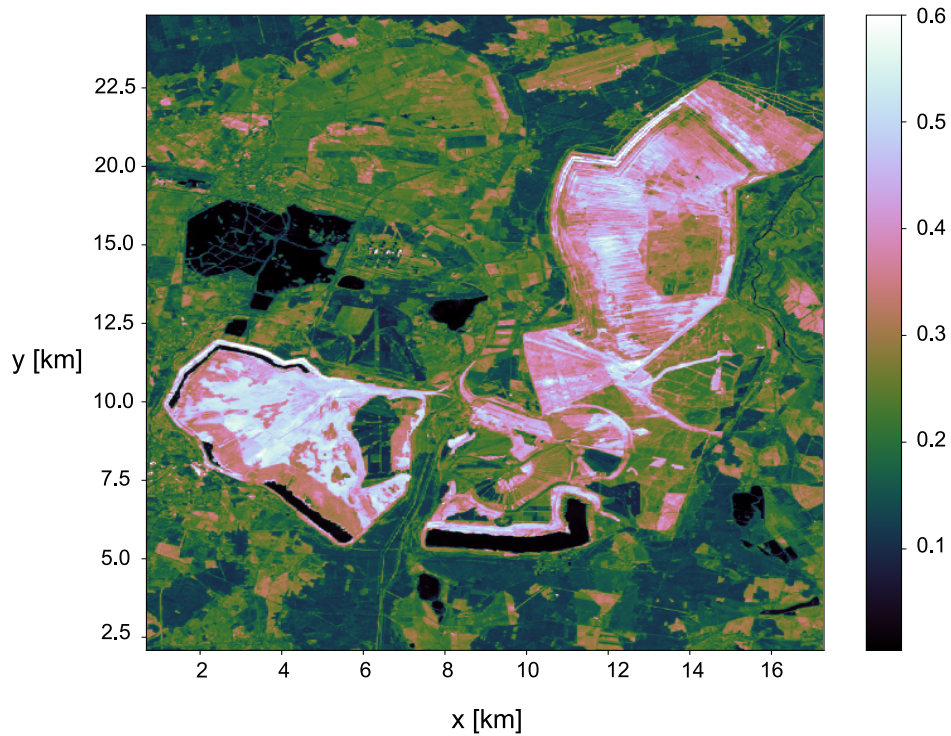
Figure 2.4: Real ground scene computed from Sentinel-2 data. Depicted is the albedo distribution over the coal-fired power plant Jänschwalde in the SWIR (2202 nm) at a resolution of 20 m. The CO_2 emitted in the power production is an example for a key observation target of the CO2M mission. Lakes and mining areas and the corresponding differences in SWIR reflectance intensity create high contrasts in the Earth radiance distribution.

Scene heterogeneity in ACT

So far, only heterogeneous scenes in ALT direction have been addressed as they are a major contributor to the ISRF due to their direct impact on the slit illumination. However, heterogeneous scenes in ACT direction can also affect the ISRF. In a perfect imaging system, the monochromatic image of the slit at any wavelength is straight and aligned with the detector array. Any deviation from this optimal

configuration is often referred to as spectrometer smile. In the presence of this effect, the ISRF is also distorted by heterogeneous scenes in ACT direction, since the slit image on the detector is no longer aligned with the spatial axis. During the superposition of all the sub-pixel ISRFs in ACT direction, partial illumination of a spatial sample in ACT direction causes the ISRF of the corresponding spectral channel to be narrower and shifted (see Caron et al. (2017); Gerilowski et al. (2011)). It is worth mentioning that in this case $ISRF_1$ and $ISRF_2$ as defined above are no longer mirror images of each other. Since this effect can only be triggered by spectrometer properties and misalignment and then becomes visible due to heterogeneous scene in ACT, it is usually fixed by stringent spectrometer smile requirements. This effect can have an impact on the spectral accuracy of EO instruments, but was not considered in the context of this work, as it is addressed, for example, in the case of Sentinel-5/UVNS through smile requirements.

2.4   Scene heterogeneity mitigation

In order to cope with the arising spectral errors due to heterogeneous scenes, several mitigation technologies for previous and future missions were analyzed. There are existing software correction algorithms as well as hardware solutions. In the following, the principle of both options will be presented and discussed.

2.4.1   Software correction

The OMI mission was, on the one hand, the first mission to recognize the impact of heterogeneous scenes and, at the same time, the first to investigate and propose a software correction algorithm. As proposed by Voors et al. (2006b), the correction approach makes use of available temporally oversampled data. By splitting the detector signal of a full exposure time into intermediate detector readings, the evolution of the radiance of a spatial sample on the detector can be reconstructed, giving an indication of the heterogeneity of the scene. In flight direction, two to five individual images are typically combined to form a final overall image. The

time evolution of the radiance can in turn be used to predict the expected change in wavelength shift due to scene heterogeneity. The predicted wavelength shift and the corresponding conversion factor between the measured wavelength and the actual wavelength are calculated as:

$$\Delta\lambda\left(x,y\right) = F\left(x,y\right) \cdot \Delta rad\left(x,y\right) \tag{2.5}$$

where $\Delta\lambda$ is the wavelength shift, F the conversion factor, Δrad the observed rate of change in the temporally oversampled spatial samples and x and y corresponds to the spatial (rows) and spectral (columns) dimension on the FPA. With this technique, the wavelength shift can be corrected to values below 0.01 pixels in the UV2 $(307 - 383\,\text{nm})$ and VIS $(349 - 504\,\text{nm})$ channel.

The disadvantage of these software corrections is that they only work in UV, UVVIS and NIR wavelength band. In the SWIR, highly variable atmospheric components such as H_2O and, in addition, the strong absorption lines generated by many different gases make software correction impossible (Caron et al., 2019). In response to this problem, hardware solutions called slit homogenizers (SH) have been studied for recent atmospheric composition measurement missions.

2.4.2 Hardware solution: Slit Homogenizer

A more robust solution to reduce errors due to heterogeneous scenes is given by slit homogenizers. A promising solution of a 1D-Slit Homogenizer (1DSH) is based on mirrors as developed for the Sentinel-5/UVNS mission. In this technique, the Earth scene radiance contrast is homogenized in the spectral direction (ALT) by means of reflection between two parallel mirrors. Besides Sentinel-5/UVNS, several other EO missions make use of this technology. The Absorbing Aerosol Sensor (AAS) will be launched aboard the GaoFen-5B satellite as part of China's EO program and is equipped with a mirror-based 1DSH. NASA's second Earth Venture Mission Geostationary Carbon Cycle Observatory (GeoCarb), observing radiances in the $O_2 - A$ $(0.76\,\mu\text{m})$, weak CO_2 $(1.61\,\mu\text{m})$, strong CO_2 $(2.06\,\mu\text{m})$ and the CO/CH_4

(2.32 μm) bands to provide GHG measurements over North and South America in a geostationary orbit make also use of this technology. Its step- and stare slit-scan strategy is particularly vulnerable to heterogeneous scenes because of the absence of platform motion smear (III et al., 2018). In simulations, their 1DSH design is predicted to reduce the retrieval error by a factor of 6.0 for CO_2, a factor of 4.8 for CO and by factor of 3.3 for CH_4 (Nivitanont et al., 2019; Somkuti et al., 2021). In the frame of this thesis, a detailed performance prediction model of the 1DSH present in the Sentinel-5/UVNS instrument was conducted, critical design parameters identified and limitations of the technology pointed out (see section 4). In addition to the mirror-based 1DSH, the technology of another SH concept, called 2D-Slit Homogenizer (2DSH), is investigated in the context of future remote sensing instruments. The 2DSH as proposed for the CO2M mission defines a new generation of slit homogenizer based on multimode fibres, which scramble the light in both ACT and ALT direction (2D). As a part of this thesis, a validation of an efficient concept of a fibre-based 2DSH is given in section 5.

3   Fourier Optics in imaging Spectrometers

This section presents the theoretical concepts for light propagation in imaging spectrometers based on Fourier optics. These concepts are applied at several points in this thesis when introducing the slit homogenizer into optical imaging systems and simulating the performance of EO missions. The presented terms and definitions can be found in Goodman (2005), Tyson (2014) or Saleh and Teich (2019), whereas the following summary of the used concepts is primarily adopted from the first source.

3.1   Scalar Diffraction Theory

The phenomenon of diffraction is of utmost importance in the field of optical imaging systems. Diffraction describes the phenomena that occur when a wave encounters an obstacle or opening. In the context of this work, we use the Rayleigh-Sommerfeld description of diffraction, which uses some simplifications. The most important one is that light is considered as a scalar phenomenon and therefore the vectorial nature of light is neglected. This assumption is valid if two conditions are met. First, the diffracting aperture must be large compared to the wavelength of the light. This is given in the common imaging spectrometers considered in this work. At the possible places where diffraction occurs, namely at the telescope aperture stop, in the slit plane as well as in the spectrometer aperture stop, the obstacles are always several orders of magnitude larger than the wavelength for instruments in the UV/NIR/SWIR wavelength regime (example Sentinel-5/UVNS slit: $65\,\text{mm}$ x $240\,\mu\text{m}$ (ACT/ALT) compared to $\lambda = 270-2385\,\text{nm}$). Second, the diffraction must not be observed too close to the limiting medium causing the diffraction. Both conditions are given in the following considerations of this work. In a first step, the following question is answered: given the electromagnetic field of the light in one plane, how do we find the field after propagation in another plane? To do so, let us consider the Maxwell's equations describing the interaction between an electric field vector $\vec{\mathcal{E}} = (\mathcal{E}_x, \mathcal{E}_y, \mathcal{E}_z)$ and a magnetic field

vector $\vec{\mathcal{H}} = (\mathcal{H}_x, \mathcal{H}_y, \mathcal{H}_z)$:

$$
\begin{aligned}
\nabla \times \vec{\mathcal{E}} &= -\mu \frac{\partial \vec{\mathcal{H}}}{\partial t} \\
\nabla \times \vec{\mathcal{H}} &= \epsilon \frac{\partial \vec{\mathcal{E}}}{\partial t} \\
\nabla \cdot \epsilon \vec{\mathcal{E}} &= 0 \\
\nabla \cdot \mu \vec{\mathcal{H}} &= 0
\end{aligned}
\tag{3.1}
$$

where ∇ is the Nabla operator, μ is the permeability and ϵ the permittivity of the propagation medium. Further it is assumed that there is no free charge. The electric field vectors as well as the magnetic field vectors are functions of position and time. Applying $\nabla \times$ on both sides of the first two equations and assuming that the medium is linear, isotropic, homogeneous and nondispersive (i.e. ϵ and μ are constant) yields:

$$
\begin{aligned}
\nabla^2 \vec{\mathcal{E}} - \frac{n^2}{c^2} \frac{\partial^2 \vec{\mathcal{E}}}{\partial t^2} &= 0 \\
\nabla^2 \vec{\mathcal{H}} - \frac{n^2}{c^2} \frac{\partial^2 \vec{\mathcal{H}}}{\partial t^2} &= 0
\end{aligned}
\tag{3.2}
$$

$n = \left(\frac{\epsilon}{\epsilon_0}\right)^{\frac{1}{2}}$ is the refractive index and $c = \frac{1}{\sqrt{\epsilon_0 \mu_0}}$ the velocity of propagation in vacuum, where μ_0 and ϵ_0 are the vacuum constants. Since the vector of the wave equation is satisfied by each component of $\mathcal{E}$ and $\mathcal{H}$, we can introduce an identical scalar wave equation as:

$$
\nabla^2 u\left(P, t\right) - \frac{n^2}{c^2} \frac{\partial^2 u\left(P, t\right)}{\partial t^2}
\tag{3.3}
$$

where $u\left(P, t\right)$ is the generalized form of any scalar field component and a function of position P and time t. At the expense of the limitations as described at the beginning of the chapter, the scalar wave description has given us a simpler form of the wave equation, which we can use to perform further calculations below.

3.1.1 Helmholtz Equation

For the next step, the scalar field for a monochromatic wave may be explicitly written as:

$$u\left(P,t\right) = A\left(P\right)cos\left[2\pi\nu t - \phi\left(P\right)\right]$$
$$= Re\left[U\left(P\right)exp\left(-i2\pi\nu t\right)\right] \tag{3.4}$$

where $A\left(P\right)$ denotes the wave amplitude, $\phi\left(P\right)$ the wavefront phase at point P, ν the optical frequency and $U\left(P\right)$ a complex function of position P given as:

$$U\left(P\right) = A\left(P\right)exp\left(i\phi\left(P\right)\right) \tag{3.5}$$

Substituting eq. (3.4) into the scalar wave equation (eq. (3.3)), it follows that $u\left(P,t\right)$ satisfies the time independent wave equation:

$$\left(\nabla^2 + k^2\right)U = 0 \tag{3.6}$$

with k being the wave number and given as $k = \frac{2\pi}{\lambda}$. Equation (3.6) is known as the *Helmholtz Equation*. Note that from that point, in principle the complex function U could always be solved for each individual case numerically as a boundary value problem. However, it is desirable to have an analytical expression for U in a homogeneous medium. This can be accomplished by applying *Green's theorem* to calculate U when its value is known at some boundary surface.

3.1.2 Green's theorem

Green's theorem is stated as an equation describing the equality between energy leaving a volume to the energy leaving a surface enclosing volume, where the direction is normal to that surface. Mathematically, it serves for a calculation of U at a given position in terms of the fields known at some boundary, without explicitly solving eq. (3.6). The relation is given as:

$$\int\int_V\int \left(U\nabla^2 G - G\nabla^2 U\right) dV = \int\int_S \left(U\frac{\partial G}{\partial n} - G\frac{\partial U}{\partial n}\right) dS \tag{3.7}$$

where S is a closed surface surrounding a volume V, $\frac{\partial}{\partial n}$ signifies a partial derivative in outward normal direction at each point in S and $G(P)$ is a complex function of position, whose first and second partial derivative are single-valued and continuous within and on the closed surface S. This theorem is considered to be the prime foundation of scalar diffraction theory. Note that only a prudent choice of the auxiliary function G and the closed surface S allows for direct application to the diffraction problem. In a next step, we want to express an optical disturbance at an observation point P_0 in terms of values on an arbitrary surface S surrounding P_0. Deriving from Huygen's theorem that each point of a wave front is the origin of a new elementary spherical wave, Sommerfeld found a very elegant choice for the Green's function. In mathematical formulation, a spherical wave expanding around the point P_0 at position P_1 is given by:

$$G(P_1) = \frac{exp(ikr_{01})}{r_{01}} \tag{3.8}$$

where r_{01} is the length of the vector $\vec{r}_{01}$ pointing from P_0 to P_1 and P_1 is an arbitrary point in the aperture plane σ. Suppose there is another source point $\tilde{P}_0$ at a mirror image on the opposite side of the initial observation point P_0 of the same wavelength and suppose that the two sources are oscillating with a 180° phase difference, the function $G(P_1)$ modifies to:

$$G_-(P_1) = \left[\frac{exp(ikr_{01})}{r_{01}}\right] - \left[\frac{exp(ik\tilde{r}_{01})}{\tilde{r}_{01}}\right] \tag{3.9}$$

where $\tilde{r}_{01}$ is the length of the vector from $\tilde{P}_0$ to P_1. Applying some calculus to eq. (3.7), for which we refer to Goodman (2005) for details, it is possible to retrieve the field at P_0 as a function of the field at P_1 as:

$$U(P_0) = \frac{1}{4\pi} \int_\Sigma \left(\frac{\partial U}{\partial n} G - U \frac{\partial G}{\partial n}\right) dS \tag{3.10}$$

where Σ is the plane aperture in the region of P_1. This equation is valid if scalar theory holds, both functions, G and U satisfy the homogeneous scalar wave equation

(eq. (3.3)) and the field U vanishes at least as fast as the diverging spherical wave. Inserting eq. (3.9) into eq. (3.10) and after applying mathematical calculus (see Goodman, 2005), we end up with the *Rayleigh-Sommerfeld Diffraction formula*:

$$U\left(P_0\right) = \frac{1}{i\lambda} \int\int_{\Sigma} U\left(P_1\right) \frac{exp\left(ikr_{01}\right)}{r_{01}} cos\left(\vec{n}, \vec{r_{01}}\right) ds \qquad (3.11)$$

The Rayleigh-Sommerfeld Diffraction formula allows us to describe the radiation
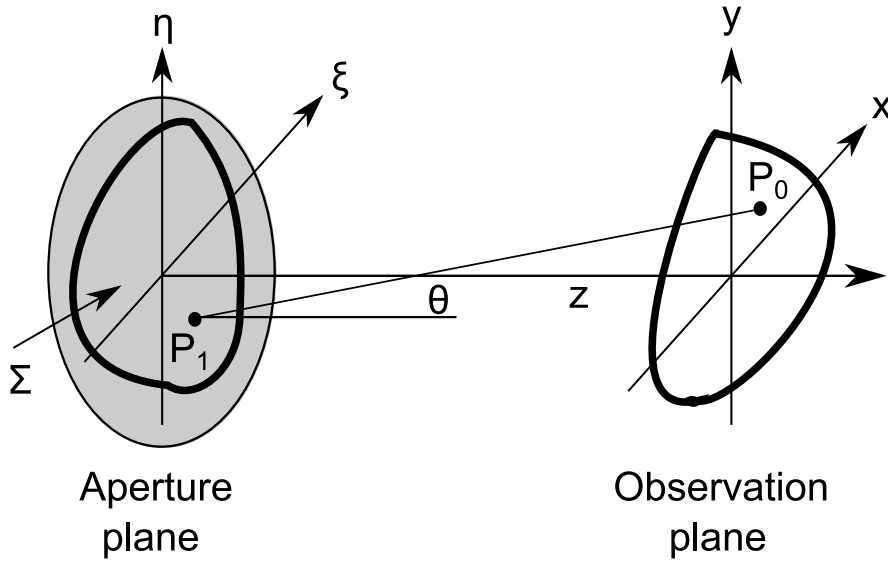
Figure 3.1: Diffraction geometry considered for the Huygens-Fresnel principle in rectangular coordinates. The diffracting aperture is lying in the (ξ, η) plane and is illuminated in positive z direction. The observation plane, i.e. the calculated wavefield is parallel to (ξ, η) and lies in the (x, y) plane. Adapted from Goodman (2005).

at a point P_0 as a superposition of diverging spherical waves across an aperture originating from point P_1. This principle is also called the *Huygens-Fresnel principle*. Let us now define θ as the angle between the outward normal $\vec{n}$ and the vector r_{01}. The term is given as:

$$cos\left(\theta\right) = \frac{z}{r_{01}} \qquad (3.12)$$

where z is the axes that pierces both the P_0 plane and the P_1 plane. Note that the point P_0 lies in the (x, y) plane and the point P_1 lies in the (ξ, η) plane, the two planes are parallel to each other and also share a common z-axes. We can then

rewrite eq. (3.11) in Cartesian coordinates (see also fig. 3.1) as:

$$U\left(x,y\right) = \frac{z}{i\lambda} \int \int_{\Sigma} U\left(\xi,\eta\right) \frac{exp\left(ikr_{01}\right)}{r_{01}^2} \, d\xi d\eta \qquad (3.13)$$

where $r_{01} = \sqrt{z^2 + \left(x-\xi\right)^2 - \left(y-\eta\right)^2}$.

In the following subsection, some approximations are applied to the Rayleigh-Sommerfeld integral to obtain the very useful and widely used *Fresnel diffraction integral*. With these tools, we can then analyze the imaging systems of a spectrometer and calculate how the electromagnetic field propagates through the instrument.

3.2   Fourier properties of a lens

Besides the propagation of electromagnetic fields in free-space, the concept of light propagation through a lens is a concept that is frequently used in this work. In this section, the mathematical treatment of such processes is introduced.

3.2.1   Fresnel diffraction integral

As a first step, the Huygens Fresnel principle expression of eq. (3.13) is reduced to a more simple and usable expression. In the current form, it is almost impossible finding a closed-form solution when using an arbitrary field $U\left(\xi,\eta\right)$ and an arbitrary aperture geometry. A frequently used approach to this problem is to apply *Fresnel Approximation*. This means that the distance r_{01} is approximated as:

$$r_{01} \approx z \left[1 + \frac{1}{2}\left(\frac{\left(x-\xi\right)}{z}\right)^2 + \frac{1}{2}\left(\frac{\left(y-\eta\right)}{z}\right)^2\right] \qquad (3.14)$$

In this step, the binomial expansion of the square root of r_{01} is reduced to the first two terms. While dropping all terms except for z seems definitely valid for the r_{01}^2 in the denominator, more care has to be taken with the r_{01} in the exponent.

The accuracy of the approximation keeping only the first order term is considered acceptable if the following condition is met (Goodman, 2005):

$$z^3 >> \frac{\pi}{4\lambda} \left[(x - \xi)^2 + (y - \eta)^2 \right]_{max}^2 \quad (3.15)$$

Whenever this relationship is fulfilled, the maximum phase change induced by dropping the terms higher than first order is much less than 1 radian. Note that in many cases this condition is even too strict, since it is not necessary that the higher order terms of the expansion are small, but that the integral value does not change. Most of the contribution of the integral is assigned to the points that are near normal to the aperture plane, which corresponds to $\xi \approx x$ and $\eta \approx y$ (see eq. (3.16)). As a result, the specific values of the higher-order terms of the expansion are not crucial.

Applying the Fresnel approximation in eq. (3.13) and incorporating the boundary condition of the aperture in $U(\xi, \eta, 0)$ we get:

$$U(x, y, z) = \frac{e^{ikz}}{i\lambda z} \int\limits_{-\infty}^{\infty} \int\limits_{-\infty}^{\infty} U(\xi, \eta, 0) \, exp\left(i \frac{k}{2z} \left[(x - \xi)^2 + (y - \eta)^2 \right] \right) \, d\xi d\eta \quad (3.16)$$

solving the binomial formulas in the exponent yields:

$$\begin{aligned} U(x, y, z) = & \frac{e^{ikz}}{i\lambda z} \, exp\left(i \frac{k}{2z} \left(x^2 + y^2 \right) \right) \\ & \cdot \int\limits_{-\infty}^{\infty} \int\limits_{-\infty}^{\infty} \left[U(\xi, \eta, 0) \, exp\left(i \frac{k}{2z} \left(\xi^2 + \eta^2 \right) \right) \right] \\ & \cdot exp\left(-i \frac{2\pi}{\lambda z} \left(x\xi + y\eta \right) \right) \, d\xi d\eta \end{aligned} \quad (3.17)$$

which can be recognized as the Fourier transform of the product of the complex field exiting the aperture and a quadratic phase term exponential. This equation is known as the *Fresnel diffraction integral*. This term will be the start for many calculations considered in imaging spectrometers.

3.2.2 Input placed against the lens

In the next step, we will cover a simple, yet very important case, where a converging lens with focal length f is illuminated with a collimated plane wave. In the first scenario the input is placed directly in front of the lens as depicted in fig. 3.2. Let us
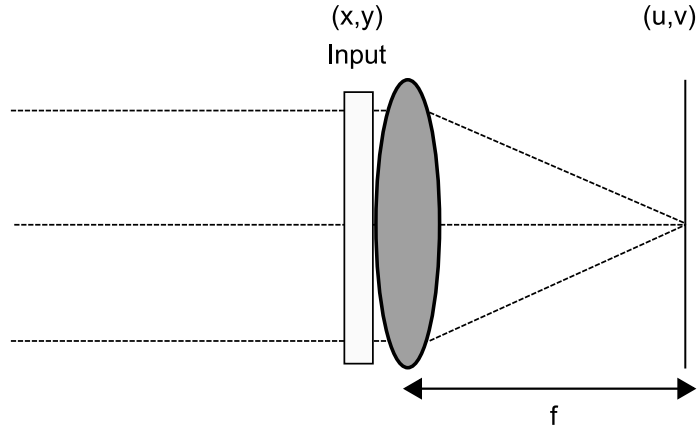
Figure 3.2: Geometries for light propagation through a lens. The input is placed directly in front of the lens. Adapted from Goodman (2005).

define the lens plane to be in the (x, y) plane and the focal point to be in the (u, v) plane. Let $U_l(x, y)$ be the field distribution right before the lens position. Including some paraxial approximations and accounting for the phase transformation of the lens (see Goodman, 2005), the field distribution right after the lens is given as:

$$U_l'(x, y) = P(x, y) U_l(x, y) \ exp\left[-i\frac{k}{2f}\left(x^2 + y^2\right)\right] \tag{3.18}$$

where the quadratic phase factor accounts for the phase transfer function of the thin lens. The lens maps an incident plane wave into a spherical wave, which converges toward the focal point f behind the lens. The restriction of the pupil size is determined by the pupil function $P(x, y)$. It is unity inside the pupil and zero outside of it:

$$P(x, y) = \begin{cases} 1 & \text{inside the pupil} \\ 0 & \text{otherwise} \end{cases} \tag{3.19}$$

To find the field distribution $U_f(u, v)$ in the focal plane of the lens, we insert eq. (3.18) into the Fresnel diffraction integral (eq. (3.17)) and evaluate it at the focal plane of the lens $(z = f)$. Dropping a constant phase factor we get:

$$
\begin{aligned}
U_f(u, v) = &\frac{exp\left[i\frac{k}{2f}(u^2 + v^2)\right]}{i\lambda z} \\
&\cdot \int\limits_{-\infty}^{\infty}\int\limits_{-\infty}^{\infty} U_l'(x, y)\, exp\left[i\frac{k}{2f}(x^2 + y^2)\right] exp\left[-i\frac{2\pi}{\lambda f}(xu + yv)\right]\, dxdy
\end{aligned}
\tag{3.20}
$$

Substituting eq. (3.18) into eq. (3.20) yields:

$$
\begin{aligned}
U_f(u, v) = &\frac{exp\left[i\frac{k}{2f}(u^2 + v^2)\right]}{i\lambda z} \\
&\cdot \int\limits_{-\infty}^{\infty}\int\limits_{-\infty}^{\infty} U_l(x, y)\, exp\left[-i\frac{2\pi}{\lambda f}(xu + yv)\right]\, dxdy
\end{aligned}
\tag{3.21}
$$

where we assumed that the physical extent of the input is smaller than the lens aperture, i.e. $P(x, y) \to 1$. This result is referred to as the *Fraunhofer diffraction pattern* of the field incident on the lens. We see that the quadratic exponential terms exactly cancel and the result has the form of the Fourier transform of the field at the lens multiplied by a quadratic phase factor. The Fourier Transform is generally defined by:

$$
\mathcal{F}\{U_l(x, y)\} = \int\limits_{-\infty}^{\infty}\int\limits_{-\infty}^{\infty} U_l(x, y)\, exp\left[-i2\pi(f_X x + f_Y y)\right]\, dxdy
\tag{3.22}
$$

Here, the spatial frequencies of the Fourier transform in eq. (3.21) are given as $f_X = \frac{u}{\lambda f}$ and $f_Y = \frac{v}{\lambda f}$. Writing the diffraction integrals in the form of a Fourier transform has the advantage that very efficient Fast Fourier transform algorithms can be used to solve the integral for discrete signals. By this technical simplification the computation time can be significantly reduced. Note that due to the quadratic phase factor the field is just proportional to the Fourier transform. However, in

some cases, one is interested in the intensity in the focal plane, in which case the results are exactly the same.

3.2.3 Input placed in front of the lens

Now we consider the more general case where the input at a distance d in front of the lens is illuminated with a normally incident plane wave as depicted in fig. 3.3.

Let $F_o[f_X, f_Y]$ be the Fourier spectrum of the light transmitted by the input
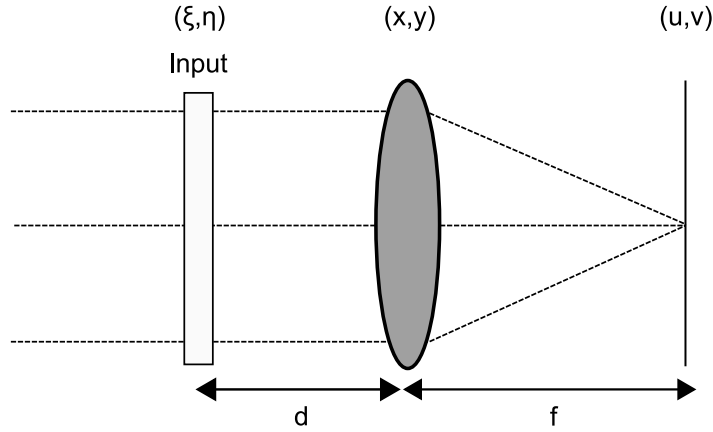
Figure 3.3: Geometries for light propagation through a lens. The input is placed at a distance d in front of the lens. Adapted from Goodman (2005).

transparency and $F_l[f_X, f_Y]$ the Fourier spectrum at the lens position given as:

$$F_o(f_X, f_Y) = \mathcal{F}\{U_o\} \quad \text{and} \quad F_l(f_X, f_Y) = \mathcal{F}\{U_l\}$$

where f_X and f_Y are as before the spatial frequencies of the Fourier transform, U_o the field transmitting through the object, U_l the field at the lens and $\mathcal{F}\{U_o\}$ and $\mathcal{F}\{U_l\}$ are the Fourier transform of the functions U_o and U_l respectively. Propagating the field from the object to the lens by relating the Fourier spectrum and applying Fresnel approximation we get:

$$F_l(f_X, f_Y) = F_0(f_X, f_Y) \, exp\left[-i\pi\lambda d\left(f_X^2 + f_Y^2\right)\right] \tag{3.23}$$

where a constant phase factor was dropped. Neglecting again the finite extent of the lens, i.e. assuming the input is smaller than the lens and therefore setting $P(x, y) \to 1$, eq. (3.21) can be written as:

$$U_f(u, v) = \frac{exp\left[i\frac{k}{2f}(u^2 + v^2)\right]}{i\lambda f} F_l\left(\frac{u}{\lambda f}, \frac{v}{\lambda f}\right) \tag{3.24}$$

Substituting eq. (3.23) into eq. (3.24), we have the result:

$$\begin{aligned} U_f(u, v) &= \frac{exp\left[i\frac{k}{2f}\left(1 - \frac{d}{f}\right)(u^2 + v^2)\right]}{i\lambda f} F_0\left(\frac{u}{\lambda f}, \frac{v}{\lambda f}\right) \\ &= \frac{exp\left[i\frac{k}{2f}\left(1 - \frac{d}{f}\right)(u^2 + v^2)\right]}{i\lambda f} \\ &\quad \cdot \int_{-\infty}^{\infty}\int_{-\infty}^{\infty} U_o(\xi, \eta) exp\left[-i\frac{2\pi}{\lambda f}(\xi u + \eta v)\right] d\xi d\eta \end{aligned} \tag{3.25}$$

In this configuration, the object is in the (ξ, η) plane, the lens in the (x, y) plane and the focal point in the (u, v) plane. There is again a quadratic phase factor that precedes the integral. It shall be emphasized that the phase factor vanishes in the special case when $d = f$. This is the case if the object is placed in the front focal plane of the lens. Thereby the phase curvature disappears and we end up again with an exact Fourier transform relation.

The two covered imaging cases enable us to express the electromagnetic wave propagation through an imaging spectrometer by means of scalar diffraction theory. So far, we have considered perfect optical systems, where the lens generates perfect spherical wave that converge toward the ideal geometrical image point. Due to the limited quality of the design and manufacturing of optical components, this will not be the case for realistic imaging systems. A more realistic and thus accurate treatment of the instruments is discussed in the following section by introducing optical aberrations into the systems.

3.3   Zernike Aberration Theory

In diffraction limited imaging systems, the PSF of the system will be the Fraunhofer diffraction pattern of the exit pupil as derived in eq. (3.21). In that case, the wavefront after the lens is of perfect spherical shape. In realistic optical systems this will not be the case. Instead, the wavefront after the lens deviates from the spherical shape due to imperfections of the optical components and result in a deviation of the ideal geometrical image point, and therefore cause the image formed by the lens to be distorted or blurred. This phenomena is called optical aberration. It is frequently analyzed by geometrical optics, where the light propagation is described in terms of rays and usually does not account for effects such as diffraction and interference.

3.3.1   Generealized pupil
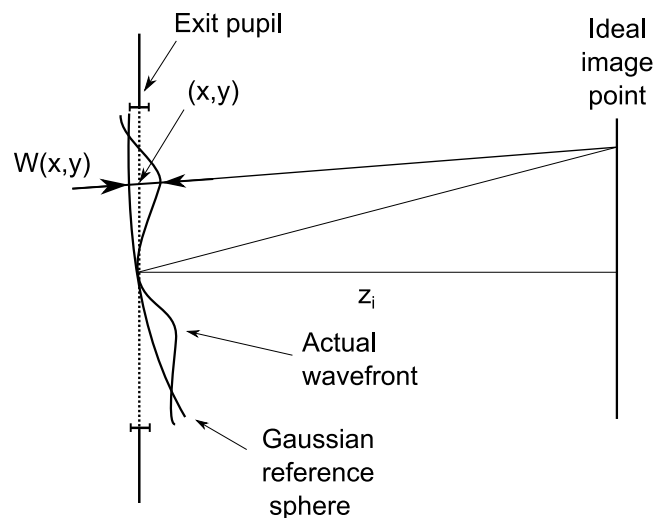
Figure 3.4: Definition of the aberration function $W(x,y)$. Optical aberrations are defined as deviations of the actual wavefront to a Gaussian reference wavefront measured at the exit pupil. For an ideal system, the reference wavefront is corresponding to a sphere. Adapted from Goodman (2005).

As diffraction and interference effects play a major role in the field of slit homogenizer, we incorporate optical aberration in our previously introduced diffraction integrals. The incorporation of wavefront error into such a system can be made

by adding a phase shifting plate onto the telescope aperture, therefore deforming the wavefront phase that leaves the pupil. A phase error at a point (x, y) on the telescope aperture is given by $kW(x, y)$, where $k = \frac{2\pi}{\lambda}$ and W is the effective path length difference with respect to a perfect *Gaussian reference sphere* without aberrations. Figure 3.4 shows the definition of the wave aberration geometry. In a system without any aberrations, the wavefront at the position of the exit pupil would be given by a perfect spherical wave which converges towards an ideal image point. The error, i.e. the sign of $W(x, y)$ can either be negative or positive depending on the direction of the deviation with respect to the reference sphere. By scaling $W(x, y)$ in units of wavelength, the complex amplitude transmittance $\mathcal{P}(x, y)$ of the phase-shifting plate is given by Goodman (2005):

$$\mathcal{P}(x, y) = P(x, y) \; exp\left[ikW(x, y)\right] \tag{3.26}$$

where $P(x, y)$ is as before the pupil function. The complex function $\mathcal{P}$ is called the *generalized* pupil function. The PSF of this generalized function is still given by the Fraunhofer diffraction pattern of the deviated wavefront. Hence, the calculation of the PSF is given by the Fourier Transform of the complex field at the exit pupil plane. The formulation of the wavefront error $W(x, y)$ can be defined in several ways. Here, we use Zernike circle polynomials to describe the wavefront error of the system.

3.3.2   Zernike aberration polynomials

Zernike polynomials are orthogonal and normalized set of basis to describe an arbitrary wavefront error on the unit disk. In particular, their orthonormality leads to a very convenient use of the Zernike expansion coefficients to combine different types of aberrations. When a wavefront is expanded in terms of Zernike coefficients the value of the coefficient is independent of the number of polynomials used in the expansion (Mahajan, 1998). Therefore, Zernike polynomials terms can be added or subtracted from each other without affecting the other coefficients.

A general wavefront error $W(\zeta, \eta)$ can be described as a sum of Zernike aberration terms. As Zernike polynomials are defined on the unit disk, we switch from Cartesian coordinates to polar coordinates. We follow the OSA/ANSI convention for the definitions of the Zernike polynomials and the indexing of the Zernike modes as described by Thibos et al. (2000). Similar to Noll's convention (Noll, 1976), which only differs by the indexing ordering of the Zernike modes but not by the definitions of the Zernike terms itself, they separate *even* and *odd* Zernike polynomials in terms of azimuthal angle φ defined as:

$$
\begin{aligned}
Z_n^m(r, \varphi) &= \sqrt{n+1}\, R_n^m(r)\, \sqrt{2}\, cos(m\varphi), & m &> 0 \\
Z_n^m(r, \varphi) &= \sqrt{n+1}\, R_n^m(r)\, \sqrt{2}\, sin(m\varphi), & m &< 0 \qquad (3.27) \\
Z_n^m(r, \varphi) &= \sqrt{n+1}\, R_n^0(r), & m &= 0
\end{aligned}
$$

where the radial polynomials $R_n^m(r)$ are defined as:

$$
R_n^m(r) = \sum_{k=0}^{(n-m)/2} \frac{(-1)^k (n-k)!}{k!\, [(n+m)/2 - k]!\, [(n-m)/2 - k]!}\, r^{n-2k} \qquad (3.28)
$$

where $m, n \in \mathbb{Z}$ and satisfy $|m| \leq n$, $n - |m| = even$. The polar coordinates are such that the radial distance $r = \sqrt{\zeta^2 + \eta^2}$ and the azimuthal angle $\varphi = tan(\eta/\zeta) \in [0, 2\pi]$. In order to not limit the description of an arbitrary wavefront to the unit disk, we normalize the radial coordinate r into $\rho = r/R$, where R is the radius of any circular aperture. The way the Zernike polynomials are defined in eq. (3.27) is reasonable as it gives a logical ordering to the modes and also allows the formulation of the following orthogonality relation:

$$
\int \rho\, d\rho\, d\varphi\ Z_j Z_j = \pi \delta_{i,j} \qquad (3.29)
$$

with $j = \frac{n(n+2)+m}{2}$ (Thibos et al., 2000) being a mode ordering number which is useful to define when describing single indexing scheme (i.e. combining m, n in a single index). The wavefront error for an arbitrary function $W(x, y)$ over a circle

of Radius R is given by the polynomial expansion:

$$W(R\rho, \varphi) = \sum_j c_j Z_j(\rho, \varphi) \tag{3.30}$$

where $c_j \in \mathbb{R}$ represents the magnitude of the respective Zernike polynomial. With this set of polynomials it is in principle possible to formulate any wavefront error induced by an optical system by including a sufficient set of Zernike modes. Every Zernike aberration term describes a certain property imposed by the system and by decomposing an arbitrary amount of terms creates a wavefront description up to the desired degree of accuracy. Table 3.1 contains the definitions and ordering scheme of the first 13 Zernike polynomials according to the OSA/ANSI index.

In the next step, we want to extend the Fraunhofer-diffraction integral to include the aberration effects of the imaging optical system. The effects of the imaging system (i.e. the induced wavefront errors) are impinged on the wavefront at the position of the lens. By applying the Fraunhofer-Diffraction integral from eq. (3.21) and accounting for the wave aberration function W, we get a field distribution in the focal plane as:

$$
\begin{aligned}
U_f(u, v) = & \frac{exp\left[i\frac{k}{2f}\left(u^2 + v^2\right)\right]}{i\lambda z} \\
& \cdot \int\limits_{-\infty}^{\infty}\int\limits_{-\infty}^{\infty} U_l(x, y)\, exp\left[-i\frac{2\pi}{\lambda f}(xu + yv)\right] exp\left[ikW(x, y)\right]\ dxdy
\end{aligned}
\tag{3.31}
$$

In the following, we will use the focal plane formulation of the PSF to determine the strength of various aberrations.

3.3.3   Characterization by the Point Spread Function

Characterization and measurement of wavefront errors of accurate optical systems is very difficult and requires very precise measurements. Although the physical wave nature of light has been known for decades, there are still no detectors that can simultaneously determine the intensity of the light as well as the phase. One way
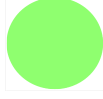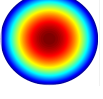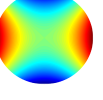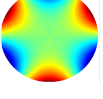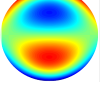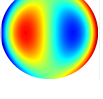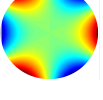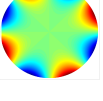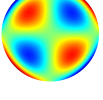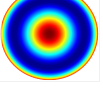
OSA/ANSI index (j)	Z_n^m	Z_j	Classical name	Plot
0	Z_0^0	1	Piston	
1	Z_1^{-1}	$2\rho\ sin(\varphi)$	Vertical tilt	
2	Z_1^1	$2\rho\ cos(\varphi)$	Horizontal tilt	
3	Z_2^{-2}	$\sqrt{6}\rho^2\ sin(2\varphi)$	Oblique astigmatism	
4	Z_2^0	$\sqrt{3}\,(2\rho^2 - 1)$	Defocus	
5	Z_2^2	$\sqrt{6}\rho^2\ cos(2\varphi)$	Vertical astigmatism	
6	Z_3^{-3}	$\sqrt{8}\rho^3\ sin(3\varphi)$	Vertical trefoil	
7	Z_3^{-1}	$\sqrt{8}\,(3\rho^3 - 2\rho)\ sin(\varphi)$	Vertical coma	
8	Z_3^1	$\sqrt{8}\,(3\rho^3 - 2\rho)\ cos(\varphi)$	Horizontal coma	
9	Z_3^3	$\sqrt{8}\rho^3\ cos(3\varphi)$	Oblique trefoil	
10	Z_4^{-4}	$\sqrt{10}\rho^4\ sin(4\varphi)$	Oblique quadrafoil	
11	Z_4^{-2}	$\sqrt{10}\,(4\rho^4 - 3\rho^2)\ sin(2\varphi)$	Oblique secondary astigmatism	
12	Z_4^0	$\sqrt{5}\,(6\rho^4 - 6\rho^2 + 1)$	Primary spherical	

Table 3.1: Definition and ordering according to the OSA/ANSI index of the first 13 Zernike polynomials.

to determine the phase is Interferometry. The optical system is illuminated with a reference light source, where a part of the light is propagated through the system and gets a phase change due to the aberrations of the optical system. Another part of the reference source that does not experience aberrations is then superimposed with the transmitted aberrated wavefront. The resulting interference pattern can then be used to analyze the type and strength of aberrations (Goodwin and Wyant, 2006). Another commonly used method is a Shack-Hartmann wavefront sensor. Here, a wavefront transmitted through the optical system is measured directly. The Shack-Hartmann sensor consists of a lens mask with regularly arranged microlenses and a 2D detector. When a collimated beam falls on the lens mask, each lens generates a point image in the focal plane. The respective position of the point images can then be measured and the exact wavefront in front of the Shack-Hartmann sensor can be reconstructed via software algorithms. The precise calibration of the optical components of the Shack-Hartmann sensor is crucial to this approach (Gross, 2005).

In optical instruments for space-based spectrometers, there are usually no requirements for the specific aberrations of the system, but only for the spot blur size on the detector, which corresponds to the size of the optical PSF. A typical criterion is the fraction of the energy contained in the PSF that lies within a certain radius around the PSF. To quantify the strength of the aberrations, we use as a reference in this work the radius of the PSF in which 80% of the energy is contained. In a system without aberrations and under a homogeneous illumination of a rectangular aperture, the size of the PSF is limited only by diffraction. Figure 3.5a shows a corresponding 2D contour plot as well as a radial profile of the diffraction limited PSF pattern in horizontal and vertical direction. The expected diffraction pattern in the image plane changes when aberrations are considered. Figure 3.5b shows an example of a system with an oblique astigmatism and an oblique quadrafoil impinged on the wavefront in the exit pupil plane. Comparing the two patterns, we find that the pattern with aberrations has a reduced height of the central peak which is caused by worsened conditions for constructive interference in the

(a) Diffraction limited PSF.

(b) PSF with aberrations.
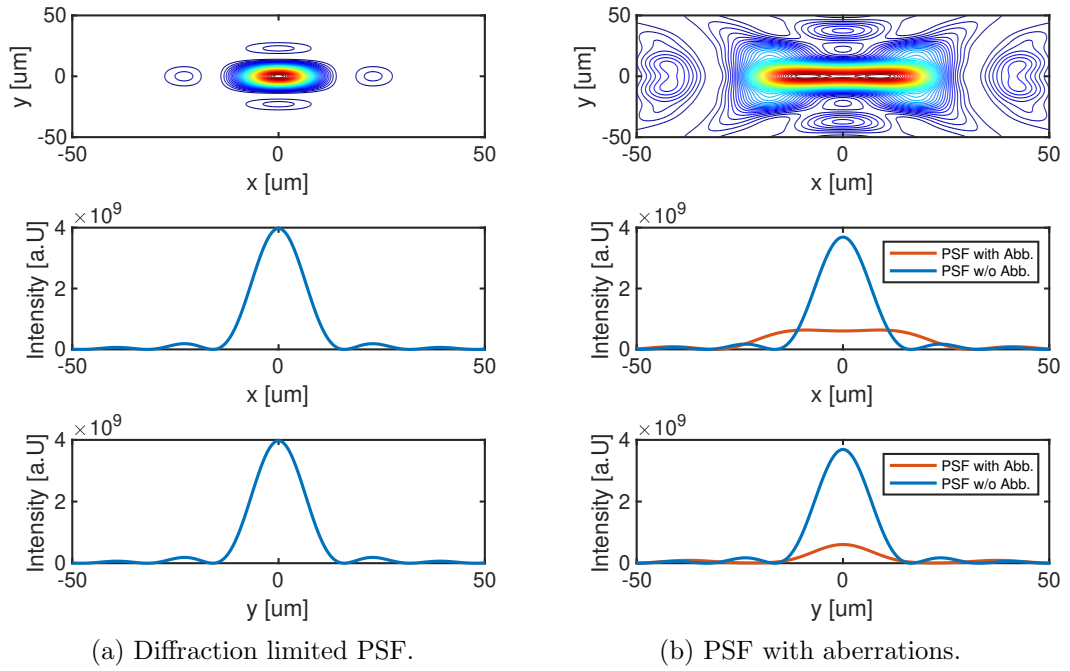
Figure 3.5: (a) PSF of an aberration-free idealized system. The intensity distribution of the field is given as the Fraunhofer-Diffraction pattern of a rectangular aperture. It is the minimum achievable spot size and is limited only by diffraction. (b) Exemplary PSF of a system with oblique astigmatism and oblique quadrafoil impinged on the wavefront in the exit pupil plane. The symmetries of the involved Zernike polynomials are clearly visible in the diffraction pattern. The maxima of the central intensity peak is reduced compared to the aberration free case and consequently the energy is distributed further away from the centre.

image plane and the energy is more widely distributed and consequently the radius of 80% encircled energy is larger. The symmetry of the diffraction pattern is substantially determined by the radial and angle dependent part of the involved Zernike polynomials.

In the next chapter, the theoretical concepts introduced in this chapter are used to describe the underlying physical effects of slit homogenizers in imaging spectrometers.

4   Mirror-based 1D-Slit Homogenizer (1DSH)

In this chapter, a mirror based 1D-Slit homogenizer (1DSH) concept consisting of two parallel mirrors is presented. This technique will be implemented in the Sentinel-5/UVNS instrument for the first time. In section 4.1 a short overview of the Sentinel-5/UVNS instrument is given and the primary mission goals are described. The principle of the 1DSH techniques and the actual implementation of the hardware is presented in section 4.2. In section 4.3, a first-order perform- ance model is presented which describes the light propagation through the SH by means of Huygens-Fresnel-diffraction integrals. Further, the ISRF stability over heterogeneous scenes is quantified and compared to a classical entrance slit. Section 4.4 discusses an important feature when implementing a 1DSH, which is the modification of the spectrometer pupil intensity distribution. Finally, a conclusion of the 1DSH technology is given in section 4.5.

> Substantial parts of the text in this section as well as many figures are adopted from the Atmospheric Measurement Techniques article published by the author of this thesis (Hummel et al., 2021b).

4.1   Sentinel-5/UVNS instrument

The Sentinel-5/UVNS mission aboard the MetOp Second Generation A-Series (MetOP-SG-A) satellite is part of the European Earth Observation Programme Copernicus fleet, which is coordinated and managed by the European commission. The main objective of Sentinel-5/UVNS is to launch an operational mission from low-Earth orbit that can provide daily atmospheric composition data for air quality monitoring and prediction, as well as for other chemical and climate applications. The instrument is nadir looking and operating in a push-broom configuration (de- scribed in section 2.1). The key data products of atmospheric constituent measured by Sentinel-5/UVNS will be ozone (O_3), nitrogen dioxide (NO_2), sulphur dioxide

(SO$_2$), formaldehyde (HCHO), glyoxal (CHOCHO), carbon monoxide (CO) and methane (CH$_4$) as well as aerosols and cloud properties. The instrument consists of five spectrometers covering a range from the ultraviolet to the shortwave infrared with seven different spectral bands in between: UV-1 $(270 - 300\,\text{nm})$, UV-2 $(300 - 370\,\text{nm})$, VIS $(370 - 500\,\text{nm})$, NIR-1 $(685 - 710\,\text{nm})$, NIR-2 $(745 - 773\,\text{nm})$, SWIR-1 $(1590 - 1675\,\text{nm})$ and SWIR-3 $(2305 - 2385\,\text{nm})$. The spectral bands are measured by five individual spectrometers (UV-1, UV2VIS, NIR, SWIR1 and SWIR3), each with its own detector optimized for the respective wavelength. The spectrometers are fed by two separate telescope optics. One telescope feeds the UV-2/VIS and NIR spectrometers and one telescope the UV-1, SWIR1 and SWIR-3 spectrometers. The detailed characteristics of the Sentinel-5/UVNS instrument is summarized in table 4.1. The design concept and the observation principle is based on the heritage of the Sentinel-5 Precursor mission with the primary TROPOMI instrument launched in 2017. The two instruments have similar measurement characteristics, spectral coverage as well as spectral resolution. A major point of difference between the two instruments is that TROPOMI is equipped with a classical slit and Sentinel-5/UVNS uses a new complex slit assembly called slit homogenizer to mitigate the impact on ISRF due to heterogeneous scenes.

4.2 Slit homogenizer principle

Sentinel-5/UVNS (Irizar et al., 2019) is the first push-broom spectrometer that employs an onboard concept to mitigate the spectral effect of non-uniform scenes in the along-track direction. A hardware solution called 1DSH is implemented, which reduces the scene contrast of the Earth radiance in ALT of the satellite flight motion by replacing the classical slit with a pair of two parallel extended mirrors (fig. 4.1). The two parallel rectangular mirrors composing the entrance slit have a distance in ALT of $b = 248\,\mu\text{m}$ (SWIR-1, SWIR-3), $240\,\mu\text{m}$ (UV2VIS, NIR), $480\,\mu\text{m}$ (UV1), side lengths of $65\,\text{mm}$ in ACT and a length of $9.91\,\text{mm}$ (SWIR-1, SWIR-3),

Mission orbit	MetOp-SG-A, sun synchronous ca. 825 km altitude
Spectral Range	- Ultraviolet 1 $270 - 300$ nm - Ultraviolet 2 $300 - 500$ nm - Near Infrared $685 - 710$ nm and $745 - 773$ nm - Short Wave Infrared 1 $1590 - 1675$ nm - Short Wave Infrared 3 $2305 - 2385$ nm
Key data products	O_3, NO_2, SO_2, HCHO, CO, CH_4 CHOCHO and aerosols
Spectral resolution	1 nm to 0.25 nm depending on the spectral band
Swath width	2670 km
Spectral resolution	0.25 nm (SWIR) - 1 nm (UV1)
Spatial resolution	7.5 km x 7.5 km
Data volume	80 Gbit per orbit
Electrical power	< 290 W
Service life	> 7 years
Weight	292 kg
Size	$1.0 \times 1.6 \times -1.2$ m

Table 4.1: Sentinel-5/UVNS mission characteristics and details.

9.6 mm (UV1, UV2VIS, NIR) along the optical axis. Thereby, the light focussed by the telescope optics onto the slit entrance plane is scrambled by multiple reflections in the ALT direction, whereas in ACT the light passes the 1DSH without any reflection. To preserve the full image information along the swath, the entrance plane of the 1DSH must be imaged; to homogenize the scene in ALT the exit plane of the 1DSH must be imaged. This is achieved by an astigmatism in the collimator optics. Heterogeneous scenes in ACT direction may also affect the ISRF stability in the presence of spectrometer smile (see section 2.3), which however will not be covered in this thesis. For a realistic reference Earth scene of the Sentinel-5/UVNS
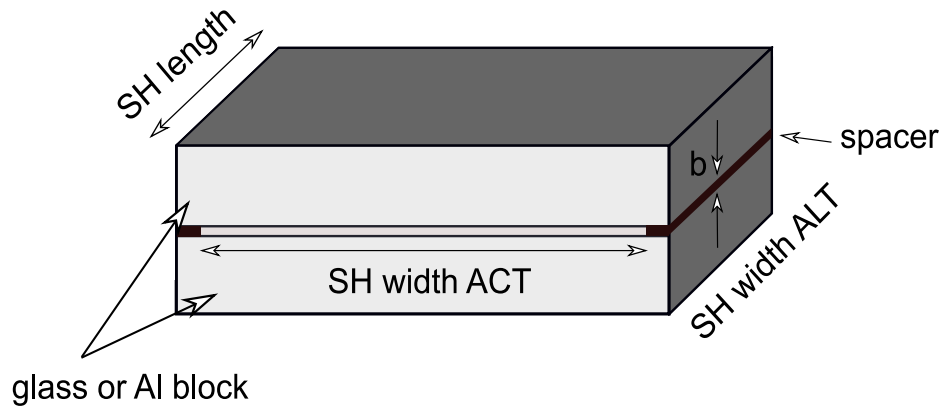
Figure 4.1: Mirror based SH geometry. The SH consists of two parallel mirrors that are separated by spacers. The width of the spacers correspond to the spectral size of the slit in ALT. The length of the SH along the optical axes creates multiple reflections on the mirrors.

mission provided by ESA (fig. 4.4), the ISRF shall meet the requirements of $< 2\,\%$ ISRF shape knowledge error, $< 1\,\%$ relative FWHM knowledge error as well as stringent centroid requirements varying for the spectral bands (table 4.5). Meister et al. (2017) and Caron et al. (2019) presented simulation results providing a first-order prediction of the performance of the SH principle, which are relevant to achieve the performance requirements above. However, so far several second order effects haven't been quantitatively addressed in the prediction of the homogenizing performance. In the frame of this thesis, the existing first-order models are extended and a more elaborate and comprehensive description of the 1DSH and its impact

on performance and instrument layout is provided. A new feature that is accounted for in this work is the phenomena of induced variation of the spectrograph pupil intensity distribution due to the homogenization of the SH exit plane. The multiple reflections at the mirrors of the SH alters the angular distribution of the light in the spectrograph pupil plane. The following sections will introduced a mathematical performance model based on scalar diffraction theory, which is able to assess the homogenization efficiency at the SH exit plane, the modification of the spectrograph pupil intensity distribution and the respective resulting impact on the ISRF. As the ISRF is not only a function of the slit illumination but also of the spectrograph PSF, a variation in the intensity distribution across the spectrograph pupil will ultimately put an uncertainty and error contribution to the ISRF. Throughout this thesis, the terms *near-field* and *far-field* are commonly used and will be introduced here:

- **Near-field (NF)** describes the intensity distribution in the SH exit plane. The NF of the SH is imaged on the detector after passing through the spectrograph optics. It forms a convolution kernel of the ISRF and is usually the largest contributor to scene dependent ISRF variations due to the size of the slit image on the detector.

- **Far-field (FF)** represents the intensity distribution in the spectrograph pupil plane. If the FF of the spectrograph is scene-dependent, the weighting of the aberrations present in the spectrograph optics will vary depending on the scene and consequently results in a scene dependency of the optical PSF of the system. Since the PSF is another convolution kernel of the ISRF, it has a direct impact on the stability of the ISRF.

It should be noted that the NF and FF are not independent of each other. On the contrary, as was shown in section 3.1, both fields are directly related by a Fourier transformation. It should be mentioned that especially in experimental measurements only intensities are determined, which means that the complex phase necessary for the re-construction is lost. However, in the case of the mirror-based

1DSH, the analysis is only based on a theoretical mathematical description. For this reason, in the considerations of this thesis, the complex phase of the electric field is completely given at each position of the instrument.

4.3   1DSH Near-Field

This section describes the underlying model and the theoretical homogenization capabilities of the 1DSH in the NF. Major parts of this section are based on the model developed by Meister et al. (2017). The analysis presented here goes beyond the results shown in previous studies and discusses additional further effects.

4.3.1   Length rule

In a first step, the working principle of the 1DSH is explained with the help of an intuitive geometrical consideration. The telescope optics in front of the 1DSH focuses a point on the Earth onto the SH entrance plane. Depending on the $F\#$ of the telescope optics, the point is mapped with a maximum opening cone angle ϕ onto the 1DSH entrance plane. With the help of an appropriate choice of the 1DSH length, this entry point is homogeneously distributed over the entire exit slit (fig. 4.2). Note that this principle is given for any entry position of the source point. Therefore, by purely geometrical reasoning, the 1DSH is perfectly designed if the following condition is fulfilled:

$$\frac{tan\left(\phi\right)}{b} = \frac{l}{2F\#b} \stackrel{!}{=} n \in \mathbb{N} \tag{4.1}$$

where b is the 1DSH width in ALT, l is the 1DSH length along the optical axis, n is the number of reflections, $F\#$ is the telescope F-number, and ϕ is the opening cone corresponding to the $F\#$ and given as:

$$tan\left(\phi\right) = \frac{1}{2F\#} \tag{4.2}$$
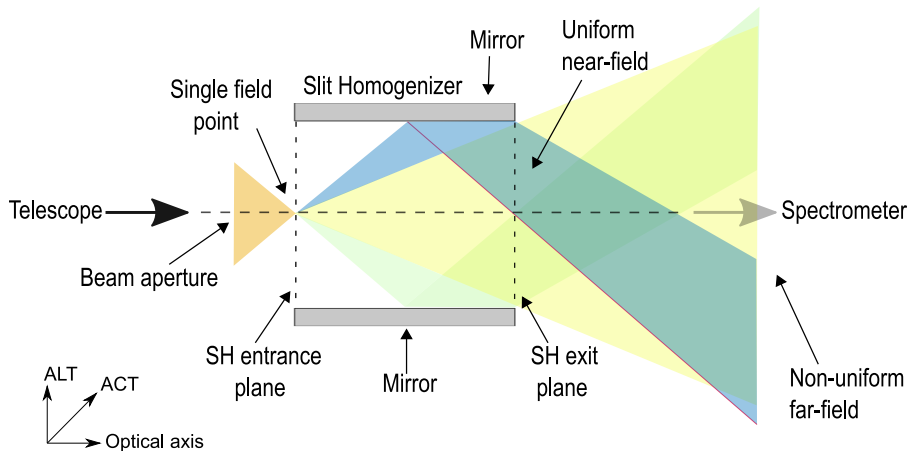
Figure 4.2: The SH homogenization principle based on a purely geometrical concept. With an appropriate length selection, the SH would perfectly homogenize any input scene in the SH exit plane. Furthermore, also due to geometric reasoning, one can deduce that the SH near-field homogenization comes at the cost of changed intensity distribution in the spectrograph pupil. Adapted from Hummel et al. (2021b).

However, this simple picture does not correspond to reality. As we will see in the further course, the reflections in the 1DSH create strong interference effects and a much more complex intensity pattern is created at the 1DSH exit plane. Nevertheless, despite the fluctuation due to interference effects, the length rule based on geometrical considerations already serves as a robust basis of general 1DSH design considerations. In the following, the geometric considerations will be replaced by treating the problem more accurately by means of scalar diffraction theory.

4.3.2   Diffraction model

The light from objects on the Earth that are imaged at one spatial position (ALT) within the 1DSH entrance, arrive at the Sentinel-5/UVNS telescope entrance pupil as plane waves, where the incidence angle θ is between $\pm 0.1°$. The extent of the wavefront is limited by the size and shape of the telescope aperture. Neglecting geometrical optical aberrations, the telescope would create a diffraction limited PSF

in the telescope image, where the 1DSH entrance plane is positioned. Depending on the angle of incidence, the PSF centroid will be located at a dedicated position within the 1DSH entrance plane. The electric field of the diffraction pattern in the 1DSH entrance plane is given as the Fourier transform of the complex electric field over the telescope pupil. For a square entrance pupil, the diffraction pattern is calculated as (see section 3.2.2):

$$
\begin{aligned}
\tilde{U}_{f,\theta}\left(u_a, v_a\right) &= \frac{A}{i\lambda f} e^{i\frac{k}{2f}\left(u_a^2+v_a^2\right)} \int_{\Omega} e^{iky_t\ sin(\theta)} e^{-i\frac{k}{f}(x_t u_a + y_t v_a)}\ dx_t dy_t \\
&= \frac{iAD^2}{\lambda f} e^{i\frac{k}{2f}\left(u_a^2+v_a^2\right)} sinc\left(\frac{Dk}{2f} u_a\right)\ sinc\left(\frac{Dk}{2f}\left(f sin(\theta) - v_a\right)\right)
\end{aligned}
\tag{4.3}
$$

where (x_t, y_t) are the coordinate positions in the telescope entrance pupil and (u_a, v_a) are the respective coordinates in the 1DSH entrance plane. Ω denotes the two-dimensional entrance pupil area, f is the focal length of the telescope, A the amplitude of the plane wavefront at the telescope entrance pupil, D the full side length of the quadratic telescope entrance pupil and $k = \frac{2\pi}{\lambda}$ the wavenumber. Further, the relation $\int_{-a}^{a} e^{ixc} dx = 2a sinc(ca)$ and a Fresnel approximation was applied in eq. (4.3). The propagation of $\tilde{U}_f$ through the subsequent 1DSH is described by the Huygens-Fresnel principle (eq. (3.13)). The reflections at the two mirrors are accounted for by inverting the propagation component in ALT upon every reflection n as:

$$
U_{f,\theta}(u_a, v_a) = R^{|n|} e^{in\pi} \tilde{U}_{f,\theta}\left(u_a, (-1)^n (v_a - nb)\right), \qquad \text{for } v_a \in \left[-\frac{b}{2} + nb, \frac{b}{2} + nb\right]
\tag{4.4}
$$

where R is the reflectivity, b is the slit width and $e^{in\pi}$ describes a phase jump upon every reflection n. Inserting eq. (4.3) into eq. (4.4) and applying the Huygens-Fresnel diffraction principle yields the expression for the intensity distribution at the SH exit plane for a given incidence angle θ, SH length l and distance

$r(u_a, v_a) = \sqrt{l^2 + (u_b - u_a)^2 + (v_b - v_a)^2}$ as:

$$
U_\theta(u_b, v_b) = \frac{lAD^2}{\lambda^2 f} \int\limits_{u_a \in \mathbb{R}} \int\limits_{v_a = -\frac{b}{2}}^{v_a = \frac{b}{2}} \sum_{n \in \mathbb{N}} R^{|n|} \frac{e^{i\frac{k}{2f}\left(u_a^2 + ((-1)^n(v_a - nb))^2\right) + ikr(u_a, v_a + nb) + in\pi}}{r^2(u_a, v_a + nb)}
$$
$$
\cdot \, sinc\left(\frac{Dk}{2f} u_a\right) sinc\left(\frac{Dk}{2f}\left(f sin(\theta) - (-1)^n \, v_a\right)\right) du_a dv_a
$$

$$(4.5)$$

where u_b, v_b are the coordinates of the position at the 1DSH exit plane. With the help of eq. (4.5), it is possible to map the field distribution of a diffraction-limited point source at the 1DSH entrance onto the 1DSH exit plane.

4.3.3   SH Transfer function

Evaluating eq. (4.5) for every incidence angle of the Sentinel-5/UVNS FoV results in the so called 1DSH transfer function (TRF), which maps any field point originating from Earth to an intensity distribution at the 1DSH exit plane. In a purely geometric theory and a perfect 1DSH configuration in terms of length, every point source would be distributed homogeneously in ALT direction (fig. 4.2). However, as is quantified in eq. (4.5), the field distribution at the 1DSH output plane highly depends on interference effects due to path differences of the reflected light inside the SH, resulting in a non-uniform transfer function as shown in section 4.4.3. For comparison and illustration, fig. 4.3d shows the TRF of a classical slit. In a classical slit, the slit entrance and the slit exit are the same plane. Therefore, the diffraction limited PSF at the slit entrance is not changed and leaves the slit in particular without homogenization. The TRFs for the case with 1DSH show the respective homogenization of a single incidence angle over the 1DSH exit plane. Since the interference effects of coherent light are the main source of the fluctuations, there is a strong wavelength dependence of the intensity distribution in the transfer function. Higher wavelengths show faster repetitions and larger peak-to-valley amplitudes of the maxima in the TRF. This means that the variations of the intensity distribution over the slit exit plane for a single angle of incidence are

(a) TRF at 400 nm (UV-VIS)

(b) TRF at 770 nm (SWIR-3)

(c) TRF at 2312 nm (NIR)

(d) TRF of a classical slit 770 nm (NIR)
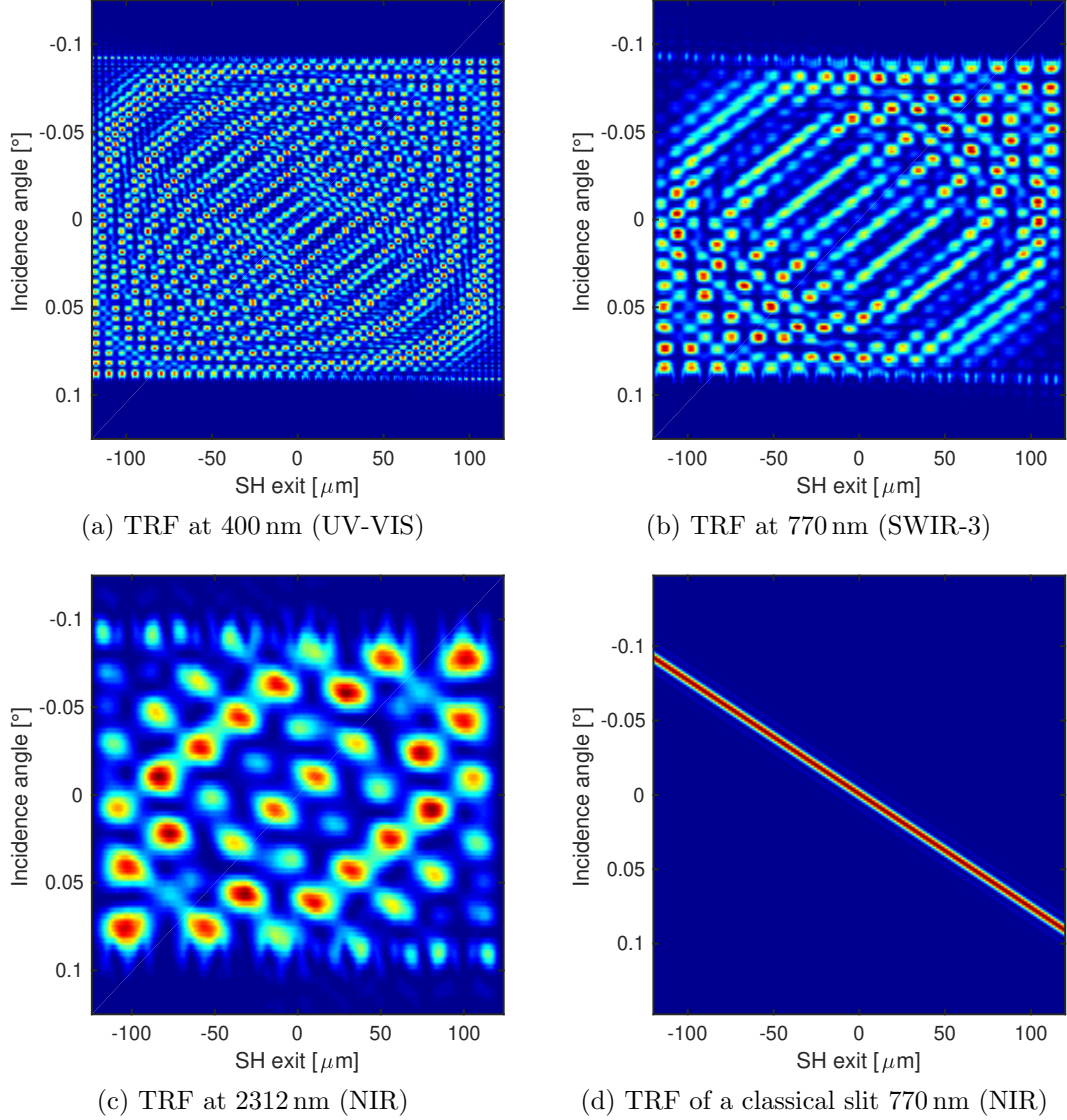
Figure 4.3: Transfer Function (TRF) of a SH. The TRF describes the response of the SH to an elementary stimulus at the SH entrance as a field distribution in the SH exit plane. An initially diffraction limited point source at the entrance is eventually distributed to the entire 1DSH exit plane. The fluctuations in the distribution are due to the interference of reflections within the 1DSH. The repetition of the intensity pattern maxima and the peak to valley amplitude are strongly dependent on the wavelength. (a) TRF at 400 nm (b) TRF at 2312 nm (c) TRF at 770 nm (d) TRF of a classical slit at 770 nm. In the case of a classical slit, the diffraction limited PSF of a SH incidence angle corresponds exactly to the SH exit intensity distribution and no homogenization takes place.

more homogeneous. The wavelength dependent homogenization capability is also determined by the relative size of the PSF with respect to the diffraction limit and the slit opening. The size of the diffraction limited PSF is determined by the wavelength and the telescope $F\#$ as $r_{PSF} = \lambda F\#$. The resulting size directly correlates to the size of the intensity peaks in the TRF. As a result, the 1DSH generally homogenizes heterogeneous scenes better at smaller wavelengths than at longer wavelengths. A full experimental validation of the propagation model through the 1DSH and the resulting TRFs is still missing. An initial approach to validate the model in a breadboard activity was conducted by ITO Stuttgart and published by Irizar et al. (2019).

4.3.4   Scene specification

In order to assess the spectral homogenization performance of the slit homogenizer, several heterogeneous scene cases are tested. The first is an applicable Earth scene as defined by the ESA for the Sentinel-5/UVNS mission, which aims at representing a realistic Earth scene case. The on-ground albedo variations of such scenes can be parametrized as a linear interpolation between two spectra, representing the same atmospheric state, but obtained with either a dark or bright albedo (Caron et al., 2017). The spatial variation of the scene heterogeneity is described by introducing interpolation weights w_k. The resulting spectrum for a given ALT subsample k is then calculated as:

$$L_k(\lambda) = (1 - w_k)\ L_{dark}(\lambda) + w_k\ L_{bright}(\lambda) \qquad (4.6)$$

where the reference spectra correspond to a tropical bright scene (L_{bright} - albedo = 0.65, SWIR3) and a tropical dark scene (L_{dark} - albedo = 0.05, SWIR3). The weighting factors that were used for this study have been derived from the Moderate Resolution Imaging Spectroradiometer (MODIS) surface reflectance products with 500 m spatial resolution and total coverage of 25 km for relevant conditions of Sentinel-5/UVNS (EOP PIO, 2011). The slit smearing due to platform movement

is accounted for by convolving the on-ground scene with the motion boxcar of the spatial sampling distance (SSD). The platform movement is acting like a low-pass filter and averages out fast albedo variations with respect to the SSD. However, without a SH, remaining inhomogeneities are present in the slit which yield up to 20% slit illumination variations in ALT direction. Figure 4.4 depicts exemplary the on-ground albedo contrast given in terms of weighting factors w_k in the NIR and SWIR-3, the scene after smearing due to the motion of the platform, and the location of the SH entrance plane. The scene is assumed to be homogeneous in ACT direction. The second scene considered represents an artificial calibration (CAL) scene where 50% of the slit is illuminated and 50% is dark. These kind of instantaneous transitions are impossible to be observed by a push-broom instrument with non-infinitesimal FoV and integration time. However, they are convenient to be applied in experimental measurements and will serve as reference to experimentally validate the 1DSH performance models. As described in section 4.3.6, it is also possible to convert the homogenization requirements from arbitrary complex Earth radiance scene to an experimental artificial CAL scene.

In the following, the homogenized slit exit illumination is projected onto the detector. For now, effects in the far field of the 1DSH are neglected and will be treated in a separate chapter at a later stage. Since the slit illumination is usually the driving factor in ISRF stabilities, the resulting ISRF stabilities are often referred to as first-order results.

4.3.5   First-order ISRF performance results

To quantify ISRF stability enhancement for some example Earth radiance scenes relevant to the Sentinel-5/UVNS instrument and for artificial CAL scenes, the TRF (see eq. (4.5)) of the 1DSH is mapped with the respective scene weighting onto the FPA. This is done in the following way: any spatially incoherent monochromatic input scene can be distributed in plane wavefronts with amplitude $A(\Theta)$. Each such wavefront leads to an intensity $I = I_\Theta(u_b, v_b) = TRF(\Theta)$ on the FPA. As we
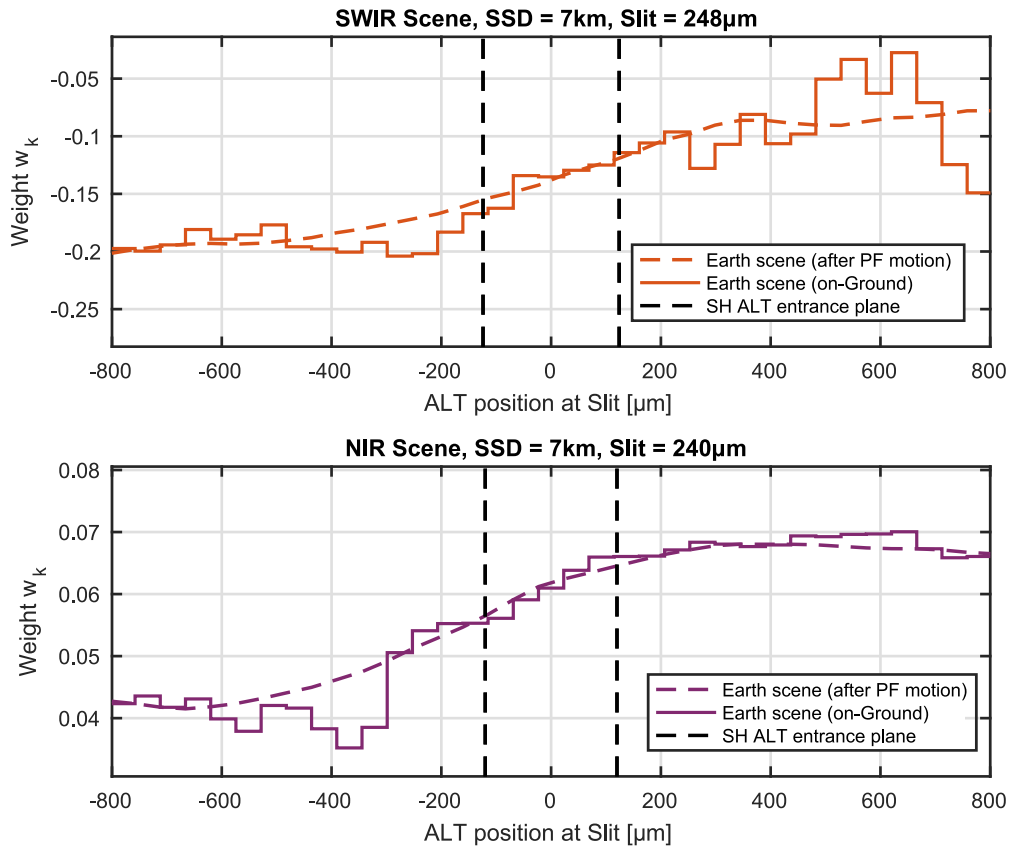
Figure 4.4:   Exemplary realistic Earth scenes in the SWIR-3 and NIR derived from MODIS images corresponding to the slit illumination in ALT. The on ground surface albedo is given in terms of weight factors w_k in the solid line. The same scene after smearing with a boxcar of the spatial sampling distance (SSD) accounting for the platform motion is given in the dashed line. The scene contrast including the platform motion in the plane of the SH entrance plane will be the reference scene for this study.

have no SH impact in ACT direction, we collapse this dimension and sum along it. This yields the 1D intensity distribution on the FPA as a function of the incidence angle Θ as $I_\Theta(v_b)$. The respective scene will weight the intensities on the FPA depending on their strength and is therefore the linear operator $\circ$:

$$I = \int_{\Theta \in \mathbb{R}} A(\Theta) I(\Theta, v_b) \, d\Theta = TRF \circ A(v_b) \tag{4.7}$$

Note that for a homogeneous scene, $A(\Theta) = 1$ for every incidence angle. Finally, the normalized ISRF on the FPA is given by:

$$\widetilde{ISRF}(v_b) = \left((TRF \circ A (v_b)) \left(\frac{1}{\gamma} \right) \right) \otimes \chi(v_b) \otimes N_\sigma(v_b) \tag{4.8}$$

$$ISRF(\lambda) = \frac{\widetilde{ISRF}(\frac{\lambda}{\alpha})}{\alpha \int \widetilde{ISRF}(v_b) \, dv_b} \tag{4.9}$$

where $\otimes$ is the convolution symbol, χ is the characteristic function, which is 1 inside a pixel area and 0 elsewhere, α a scaling factor to give the ISRF in units of wavelength (λ), N_σ is the density function of a normal distribution with zero mean value and standard deviation σ and γ is the spectrometer magnification factor which maps the SH output size onto the detector. The latter factor accounts for the modulation transfer function (MTF) of the detector (not the MTF of the whole optical system).

In order to asses the stability of the ISRF three merit functions are defined:

- Shape error, which is defined as the maximum difference of the ISRF calculated for a homogeneous and heterogeneous scene respectively:

$$\text{Shape error} := \frac{\max_\lambda |ISRF_{hom}(\lambda) - ISRF_{het}(\lambda)|}{\max_{\tilde{\lambda}} ISRF_{hom}(\tilde{\lambda})} \tag{4.10}$$

- Centroid error: Shift of the position of the spectral channel centroid, where

the centroid is defined as:

$$\text{Centroid error} := \frac{\underset{FPA}{\int} ISRF(\lambda)\ \lambda\ d\lambda}{\underset{FPA}{\int} ISRF(\lambda)\ d\lambda} \tag{4.11}$$

- Spectral resolution of the ISRF given by the FWHM

When optical aberrations are neglected, the PSF of the spectrometer is assumed to be a constant scene-independent normal distribution defined as:

$$g(v_b) = \frac{1}{\sigma\sqrt{2\pi}}\ exp\left(-\frac{v_b^2}{2\sigma^2}\right) \tag{4.12}$$

where σ is the standard deviation representing the size of the PSF. The size of the PSF or often called blur spot is determined by the aberrations present in the spectrograph. Here, we tune the size of the PSF by the parameter σ such that the size of the blur spot matches the respective Sentinel-5/UVNS spectrographs. Table 4.2 summarizes the ISRF result of the applicable Earth scenes, which aim at representing realistic Earth scenes and table 4.3 of an artificial 50% CAL scene as used in experimental verification measurements. The 1DSH homogenizes the input scene very effectively and improves the ISRF performance parameters by up to several orders of magnitude compared to a classical slit. One can also see a trend that the homogenization is even more effective at smaller wavelengths than at longer ones, which is related to the homogeneity and smoothness of the TRF. Only the NIR spectrometer does not quite fit this pattern. The reason for that could be that the spectrometers do not have exactly the same parameters. For example, the ratio between slit size on the detector to optical PSF size, which we assumed to be homogeneous, plays a role (see table 4.4). Furthermore the pixel pitch size on the FPA also affects the weight of the 1DSH NF on the ISRF.

In certain scenarios, Sentinel-5/UVNS will fly over Earth scenes with higher contrasts than specified in the applicable Earth scene. This will be the case when flying over cloud fields, water bodies or city to vegetation transitions. However, these

Spectral channel	Shape Error [%]		FWHM Error [%]		Centroid Error [nm]	
	SH	No SH	SH	No SH	SH	No SH
UV1 (310 nm)	0.008	0.697	0.001	0.017	$2.7 \cdot 10^{-5}$	$2.0 \cdot 10^{-3}$
UV2VIS (500 nm)	0.222	4.847	0.028	0.218	$2.6 \cdot 10^{-4}$	$1.1 \cdot 10^{-2}$
NIR (773 nm)	0.312	2.242	0.013	0.021	$5.9 \cdot 10^{-4}$	$4.0 \cdot 10^{-3}$
SWIR-1 (1660 nm)	0.158	2.064	0.019	0.301	$1.9 \cdot 10^{-4}$	$2.2 \cdot 10^{-3}$
SWIR-3 (2312 nm)	0.248	2.54	0.010	0.061	$3.0 \cdot 10^{-4}$	$3.0 \cdot 10^{-3}$

Table 4.2: ISRF stability results for representative Sentinel-5/UVNS Earth radiance scenes. The table includes the spectral performance comparison between an instrument with and without SH.

Spectral channel	Shape Error [%]		FWHM Error [%]		Centroid Error [nm]	
	SH	No SH	SH	No SH	SH	No SH
UV1 (310 nm)	0.558	90.892	0.005	47.658	$1.9 \cdot 10^{-3}$	$2.5 \cdot 10^{-1}$
UV2VIS (500 nm)	1.172	59.601	0.022	32.898	$3.2 \cdot 10^{-3}$	$1.2 \cdot 10^{-1}$
NIR (773 nm)	8.685	60.474	1.823	33.853	$1.6 \cdot 10^{-2}$	$9.7 \cdot 10^{-2}$
SWIR-1 (1660 nm)	6.496	80.541	2.668	39.070	$7.2 \cdot 10^{-3}$	$7.7 \cdot 10^{-2}$
SWIR-3 (2312 nm)	7.088	59.057	1.058	33.280	$8.8 \cdot 10^{-3}$	$5.9 \cdot 10^{-2}$

Table 4.3: ISRF stability results for an artificial 50% CAL scene. The table includes the spectral performance comparison between an instrument with and without SH.

scenes are excluded from the mission requirements in terms of scene homogenization. Although sufficient for the purposes of Sentinel-5/UVNS, the capability of the SH to homogenize the scene is not perfect. This imperfection is particularly prominent when considering the CAL scenes. The imperfections originate from the interference fluctuations in the SH transfer function which is clearly not completely smooth.

Spectral channel	UV1	UV2VIS	NIR	SWIR-1	SWIR-3
SH length	$9600\,\mu$m	$9600\,\mu$m	$9600\,\mu$m	$9910\,\mu$m	$9910\,\mu$m
SH width	$480\,\mu$m	$240\,\mu$m	$240\,\mu$m	$248\,\mu$m	$248\,\mu$m
Tel $F\#$	9.95	9.95	11.24	9.95	9.95
Spectr. magn.	0.38	0.36	0.37	0.15	0.15
Spectral Resolution $\Delta\lambda$	1 nm	0.5 nm	0.4 nm	0.25 nm	0.25 nm
Spectral sampling interval (SSI)	0.33 nm	0.17 nm	0.13 nm	0.1 nm	0.1 nm
Det. Pixel pitch	$30\,\mu$m	$30\,\mu$m	$30\,\mu$m	$15\,\mu$m	$15\,\mu$m
Det. OPSF size	$18.5\,\mu$m	$19.3\,\mu$m	$19.1\,\mu$m	$6.82\,\mu$m	$6.85\,\mu$m

Table 4.4: Spectrometer values used for the Sentinel-5/UVNS performance assessment.

4.3.6   Scene conversion

As mentioned earlier, it is difficult to recreate realistic earth scenes in the laboratory to test the performance of the 1DSH. Therefore, the calibration scenes will be used for this purpose. However, the spectral stability requirements of the ISRF are defined in terms of realistic earth scenes as seen by the instrument. In the following, a method is presented to convert the stability requirements of the ISRF from a realistic heterogeneous Earth scene to matching requirements of an artificial calibration scene.

The ISRF is the image of the 1DSH input on the FPA for a given input scene X and is calculated as:

$$ISRF = \frac{A(X)}{\int A(X)\,dx} \tag{4.13}$$

with

$$A\left(X\right) = \left(TRF \circ X\right) \otimes \chi \otimes N_\sigma \tag{4.14}$$

where TRF is again the Transfer function of the 1DSH, χ the characteristic function which is 1 inside an interval defined by the pixel width and 0 outside, and N_σ is the density function of the normal distribution. The applicable Earth scene (Es) (as depicted in eq. (4.6)), already convolved with the motion smear boxcar function, is proportional to the sum of a homogeneous scene and a heterogeneous scene:

$$X_{Es} = mX_{hom} + nX_{het} \tag{4.15}$$

where X_{hom} is a homogeneous slit entrance illumination and X_{het} is a heterogeneous slit illumination. Since scaling the scene doesn't change the ISRF, both sides can be scaled by a factor:

$$c = \frac{1}{m+n}$$

in order to achieve:

$$c\,n = 1 - c\,m \tag{4.16}$$

Defining $a = c\,m$, we get:

$$ISRF\left(X_{Es}\right) = ISRF\left(aX_{hom} + \left(1-a\right)X_{het}\right) \tag{4.17}$$

Due to normalization the ISRF is non-linear. However, we can write the ISRF of the realistic Earth scene as a convex combination of the ISRF of the homogeneous part of the scene and the heterogeneous part of the scene as:

$$ISRF\left(X_{Es}\right) = \tilde{a}ISRF\left(X_{hom}\right) + \left(1-\tilde{a}\right)ISRF\left(X_{het}\right) \tag{4.18}$$

with

$$\tilde{a} = \frac{a\int A\left(X_{hom}\right)dx}{a\int A\left(X_{hom}\right)dx + \left(1-a\right)\int A\left(X_{het}\right)dx} \tag{4.19}$$

The value $\tilde{a}$ describes the degree to which the realistic Earth scene is homogeneous.

The higher $\tilde{a}$, the more the realistic Earth scene corresponds to a homogeneous scene. Vice versa we have:

$$a = \frac{\tilde{a} \int A\left(X_{het}\right) dx}{\tilde{a} \int A\left(X_{het}\right) dx + \left(1 - \tilde{a}\right) \int A\left(X_{hom}\right) dx} \tag{4.20}$$

From eq. (4.19), it follows that the ISRF of any complex input scene can be split into a homogeneous and a heterogeneous part. The complex structure of the heterogeneous scene is not feasible to implement in laboratory experiments, and therefore it is difficult to verify that the 1DSH satisfies the spectral ISRF stability requirements. However, it is possible to convert the heterogeneous part of the realistic earth scene into a calibration scene. Therefore, an attempt is made to replace the realistic Earth scene by a calibration scene that can be tested in laboratory measurements, so that:

$$ISRF\left(X_{het}\right) \approx ISRF\left(X_{CAL}\right) \tag{4.21}$$

To do so, the calibration scene is moved in ALT direction (x) and the parameter $\tilde{a}$ is tuned in order to approximate:

$$
\begin{aligned}
ISRF\left(X_{Es}\right) &\approx \tilde{a}\, ISRF\left(X_{hom}\right) + \left(1 - \tilde{a}\right) ISRF\left(X_{CAL}\left(x\right)\right) \\
&= ISRF\left(a\, X_{hom} + \left(1 - a\right) X_{CAL}\left(x\right)\right)
\end{aligned}
\tag{4.22}
$$

Subtracting $ISRF\left(X_{hom}\right)$ on both sides and using eq. (4.10) yields for the ISRF shape error S_{CAL} and S_{Es}:

$$
\begin{aligned}
S_{CAL} &= \max_{x} \left| \frac{ISRF\left(X_{CAL}\left(x\right)\right) - ISRF\left(X_{hom}\right)}{\max\limits_{\tilde{x}} ISRF\left(X_{hom}\right)} \right| \\
&\approx \frac{1}{1 - \tilde{a}} \max_{x} \left| \frac{ISRF\left(X_{Es}\left(x\right)\right) - ISRF\left(X_{hom}\right)}{\max\limits_{\tilde{x}} ISRF\left(X_{hom}\right)} \right| \\
&= \frac{1}{1 - \tilde{a}}\, S_{Es}
\end{aligned}
\tag{4.23}
$$

Using eq. (4.20) and knowing that the ISRF is a function of wavelength (λ) on the

detector, we can determine the centroid error as:

$$C_{Es} \approx \int \lambda \; ISRF \left(a \; X_{hom} + (1-a) \; X_{CAL} \left(x \right) \right) \left(\lambda \right) \; d\lambda$$
$$= (1 - \tilde{a}) \int \lambda ISRF \left(X_{CAL} \left(x \right) \right) \left(\lambda \right) \; d\lambda \qquad (4.24)$$
$$= (1 - \tilde{a}) \; C_{CAL}$$

where it is applied that the ISRF centroid error for a homogeneous scene is 0. The FWHM criterion of the realistic Earth scene can be calculated by defining $\lambda_1 < \lambda_2$ such that:

$$ISRF \left(X_{Es} \right) \left(\lambda_i \right) \approx ISRF \left(a \; X_{hom} + (1-a) \; X_{Cal} \left(x \right) \right) \left(\lambda_i \right)$$
$$= \frac{1}{2} max ISRF \left(a X_{hom} + (1-a) X_{Cal} \left(x \right) \right), \quad \text{for } i = 1, 2 \qquad (4.25)$$

Then, the FWHM is given as:

$$FWHM_{Es} = \lambda_2 - \lambda_1 \qquad (4.26)$$

By comparing the difference in FWHM of the homogeneous scene with the realistic Earth scene, the FWHM error can be determined. In the following, this error will again be translated to a corresponding CAL scene. The ISRF differences on the left and right side of eq. (4.22) are small vertical differences of two functions $\Delta y_{CAL} = \frac{1}{1-\tilde{a}} \; \Delta y_{Es}$. The FWHM difference Δx corresponds to horizontal function differences with approximately:

$$\frac{\partial}{\partial \lambda} ISRF \left(X_{hom} \right) \left(\lambda_i \right) \approx \frac{\Delta y_i}{\Delta \lambda_i}, \quad \text{for } i = 1, 2 \qquad (4.27)$$

Here, the left side is the derivative of the homogeneous ISRF at points λ_i where the ISRF reaches half of its maximum, i.e.:

$$FWHM \left(ISRF \left(X_{hom} \right) \right) \left(\lambda_i \right) = ISRF \left(X_{hom} \right) \left(\lambda_2 \right) - ISRF \left(X_{hom} \right) \left(\lambda_i \right) \qquad (4.28)$$

Using the abbreviation $\partial_i := \frac{\partial}{\partial \lambda} ISRF\left(X_{hom}\right)\left(\lambda_i\right)$, we get:

$$
\begin{aligned}
FWHM_{Es} - FWHM_{hom} &= \Delta x_{Es,1} + \Delta x_{Es,2} \\
&\approx \frac{\Delta y_{Es,1}}{\partial_1} + \frac{\Delta y_{Es,2}}{\partial_2} \approx (1 - \tilde{a})\left(\frac{\Delta y_{CAL,1}}{\partial_1} + \frac{\Delta y_{CAL,2}}{\partial_2}\right) \\
&\approx (1 - \tilde{a})\left(\Delta x_{CAL,1} + \Delta x_{CAL,2}\right) \\
&= (1 - \tilde{a})\left(FWHM_{CAL} - FWHM_{hom}\right)
\end{aligned}
$$

$$(4.29)$$

This result lets us translate the FWHM error requirement of the realistic Earth scene to a stationary CAL scene.

Spectral channel	Earth scene ISRF requirement			50% CAL scene ISRF requirement		
	Shape [%]	Centroid [SSI]	FWHM [%]	Shape [%]	Centroid [SSI]	FWHM [%]
UV1 (310 nm)	2	0.02	1	153	1.53	77
UV2VIS (500 nm)	2	0.01	1	14	0.07	7
NIR (773 nm)	2	0.05	1	50	1.25	25
SWIR-1 (1660 nm)	2	0.06	1	69	2.07	34
SWIR-3 (2312 nm)	2	0.05	1	65	1.61	32

Table 4.5: Translation of ISRF stability requirements for a complex heterogeneous Earth scene to a experimentally measurable 50% CAL scene. The data for the Earth scene requirements are taken from the Sentinel-5/UVNS SRD (EOP PIO, 2011).

As an example, we set the CAL scene $X_{CAL}\left(x\right)$ to correspond to a slit illumination of 50%, i.e., 50% of the slit is illuminated and the other half remains dark. x is here defined as the center of the slit width b and therefore $x \in \left[-\frac{b}{2} + \frac{b}{4}, \frac{b}{2} - \frac{b}{4}\right]$. Table 4.5 summarizes the results. The table shows the translation of the Sentinel-5/UVNS

ISRF stability requirements for a realistic Earth radiance scene as characterized by ESA EOP PIO (2011) to an experimentally measurable stationary CAL scene of 50% slit illumination. Note that the specified ISRF stability requirements include heterogeneous scenes as well as any other errors sources that contribute to the ISRF stability, such as thermal and mechanical displacements after launch. Heterogeneous scenes are usually allocated only $\sim 10 - 40\%$ of the total ISRF error budget. The scene conversion results have been verified by checking the fitting validity of the difference between the derived ISRF for the CAL and the ISRF of the Earth scene by the following relation:

$$\Delta := \max_{x} \left| \frac{ISRF\left(X_{Es}\left(x\right)\right) - \left(aISRF\left(X_{hom}\right)\right) + \left(1-a\right)ISRF\left(X_{CAL}\left(x\right)\right)}{\max_{\tilde{x}} ISRF\left(X_{hom}\left(x\right)\right)} \right| \tag{4.30}$$

the approach seems justified, when $\Delta << |S_{Es}|$, which was checked for all the results.

Using the results of this chapter, it is possible to quantify the first-order performance results of the 1DSH for arbitrary Earth scenes. Furthermore, the results can be verified in laboratory measurements by a stationary calibration scenes and compared with the success criteria of arbitrarily complex heterogeneous earth scenes.

In the next chapter we will discuss second-order effects induced by the FF after the 1DSH.

4.4   1DSH Far-Field

In a space-based imaging spectrometer equipped with a classical slit acting as a field stop, a point source on the Earth surface enters the instrument as a plane wavefront with a uniform intensity over the telescope pupil. As this principle applies for every point source in a spatial sample on the Earth, the telescope pupil intensity homogeneity is independent of the radiance variation among the point sources in a spatial sample. Besides some diffraction edge effects in the slit plane, the telescope pupil intensity distribution gets retrieved in the spectrograph pupil (FF of the SH).

This is not the case when introducing a mirror based 1DSH. Existing 1DSH models (Meister et al. (2017) and Caron et al. (2019)) implement the spectrometer as a simple scaling factor and the ISRF on the FPA is obtained via the convolution of the 1DSH output intensity distribution, the pixel response implemented as a characteristic function and the spectrograph PSF. Here we model the propagation through the spectrograph more accurately by including the spectrograph optics, such as the collimator, a dispersive element and the imaging optics. In particular, the inclusion of these optical parts becomes important because the 1DSH not only homogenizes the scene contrast in the slit, but it also significantly modifies the spectrograph pupil illumination. A schematic diagram of the 1DSH behaviour and the instrument setup is shown in fig. 4.5. A plane wavefront with incidence angle Θ is focussed by a telescope on the 1DSH entrance plane.

In ACT direction, the light is not affected by the 1DSH. After a distance l, corresponding to the 1DSH length, the diffraction limited PSF at the 1DSH entrance plane is converted to the far-field pattern of the diffraction pattern. Independent of the applied scene in ACT, the telescope pupil intensity distribution in ACT is mostly retrieved again at the spectrograph pupil. The exact distribution of the spectrograph pupil illumination is affected by magnification factor and a truncation of the electric field at the 1DSH entrance plane, which leads to a slight broadening and small intensity variations with a high frequency in angular space (Berlich and Harnisch, 2017).

In ALT direction, the multiple reflections inside the 1DSH not only lead to a homogenized SH exit plane but also lead to a modification of the system exit pupil illumination. The exact modification of the spectrograph pupil intensity distribution depends on the initial SH entrance illumination. Following a first simple geometrical argument as discussed by Caron et al. (2019), we consider a point source at the 1DSH entrance. The rays inside the cone emerging from this source will undergo a number of reflections depending on the position of the point source and the angle of the specific ray inside the cone. The maximum angle is given by the telescope F-Number. With this geometrical reasoning it becomes
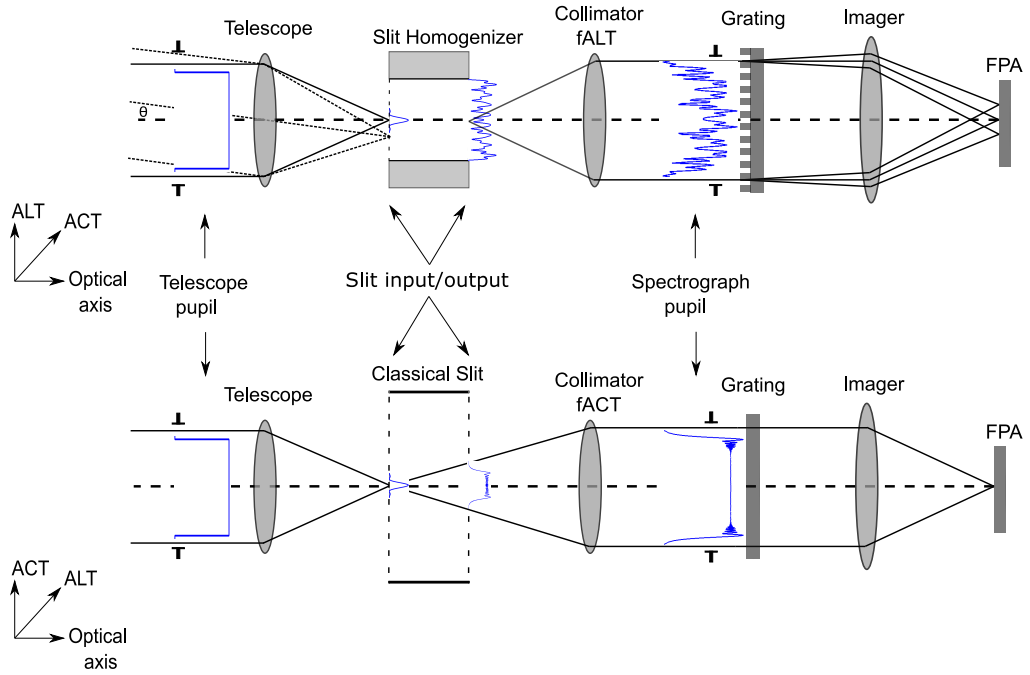
Figure 4.5: Generic setup of the 1DSH in the Sentinel-5/UVNS instrument. A plane wavefront gets focussed in the 1DSH entrance plane and the propagation of such stimulus is shown in blue as the square modulus of the electric field. The incoming light undergoes several reflections in ALT direction, whereas the 1DSH in ACT is similar to a classical slit acting as a field stop. The collimator contains an astigmatic correction which is adjusted to the slit length. The 1DSH homogenizes the scene in ALT direction but also modifies the spectrograph pupil illumination. The grating disperses the light in ALT. The pupil distribution in ACT direction is conserved except for diffraction effects due to truncation of the telescope PSF in the slit plane. Adapted from Hummel et al. (2021b).

obvious, that the number of reflections differs among the rays inside the cone. If the number of reflections is even, a ray keeps its nominal pupil position; whereas if the number is odd, its pupil coordinate will be inverted. From this argument we deduce that the spectrograph pupil illumination will be altered with respect to the telescope pupil illumination. Note that the reallocation of the angular distribution of the light has a different origin than the remaining inhomogeneity at the 1DSH exit plane. The achieved NF homogenization is dependent on the interference fluctuations in the SH transfer function. In contrast, the variations in the spectrograph illumination are based on a geometrical reallocation of the angular distribution of the light exiting the SH in combination with interference effects in the spectrograph pupil plane.

In the following the geometrical argument is made rigorous using diffraction theory. A general case for the connection between slit exit plane and spectrograph pupil plane is considered by eq. (3.25). In the scenario discussed there, a collimated input field $U_l(x_s, y_s)$ propagates through a perfect thin lens at a distance d. The field in the focal plane of the lens is then given by:

$$
\begin{aligned}
U_f(u_b, v_b) = & \frac{1}{i\lambda f}\; exp\left(i\frac{k}{2f}\left(1 - \frac{d}{f}\right)\left(u_b^2 + v_b^2\right)\right) \\
& \cdot \int_{-\infty}^{\infty}\int_{-\infty}^{\infty} U_l(x_s, y_s)\; exp\left(-i\frac{k}{f}\left(x_s u_b + y_s v_b\right)\right) dx_s dy_s
\end{aligned}
\tag{4.31}
$$

where x_s, y_s is the position in the spectrometer pupil plane, u_b, v_b the coordinates in the image plane at the 1DSH exit and f is the focal length of the collimator in ALT direction. Indeed, the field at the lens focal plane is proportional to the two-dimensional Fourier transform. In contrast, our situation is inverted as we are interested in $U_l(x_s, y_s)$, i.e. the collimated field distribution at the spectrometer pupil originating from the SH output plane. Applying $d = f_{col,ALT}$ and solving eq. (4.31) for $U_{l,\theta}$ by using the coordinate transformation $x'_s = \frac{k}{f}x_s$ and $y'_s = \frac{k}{f}y_s$

we get:

$$U_{l,\theta}\left(x'_s, y'_s\right) = \frac{i}{\lambda f} \cdot \int_{-\infty}^{\infty} \int_{-\infty}^{\infty} U_{f,\theta}(u_b, v_b) \ exp\left(i\frac{k}{f}(x'_s u_b + y'_s v_b)\right) du_b dv_b \quad (4.32)$$

Further, we need to incorporate the astigmatism in the collimation optics and the diffraction grating. These steps are covered in the following two subsections.

4.4.1 Collimator astigmatism

In order to keep the full image information in ACT, the focal plane of the telescope must be imaged. However, one would like to simultaneously use the homogenization of the SH in ALT, which requires that the SH output must be imaged in ALT. To achieve this, the collimator needs an astigmatism that allows the two separate focal planes to be imaged. In our model, this is implemented via Zernike polynomial terms on the collimation lens. The focal length of the collimator in ALT is such to image the 1DSH exit plane, while in ACT the 1DSH entrance plane is imaged. In the simulation this is realised with three terms: a focal length term where the focal length is that of the collimator in ALT, a defocus term to shift the object plane and an astigmatism term to separate the ALT (tangential) and ACT (saggital) object planes. Since the astigmatism Zernike term is radially symmetric, the sagittal and tangential focal planes become equidistant from the original focus. Since in our model we fix the focal length of the collimator to $f = f_{col,ALT}$ and the focal length in ACT should be $f = F_{ALT} + l$, we introduce an additional defocus term to place the focus of the collimator in the center of the SH, thereby mapping both planes of the SH. The Zernike polynomials of Defocus and Astigmatism are given by:

$$\text{Defocus:} \quad Z_2^0(\rho, \theta) = c_{02}\sqrt{3}(2\rho^2 - 1) \quad (4.33)$$

$$\text{Astigmatism:} \quad Z_2^2(\rho, \theta) = c_{22}\sqrt{6}\rho^2 sin(2\theta) \quad (4.34)$$

where c_{nm} are the Zernike coefficients, defining the strength of the aberration and Z_n^m the Zernike polynomials. The definition of the Zernike polynomials and the

indexing of the Zernike mods follows the OSA/ANSI convention as described in section 3.3.2. The orthonormal definition of the Zernike polynomials allows for an exact matching of Defocus and Astigmatism amplitude, as the difference between the sagittal and tangential plane of the astigmatism is solely dependent on the radial term of the Zernike polynomial. Therefore, in order to match the corresponding difference given by the 1DSH length, the weighting of the astigmatism has to be larger than the defocus term by a factor of $\sqrt{2}$. Hence, the combined Zernike term will be:

$$H(\rho, \theta) = c\ Z_2^0(\rho, \theta) + \sqrt{2}\ c\ Z_2^2(\rho, \theta) \tag{4.35}$$

Including the astigmatism of the collimation optics, we get the field distribution at the diffraction grating as:

$$
\begin{aligned}
U_{l,\theta}\left(x_s', y_s'\right) = &= \frac{i}{\lambda f} e^{ikH(\rho,\theta)} \\
&\cdot \int_{-\infty}^{\infty} \int_{-\infty}^{\infty} U_{f,\theta}(u_b, v_b)\ \ exp\left(i\frac{k}{f}(x_s' u_b + y_s' v_b)\right) du_b dv_b \\
&= \frac{i}{\lambda f} e^{ik\left(c\ Z_2^0(\rho,\theta) + \sqrt{2}\ c\ Z_2^2(\rho,\theta)\right)} \\
&\cdot \int_{-\infty}^{\infty} \int_{-\infty}^{\infty} U_{f,\theta}(u_b, v_b)\ \ exp\left(i\frac{k}{f}(x_s' u_b + y_s' v_b)\right) du_b dv_b
\end{aligned}
\tag{4.36}
$$

The implementation of the diffraction grating, which is responsible for the wavelength dispersion will be introduced in the next section.

4.4.2   Diffraction grating

The primary goal of the spectrometer is to distinguish the intensity of the light as a function of the wavelength. In order to separate the wavelengths a diffractive element is placed in the spectrograph pupil and disperses the light in the ALT direction. For our analysis, we place the diffraction grating at a distance $d = f_{col,ALT}$ after the collimator and on the optical axes. Further, we model the dispersive element as a 1D binary phase diffraction grating. Such gratings induce a π phase

variation by thickness changes of the grating medium. Three design parameters are used to describe the grating and are unique for every spectrometer band: the period of the grating Λ, the phase difference Φ between the ridge (of width d) and the groove regions of the grating, and the fill factor d/Λ. Physically, the phase difference itself is induced by two parameters: the height or thickness t of the ridge and the refractive index of the material of which the grating is made. In a simplified view, the refractive index of the used material is fixed and the thickness of the material is the primary parameter. The phase profile with a fill factor of 0.5 which provides the maximum efficiency in ALT direction is given by:

$$\Phi_{1D}\left(y_s\right) = \begin{cases} \pi & 0 \leq y_s \bmod \Lambda \leq \frac{\Lambda}{2} \\ 0 & \frac{\Lambda}{2} \leq y_s \bmod \Lambda \leq \Lambda \end{cases} \tag{4.37}$$

The complex electric field of the spectrograph pupil wavefront after the diffraction grating is then given by:

$$U_{g,\theta}(x'_s, y'_s) = U_{l,\theta}(x'_s, y'_s) \; e^{i\Phi_{1D}(y_s)} \tag{4.38}$$

The intensity distribution after the grating is given by inserting eq. (4.36) in eq. (4.38) and applying the absolute square:

$$I_{g,\theta}(x'_s, y'_s) = |U_{g,\theta}(x'_s, y'_s)|^2 \tag{4.39}$$

The implementation of the diffraction grating is a simplified model, which is an approximation of the real, more complex case. However, as the 1DSH does not affect the general behaviour of the grating this approach seems valid.

4.4.3 Spectrograph pupil intensity distribution

The FF intensity distribution is dependent on the contrast of the Earth scene in ALT and therefore on the 1DSH entrance plane illumination. As before, we characterize the amplitude of the variations of the spectrograph pupil illumination

by an applicable Earth scene as defined by ESA for the Sentinel-5/UVNS mission, which aims at representing a realistic Earth scene case (EOP PIO, 2011), and a stationary 50% CAL scene. As the SWIR-3 band is the most critical in terms of homogenization capabilities of the 1DSH, we constrain the analysis for FF induced ISRF variation to this spectral band. Figure 4.6 depicts the simulation results for

(a) Homogeneous scene SWIR-3

(b) Applicable Earth scene

(c) 50 % CAL scene - bottom

(d) 50 % CAL scene - top
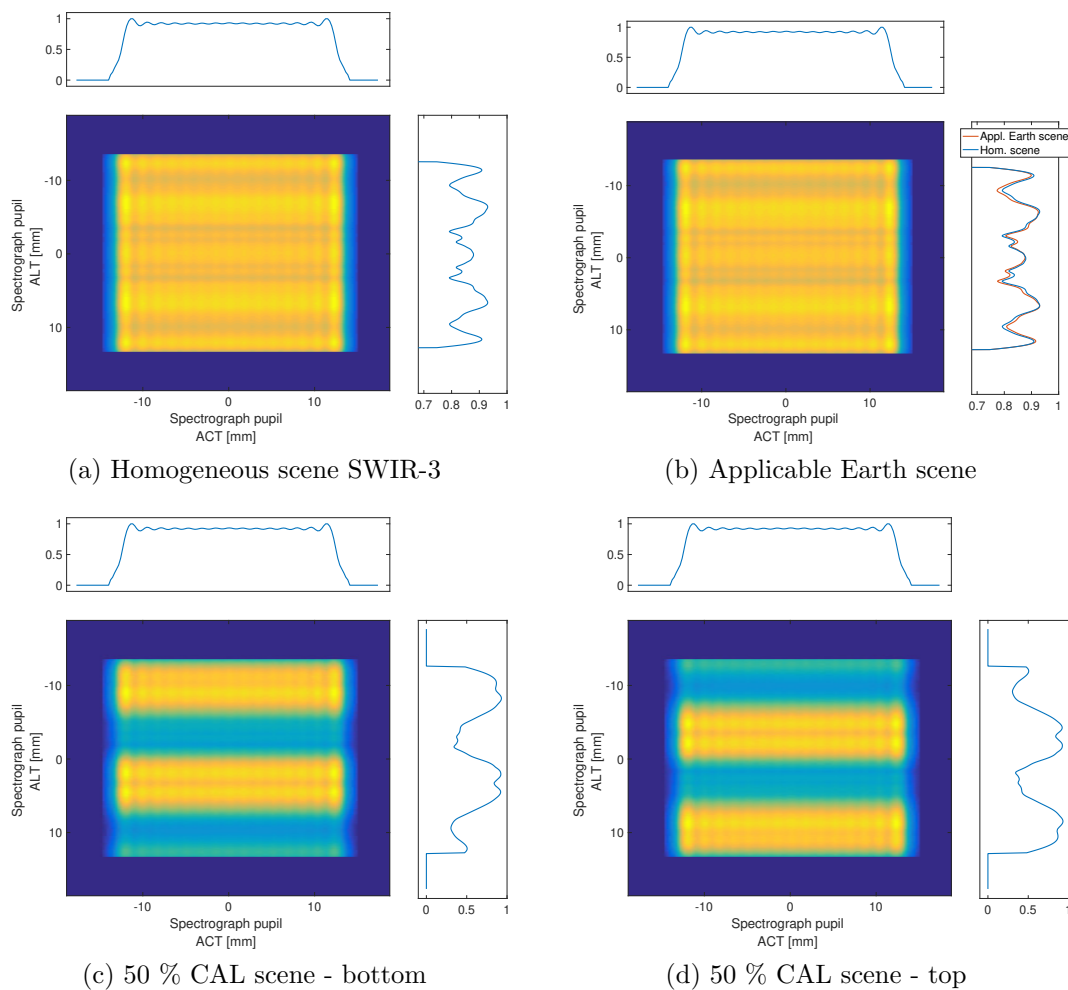
Figure 4.6: Simulation results of the spectrograph pupil intensity distribution in the SWIR-3 (2312 nm) for different slit illuminations. The uniformity of the pupil in ALT is dependent on the applied scene. The ACT uniformity from the telescope pupil is preserved, as there is no interaction with the 1DSH. Adapted from Hummel et al. (2021b).

the pupil intensity distribution at 2312 nm (SWIR-3) for the applied test scenes as well as a homogeneous slit illumination. As expected, the uniformity of the input telescope pupil illumination is completely conserved in ACT direction due to

the absence of interaction, i.e. reflection, with the 1DSH. Therefore the top-hat intensity distribution of the telescope is, besides diffraction edge effects, completely preserved. To the contrary, the intensity distribution in ALT is dependent on the contrast of the applied scene. Even for a homogeneous scene the 1DSH modifies the pupil intensity (fig. 4.6a) and consists of symmetrical variations. The intensity pattern just varies slightly for the applicable Earth scene (fig. 4.6b) due to the moderate gradient of the slit illumination variation. The lower panels show the case where only 50% of the entrance slit is illuminated. Here, fig. 4.6c shows the case where the lower 50% of the slit is illuminated and fig. 4.6d the case where the upper 50% of the slit is illuminated. These extreme cases illustrate the previously made geometrical arguments of the stripe pattern. Indeed, some parts of the pupil intensity distribution are nearly empty because the rays in the FF reallocate according to the symmetry of the input illumination in the SH entrance plane. The symmetry reverses when the symmetry of the input illumination is reversed. Note that the NF exit illumination also reverses according to the symmetry of the input illumination.

In the next section the impact of non-uniform pupil illumination in combination with spectrograph aberrations on the ISRF stability will be investigated.

4.4.4   FF impact on ISRF

The main impact of the above described variations in the spectrometer pupil illumination is the scene dependent weighting of the aberrations inherent to the spectrograph optics. In the case of a classical slit, it is valid to calculate the ISRF of an imaging spectrometer as the convolution of the slit illumination, the pixel response on the FPA and the optical PSF of the spectrograph optics. When using a 1DSH, a scene dependency of the spectrograph pupil illumination will weight the aberrations of the system accordingly and thereby create a variation in the PSF, which will ultimately also change the ISRF properties. Therefore, it is necessary to keep the complex phase of the electric field during the propagation through the

70

instrument.

Instead of a convolution, the spectrograph pupil illumination is propagated through the imaging optics by diffraction integrals. For the description of the aberrations present in the Sentinel-5/UVNS instrument the formulation of Zernike theory is used. The expected PSF size on the FPA of the Sentinel-5/UVNS SWIR-3 band is known, which in the case of a classical slit can be approximated by the standard deviation of a normal distribution. In order to assess the impact of aberrations, we impinge different types of aberrations on the spectrograph imaging optics and match the PSF size to the instrument prediction. As the shape of the PSF for an arbitrary aberration is not given by a normal distribution, the PSF size is defined as the area where 80% of the encircled energy (EE) is contained. Then, the strength of the aberration coefficients is tuned in such a way that the size of the aberrated PSF matches that of the normal distributed PSF. For the transformation of the spectrograph pupil illumination to the FPA including aberrations, the thin lens formula is applied and expanded by adding the phase term for the Zernike aberrations (see section 3.3.2). The starting point for the propagation is the grating position where, for the case of Sentinel-5/UVNS, the distance d is matching the focal length of the imaging optics. In that case the formulation simplifies again and is given by a relation which has the form of a Fourier transform:

$$
\begin{aligned}
U_{FPA,\theta}(s,t) = \frac{1}{i\lambda f_{im}} \int_{-\infty}^{\infty} \int_{-\infty}^{\infty} U_{g,\theta}(x'_s, y'_s) \; exp\left(-i\frac{k}{f_{im}}\left(x_s s + y_s t\right)\right) \\
\cdot \; exp\left(\frac{ik}{\pi} H(r,\phi)\right) dx_s dy_s
\end{aligned}
\tag{4.40}
$$

where s, t are the coordinates at the FPA, f_{im} is the focal length of the imager, $U_{g,\theta}$ the field distribution at the grating and $H(r,\phi)$, with $r = r(x_s, y_s)$ and $\phi = \phi(x_s, y_s)$, the respective Zernike aberration that is applied.

The calculation of the signal on the detector follows the same principle as done in section 4.3.5. Equation (4.40) is evaluated for distributed plane wavefronts with amplitude A_Θ. Propagation of the wavefronts through the spectrometer is done

individually for each SH entrance angle of incidence and all wavefronts are then summed at the detector. The scene radiance distribution will consequently weight the strength of the respective incidence angles. Collapsing again the ACT direction we end up with an intensity on the FPA in the used coordinate system as:

$$I_t = \int_{\Theta \in \mathbb{R}} A(\Theta) I(\Theta, t) \, d\Theta = I \circ A(t) \tag{4.41}$$

The definition of the ISRF and of the figures of merit determining the ISRF stability criteria remain the same as in section 4.3.5. The main difference by accounting for the FF 1DSH effects is that the ISRF is not convolved with a constant normal distribution representing the PSF. Instead, a certain amount of aberrations are impinged on the imaging optics to get the same blur spot size for the PSF as in the case of a constant normal distribution. In this case, the ISRF errors are a combination of the remaining inhomogeneities at the 1DSH exit plane (NF), as well as effects due to non-uniform spectrograph illumination (FF). The aberrations present in the Sentinel-5/UVNS spectrograph are dependent on the position on the FPA in spectral and spatial direction. In the upcoming characterization and calibration campaign, the specific types of aberration of the final instrument will not be determined, but only the size of the blur spots. Therefore, although it is not a realistic case, pure aberrations of a single type are impinged in order to determine critical Zernike terms for the ISRF stability. Further two mixtures of different types of aberrations are tested, which represent more realistic field points of Sentinel-5/UVNS. The ISRF for a homogeneous scene including aberrations, will be extensively characterized on-ground. Here it is investigated how the ISRF based on several Zernike terms behave under the condition of heterogeneous scenes and how the ISRF deviation evolves with respect to each, aberration type specific, homogeneous ISRF. Therefore, in the next paragraph, the relative change in the ISRF figures of merit functions is calculated.

4.4.5 1DSH performance results including FF

In the following, the ISRF figures of merit resulting from the simulation of several Zernike polynomials for the Sentinel-5/UVNS applicable heterogeneous Earth scene and a 50% stationary CAL scene are presented. As before, the ISRF errors are based on the differences of the respective ISRF of a homogeneous and a heterogeneous scene. Further, the results are again compared to the case of a classical slit without scene homogenization. Tables 4.6 and 4.7 summarize the results for the ISRF figures of merit. All Zernike polynomials increase the error in the ISRF knowledge compared to the case, where the ISRF is calculated as the convolution with a constant gaussian PSF. The error magnitude variation ranges from only small increasing errors (Defocus, Vertical astigmatism) to a notable increase of the error (Oblique quadrafoil, Horizontal Coma). The aberrations change both the maximum amplitude of the errors and the specific shape of the ISRF. Figure 4.8 depicts the ISRF assuming pure vertical coma, pure spherical aberrations and pure oblique trefoil for a heterogeneous 50% calibration scene. The lower part of the plot shows the ISRF shape difference for each specific homogeneous reference scene. Note, that the shape error is defined as the maximum amplitude of the difference plot. As none of the field points in the real Sentinel-5/UVNS instrument will contain a pure singular type of aberration, additionally two sets of aberration mixtures are tested, which is more representative of a real field point in the Sentinel-5/UVNS instrument.

Although this study doesn't provide a rigorous mathematical argument, the results indicate, that the error of the combined Zernike polynomials lies within the errors of the individual contributors. This argument is supported by fig. 4.7, where the ISRF shape error is plotted, e.g. in the transition from a pure Oblique Quadrafoil aberration to a pure Defocus aberration (fig. 4.7a). In each step, the fraction of the Oblique Quadrafoil aberration was reduced by 20% and the defocus aberration coefficient was adjusted to yield the same PSF size of $6.85\,\mu$m (80% EE). The ISRF errors always remain in the corridor between the case of pure

(a) Oblique Quadrafoil - Defocus

(b) Vertical Coma - Defocus

(c) Oblique Quadrafoil - Primary Spherical
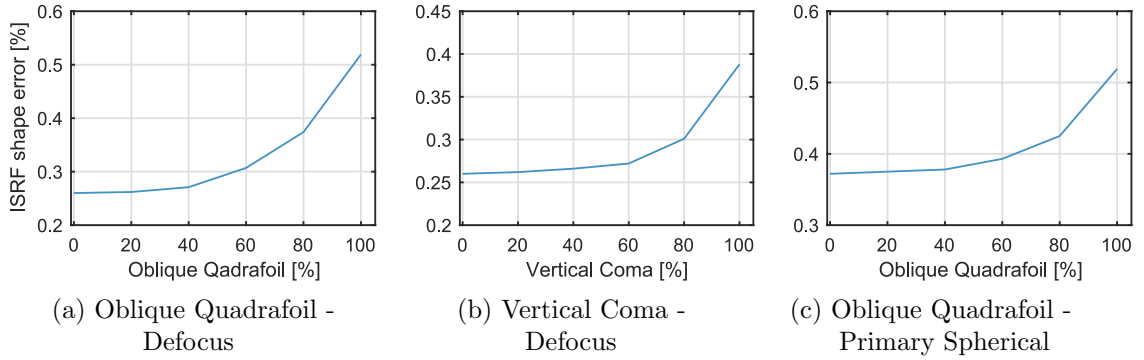
Figure 4.7: Progression of ISRF shape error (a) from pure Oblique Quadrafoil aberration to pure Defocus aberration (b) from pure Vertical Coma to Defocus (c) from pure Oblique Quadrafoil to primary spherical. Between the values, one Zernike coefficient is decreased in 20% steps and at the same time, the other coefficient is adjusted to reach the PSF design size of $6.85\,\mu$m again. The plots suggests that the ISRF errors of Zernike combinations are within the ISRF errors of the individual Zernike contributors.

Figure 4.8:   Comparison between the ISRF shape errors for three exemplary aberrations. The presented aberrations induce a higher maximum shape error but also strongly change the overall shape of the ISRF with respect to the homogeneous reference case. Adapted from Hummel et al. (2021b).

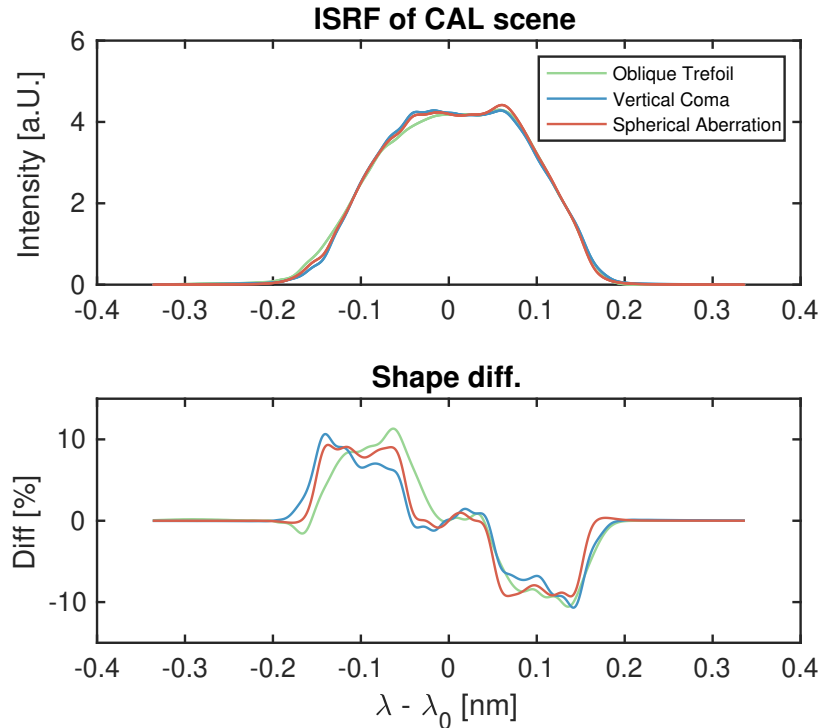| OSA/ANSI Index	Zernike Term	Shape Error [%]	FWHM Error [%]	Centroid Error [nm]
3	Oblique astigmatism	0.344	0.056	0.0003
4	Defocus	0.260	0.023	0.0002
5	Vertical astigmatism	0.260	0.023	0.0002
6	Vertical trefoil	0.409	0.020	0.0002
7	Vertical coma	0.388	0.032	0.0003
8	Horizontal coma	0.490	0.055	0.0003
9	Oblique trefoil	0.451	0.103	0.0003
10	Oblique quadrafoil	0.519	0.017	0.0003
11	Oblique second. astigmatism	0.398	0.011	0.0003
12	Primary spherical	0.372	0.040	0.0003
13	Vertical second. astigmatism	0.382	0.040	0.0003
14	Vertical quadrufoil	0.380	0.030	0.0003
Mixture 1 - Defocus (33%) / V. astig. (33%) / Prim. sph. (33%)		0.334	0.017	0.0002
Mixture 2 - O. astig (36 %) / V. coma (32 %) / O.s. astig (32 %)		0.382	0.040	0.0002
With SH - Gaussian PSF		0.248	0.010	0.0003
Classical Slit - Gaussian PSF		2.54	0.061	0.0030

Table 4.6: Applicable Earth scene - ISRF stability. Requirements: Shape error < 2%, FWHM error < 1%, Centroid error 0.0125 nm. The presented errors combine the remaining 1DSH exit non-uniformity (NF) and effects due to the variations of the spectrograph pupil illumination (FF). The strength of the aberrations are chosen such that the spot size matches the case of a PSF size of 6.85 μm (80% EE). Adapted from Hummel et al. (2021b).

OSA/ANSI Index	Zernike Term	Shape Error [%]	FWHM Error [%]	Centroid Error [nm]
3	Oblique astigmatism	8.507	1.589	0.008
4	Defocus	6.883	0.884	0.004
5	Vertical astigmatism	6.883	0.884	0.004
6	Vertical trefoil	9.230	0.833	0.008
7	Vertical coma	9.320	2.025	0.008
8	Horizontal coma	11.549	2.250	0.008
9	Oblique trefoil	11.320	0.566	0.008
10	Oblique quadrafoil	11.859	3.316	0.008
11	Oblique second. astigmatism	10.059	3.750	0.008
12	Primary spherical	10.686	0.382	0.008
13	Vertical second. astigmatism.	11.136	0.465	0.008
14	Vertical quadrufoil	10.127	0.928	0.008
Mixture 1 - Defocus (33 %) / V. astig. (33 %) / Prim. sph. (33 %)		7.367	0.442	0.004
Mixture 2 - O. astig (36 %) / V. coma (32 %) / O.s. astig (32 %)		9.982	0.849	0.008
With SH - Gaussian PSF		6.363	0.566	0.008
Classical Slit - Gaussian PSF		65.664	37.039	0.059

Table 4.7: 50% CAL scene - ISRF stability. The presented errors combine the remaining 1DSH exit non-uniformity (NF) and effects due to the variations of the spectrograph pupil illumination (FF). The strength of the aberrations are chosen such that the spot size matches the case of a PSF size of $6.85\,\mu$m (80% EE). Remark: ISRF values are exaggerated with respect to real flight scenarios. Calibration scenes are used for on-ground SH performance validation. Adapted from Hummel et al. (2021b).

oblique quadrafoil and pure defocus aberration. This behaviour was tested for other combinations of Zernike polynomials such as vertical coma and defocus (fig. 4.7b), as well as Oblique Quadrafoil and Primary Spherical (fig. 4.7c). From that it can be concluded that the errors given in tables 4.6 and 4.7 for the respective Zernike polynomials span the error space, where mixtures of aberrations lie within.

We observe, that increasing the number of reflections inside the 1DSH will increase the number of stripes in the spectrometer pupil illumination (see figs. 4.6c and 4.6d) and reduce the peak to valley amplitude. This would lead to a more homogeneous pupil illumination. More reflection in the 1DSH can be achieved by either increasing the length of the SH or adapting the telescope $F\#$. However, it is advantageous to keep the 1DSH length small to reduce the collimator astigmatism requirements. Note, that a longer 1DSH would not increase the NF homogenization performance. In addition, more reflections in the 1DSH lead to greater transmission losses at the mirrors. As the errors due to the pupil illumination are small compared to achieved NF homogenization, it seems favourable to prioritize the first-order length design rule given in Caron et al. (2019) and Meister et al. (2017). The 1DSH shows the best NF homogenization performance if $F\#_{tel} = l/(2bn)$, where $F\#_{tel}$ is the telescope F-number, l the 1DSH length, b the SH width and n the number of reflections. For Sentinel-5/UVNS, the optimal parameters for SWIR-3 are a telescope $F_{\#}$ of 9.95, a slit length of 9.91 mm and a slit width of 248 μm.

Although the phenomena of the variations of the pupil illumination in combination with spectrometer aberrations increases the errors, the 1DSH still homogenizes the scene well, and significantly improves the stability of the ISRF compared to a classical slit. In the case of Sentinel-5/UVNS, the 1DSH meets the mission ISRF stability mission requirements over applicable Earth scenes. This would not be the case for an instrument equipped with a classical slit.

4.5   Conclusion

This part of the thesis continued the investigation by Caron et al. (2019) and Meister et al. (2017) on the mirror based 1DSH technology. Using diffraction integrals, a model was presented showing the superior ISRF stability performance of the 1DSH over heterogeneous scenes compared to a classical slit. The ISRF errors with respect to several figure of merit functions were reduced by at least an order of magnitude. This will enable the Sentinel-5/UVNS instrument to determine chemical atmospheric composition with high accuracy even over heterogeneous Earth scenes.

While the preceding studies were considering the homogenization of the 1DSH exit plane, here, the models are extended by including the electric field propagation through the subsequent spectrograph. The 1DSH not only homogenizes the slit illumination, but also modifies the spectrograph pupil illumination dependent on the input scene. The variations in the spectrograph pupil illumination will lead to a scene dependent weighting of the geometrical aberrations in the optical system, which cause an additional distortion source of the ISRF. The phenomena is particularly prominent in the presence of extreme on-ground albedo contrasts. This will be the case, when the instrument flies over clouds or water bodies. However, in the context of the Sentinel-5/UVNS instrument, these scenes are excluded from the mission requirements.

The impact of spectrograph pupil illumination variations is small compared to the error due to non-uniform slit illumination and the ISRF distortion is primary driven by the remaining NF variations after the 1DSH. The inhomogeneity remnants arise from the fluctuations of the interference pattern at the SH exit plane. The strength of the variations is increasing with wavelength. Therefore, the FF analysis was conducted in the SWIR-3 band in order to cover the worst case.

We quantify the ISRF in terms of shape error, FWHM error and centroid error at 2312 nm by an end to end propagation through the SH and the subsequent spectrograph optics. The ISRF errors are based on the differences of the respective

ISRF of a homogeneous and heterogeneous scene. With regard to these figures of merits, our simulation results suggest an increase of the errors depending on the specific type of aberrations impinged on the optics. ISRF errors of combined Zernike polynomials matching the same PSF size are always within the maximum errors of the individual Zernike constituent. Although the SH changes the spectrometer illumination, it still has significant performance advantages in stabilizing the ISRF compared to a classical slit. For an applicable heterogeneous Earth scene, the SH improves the ISRF shape stability by a factor of 5-10. The remaining residual errors in the SWIR-3 band are well below the Sentinel-5/UVNS system requirement, which are: shape error 2%, the relative FWHM error $< 1\%$ and the centroid error $0.0125\,\mathrm{nm}$.

5 Fibre-based 2D-Slit Homogenizer (2DSH)

In the previous chapter, a 1DSH concept was presented that scrambles the light only in the ALT dimension (1D). The measurement of anthropogenic CO_2 from space imposes increased performance requirements on the slit homogenizer technique compared to atmospheric chemistry missions such as Sentinel-5/UVNS, which cannot be met with the 1DSH. The upcoming CO2M mission will be the first Earth observation mission deploying a new kind of slit concept based on fibre waveguides. This chapter presents a suitable and efficient concept for a 2D-Slit Homogenizer based on multimode fibres. First, in section 5.1, a brief introduction to the CO2M mission is given. Section 5.2 describes an experimental test setup, capable of evaluating the scrambling performance of the 2DSH. In section 5.3 a predevelopment sample of a fibre-based 2DSH is presented. Then, the homogenization capabilities of such a device in NF and FF are experimentally determined and presented in section 5.4. Finally, section 5.5 discusses a characteristic disadvantage of using fibre-based input slits and outlines the implications for instrument layout and radiometry.

> Substantial parts of the text in this section as well as many figures are adopted from two articles published by the author of this thesis. The first article was published in the CEAS Space Journal (Hummel et al., 2022) and the second as a conference proceeding for the ICSO conference 2021 (Hummel et al., 2021a).

5.1 The CO_2 Monitoring Mission - CO2M

In response to the 2015 United Nations Climate Change Conference, a satellite constellation was proposed to accurately quantify anthropogenic greenhouse gas emissions at both regional and global scales. Since the majority of man-made greenhouse gas emissions comes from point sources, such as coal-fired power plants and larger cities, it is of utmost importance to measure and track trends in these

emissions. In order to provide policy makers with actionable information on the evolution of emissions and, in particular, to assess the effectiveness of the emission reduction measures and regulations put in place, a satellite constellation optimized for monitoring anthropogenic CO$_2$ emissions with high spatial resolution and revisit frequency was proposed.

The CO$_2$ Monitoring Mission (CO2M) aims to quantify sources and sinks of carbon dioxide (CO$_2$) and methane (CH$_4$) by measuring their concentration in the atmosphere. The concentration is measured in terms of their column-averaged dry air mole fractions (XCO$_2$). In order to differentiate anthropogenic CO$_2$ emissions from biogenic CO$_2$ fluxes, an instrument was proposed, which is capable of observing XCO$_2$ at a precision (repeatability) of < 0.7 ppm, with a systematic accuracy (systematic bias) of 0.4 ppm and with a spatial sampling resolution of 2 km x 2 km (ESA, 2020). The mission consists of a total of four instruments: the NO$_2$ imager (NO2I), operating in the visible spectral range ($405 - 490$nm), the multi-angle polarimeter (MAP), measuring and characterizing the aerosol contribution in the atmosphere, a high-resolution cloud imager (CLIM), detecting cloud contamination within a spatial sample and the CO$_2$ imager (CO2I), measuring the spectral radiances and solar irradiance in the NIR ($747 - 773$ nm), SWIR-1 ($1595 - 1675$ nm), and SWIR-2 ($1990 - 2095$ nm). Similar to Sentinel-5/UVNS, CO2I is also operating in a push-broom configuration. Identifying plumes of elevated CO$_2$ requires high single-sounding precision without regional and temporal averaging (Kuhlmann et al., 2020). The stringent precision and accuracy requirements correspond to only 0.1% of today's typical CO$_2$ background values around 400 ppm. This, along with the small ground sampling distance (2 km), corresponding to a significant fraction of the IFOV in ALT direction, leads to a higher sensitivity of the CO2I instrument to ISRF distortion than atmospheric chemistry missions like Sentinel-5/UVNS. The CO2M requirement for ISRF stability over scenes with sharp contrast, i.e. a sudden transition from bright to dark irradiance in the centre of a spatial sample, requires the ISRF in-flight shape knowledge to be better than 1.5% and the position of the spectral channel centre shall be known with an accuracy better than 0.002 nm (NIR)

(ESA, 2020). Simulations indicate, that these ISRF stability requirements under sharp contrast scenes cannot be met with the 1DSH model implemented in the Sentinel-5/UVNS instrument (Hummel et al., 2021b). Furthermore, the sensitivity of XCO_2 retrieval to topography imposes extremely strong requirements on the spatial co-registration between spectral channels of 5% of the SSD (Sierk et al., 2019). This accuracy is necessary, as several data products of the three simultaneously measured channels (NIR, SWIR-1, SWIR-2) are required to determine the XCO_2 retrieval. Therefore, any spatial mismatch between the channels would lead to further XCO_2 error contributions.

In order to address both critical requirements, ISRF stability and spatial co-registration, a new slit concept called 2D-Slit Homogenizer (2DSH) was investigated. In this concept, the classical slit is replaced with a bundle of multimode fibres. The dimension of each rectangular fibre core in ALT defines the spectral extent of the slit and the dimension in ACT represent the spatial sampling. The full swath width is given by the total size of the adjoined fibres in ACT direction. Compared to the 1DSH from Sentinel-5/UVNS, in addition to the spectral direction, piece-wise homogenization is now also performed in ACT direction. The heritage of efficient scrambling capabilities of multimode fibres and the application as spectrograph entrance slits originates from on-ground radial velocity (RV) spectrographs such as for example CARMENES (Stürmer et al., 2014), HARPS (Pepe et al., 2002) or ESPRESSO (Pepe et al., 2010). Initial concepts of using a 2DSH for space-based imaging spectrometers were proposed by Guldimann and Minoglou (2016) and the performance characterized by Amann et al. (2019). Here, the above studies are extended and further implications on the optical system when using a 2DSH are determined. Besides the unprecedented stabilization of the slit illumination, several drawbacks and efficiency parameters have been identified, namely the phenomena of Focal Ratio Degradation (FRD), the dependency of the scrambling efficiency on the fibre length or the modification of the spectrograph pupil intensity distribution due to heterogeneous scenes. In the following, a concept for a fibre-based slit concept for space-based imaging spectrometers is presented and key parameters for

an efficient fibre scrambling performance in the near-field (NF) and far-field (FF) are investigated.

5.2   Experimental setup

To probe the fibre characteristics for non-uniform illumination, an experimental setup was designed and constructed, which allows to detect either the NF or FF pattern of light transmitted through the fibre, while precisely controlling the illumination pattern inserted into the fibre. A schematic overview of the setup is given in fig. 5.1 and the naming and description of the used optical components is given in table 5.1. Depending on the spectral band of interest, different coherent and incoherent light sources were used to probe the fibre. Tunable lasers were used as monochromatic light sources. The light source of choice for the corresponding test is connected to an input port of the integrating sphere via an optical fibre. The integrating sphere ensures a homogeneous intensity distribution of the beam across the telescope pupil plane. However, when using monochromatic laser light, the surface roughness of the sphere's internal material leads to a speckle pattern in the emitted beam. To get rid of this effect, a speckle reducer is mounted at the output opposing the regular beam output. The speckle reducer itself consists of diffusing material (Spectralon) placed just outside the integrating sphere and mounted on a rotor which is continuously spun by a motor. The rotating diffuser material eliminates the spatial coherence by averaging over the detector integration time and thus significantly reduces the amplitude of the averaged speckle patterns. A field stop, that is adjustable in two-dimensions and placed on the regular beam output secures full control over the shape and size of the emitted beam. This controls the illumination pattern at the image plane, which is later coupled onto the fibre. A lens (lens 1) with a 250 mm focal length collimates the beam from the light source assembly. The collimated beam is divided by a 50-50-beam-splitter. The transmitted part is sent through an adjustable aperture and imaged telecentric onto the fibre facet by a lens with a 25 mm focal length. The telecentricity ensures
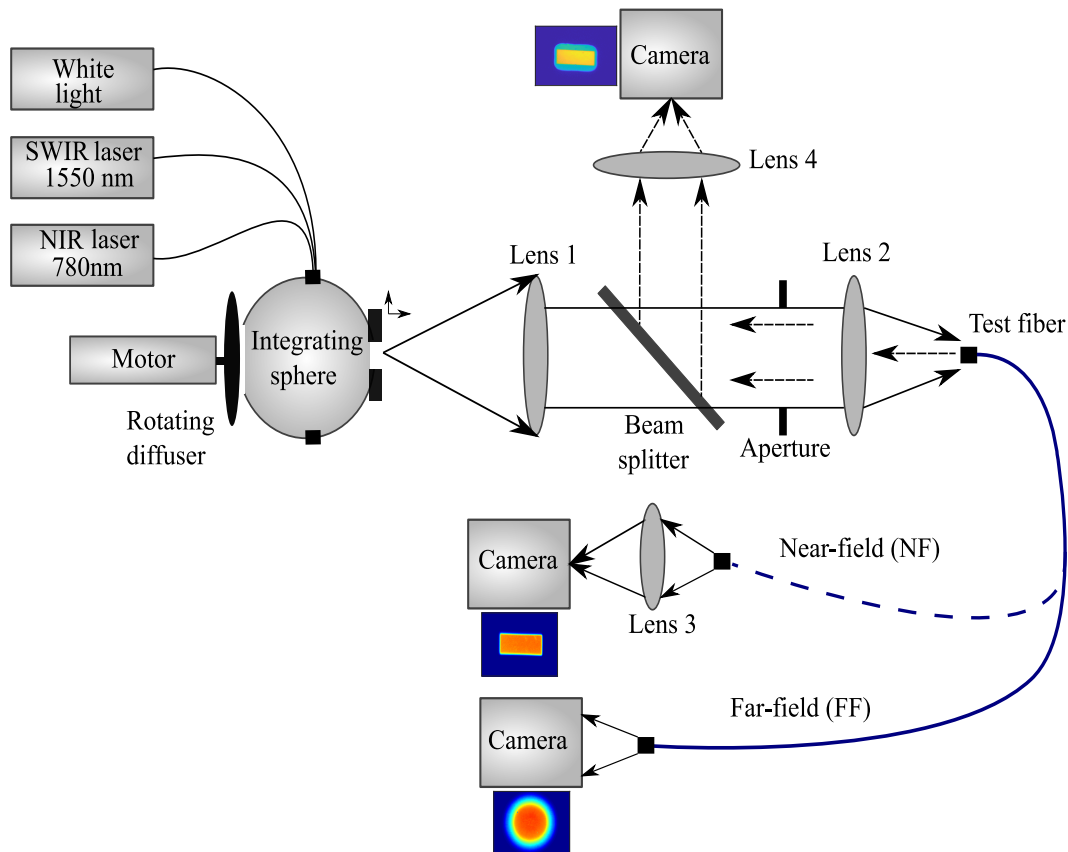
Figure 5.1: Sketch of the fibre-test setup. Next to each camera, associated false colour images are displayed. The dashed blue line indicate optional fibre-connection for near-field (NF) or far-field (FF) measurements. Adapted from Hummel et al. (2022).

Optical component	Type and description
White light	Thorlabs OSL2 fibred halogen lamp (3200 K)
SWIR laser	Toptica CTL 1550, Tuning range 1550 nm..1630 nm
NIR laser	Sacher-Laser, Tuning range 755 nm..785 nm
Integrating sphere	Thorlabs IS236A-4 2" integrating sphere
Adjustable stop	OWIS SP40
Beam-splitter	BSW $\varnothing$1" 50:50 UVFS Plate Beamsplitter
Lens 1	Edmund Optics # 49-366 achromatic lens f = 250 mm
Lens 2	Thorlabs AL 1225H-B/J-C $\varnothing$12.5 mm Diffraction limited Asphere, NA = 0.2
Lens 3/4	Olympus RMS x4 magnification, 0.1 NA
Camera (NIR)	Basler ACA1600-20um, 1236x1626 pixels, 4.4 μm pixel size
Camera (SWIR)	Photonic science ViSWIR InGaAS Camera, 640x512 pixels, 15 μmx15 μm pixel size

Table 5.1: Naming and description of the laser sources, detectors and optical components used in the measurements.

that each point at the fibre entrance receives the same cone of light. Tuning the diameter of the aperture allows us to change the F-number ($F\#$) of the beam-cone sent onto the fibre tip. NF images are obtained by projecting the exit facet of the fibre on a sensor. The projection is performed with a microscope objective and an achromatic lens both mounted in a tube system (lens 3 in fig. 5.1). FF images are obtained with a bar camera sensor located at a known distance from the fibre exit. The distance is much larger than the typical fibre core size and features no optics between the fibre exit and the sensor (free space propagation). Light reflected by the fibre tip (front facet), as well as light coupled into the fibre and reflected by the facet on the back site is again collimated by lens 2. This reflected beam is sent onto the beam-splitter and the reflex is imaged via another 4-fold magnification microscope objective (identical to lens 1). The NF image of the fibre front facet allows to monitor the illumination pattern on the facet when tuning the stop on the light source assembly. The light reflected at the backside of the fibre appears as a homogeneous illumination of the fibre core due to the scrambling.

The brighter reflection of the illumination pattern on the front facet overlays the faint core illumination from the fibre output side and can be precisely tuned with the adjustable stop on the light source assembly over the entire facet (including cladding).

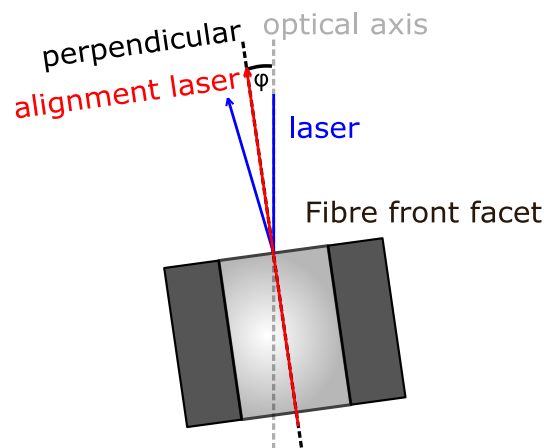The alignment of the tested fibre to the optical axis of the setup is crucial for

Figure 5.2: Criterion for the alignment of the fibre's front facet to the optical axis of the setup. The Helium-Neon-alignment-laser beam, coupled to the backside of the fibre, is depicted in red and the irradiated white light (or laser light during measurements) beam is depicted in blue. Dashed lines mark the normal to the front facet (black) and the optical axis of the setup (grey), presented here with an angle φ.

the conducted investigations. In order to simplify the alignment procedure and to secure the required precision, a Helium-Neon-laser (HeNe-laser) with its emission line at $\lambda = 632.8\,\mathrm{nm}$ was used as a reference beam. This laser beam is coupled into the back side of the testicular fibre and thus guided through the setup from the fibre to the integrating sphere. At the same time, light from the regular white light or laser source is used to superimpose the red laser beam. Centring these beams onto each other throughout the setup by aligning the fibre angles secures a precise alignment of the fibre surface to the optical axis. The foundation for this alignment criterion is the angular difference between transmitted and reflected light on the

fibre's front facet, shown schematically depicted in fig. 5.2. If there is an angular misalignment between the optical axis of the setup and the normal to the fibre's front facet with an angle φ, the two beams cannot be centred on each other. This behaviour is due to the fact that the HeNe laser beam is emitted at an angle φ with respect to the optical axis, while the reflection at the fibre facet detected by a camera in the setup is reflected at an angle $2 \times \varphi$. Tuning the angles on the fibre mount allows to align the beams with respect to each other and once the beams are centred on each other, the fibre facet is properly aligned since $\varphi \approx 0$.

5.3   2D-Slit Homogenizer

In this study, two different lengths of rectangular core COTS fibres provided by Optec were tested. They share the same core dimension of $300 \times 100 \ \mu m \pm 2\%$ (ACT/ALT) and a cladding of 350 x 180 $\mu m \pm 2\%$ (ACT/ALT) (see fig. 5.3). One set of fibres is 5 $cm \pm$ 0.3cm long and the other set is 100 $cm \pm 5 \ mm$ long. All the tests in this study have been repeated and confirmed with a representative pre-development model of a 2DSH sample, consisting of 25 adjoined multimode fibres of 100 cm as shown in fig. 5.4. The depicted 2DSH sample is made of two optical heads. One is mounted at the telescope image plane, and the other on the spectrometer object focal plane. They are connected by the bundle of fibres. Within each optical head, the ribbon of fibres shaping the slit is bonded on a silica plate with NOA-88 UV adhesive. On the spectrometer side, the silica plate is polished with a small radius of curvature for smile correction. Depending on the instrument design and the mission requirements, the 2DSH entrance and exit plane can be slightly curved to compensate smile effects on both, the spectrometer and telescope side. This is achieved by assembling the fibre core positions of the bundle in a parabolic shape instead of a straight line. A potting epoxy sealant is used to guarantee global stability of the fibres. Moreover, a second silica plate is glued on top to form the silica-plate/ fibre-ribbon/ silica-plate sandwich. Two additional

silica plates are glued on the edges of the slit to form a complete casing. An AR coated window is bonded at 2DSH entrance and output facets to avoid straylight and maximize transmission.
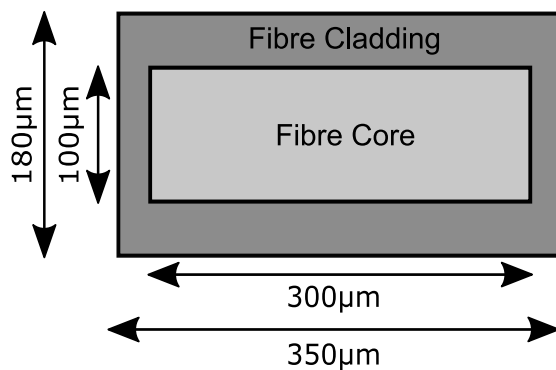
Figure 5.3: Rectangular fibre core geometry.

The separation between the fibre cores due to the cladding results in a stripe pattern at the 2DSH output plane (fig. 5.4). Between the illuminated cores there are dark areas where there is no light. The reason for this is that the light entering the cladding at the 2DSH entrance plane is not propagated through the fibres. Thus, the binning of the spatial samples is already defined in the slit by design. As the NO2I and CO2I share a common 2DSH, this allows for a binning-strategy with almost perfect co-registration between the wavelength channels. However, the cladding gaps also lead to gaps in the imaged swath on-ground and reduced SNR. Note that the gaps are not completely unsampled, as the telescope PSF and scrambler pattern blur the slit projection on-ground.

5.4   Scrambling performance

For the ISRF stability with regard to non-uniform scenes, two scrambling parameters of the fibre have to be considered. First, the ISRF is directly dependent on the slit illumination which, besides some spectrometer magnification, corresponds to the NF after the fibre. Secondly, the ISRF is a function of the spectrograph PSF.
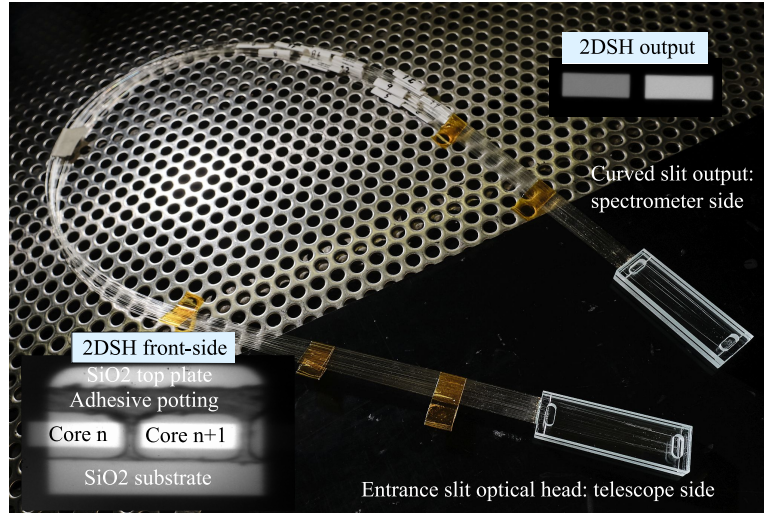
Figure 5.4: 2DSH pre-development model provided by Optec consisting of 25 adjoined rectangular multimode fibres with a length of 100 cm. The fibres within each optical head are bonded on a silica plate. The spectrometer facing output optical head is curved for smile correction (image courtesy of Optec). Adapted from Hummel et al. (2022).

A scene-dependent variation in the FF of the fibre will change the spectrograph pupil illumination and therefore create a scene-sensitive weight of the aberrations present in the spectrograph. This alters the PSF of the spectrometer on the FPA and consequently also the ISRF. The following scrambling gain measurements were performed in the NIR at 780 nm and with a circular $F/3.28$ telescope pupil.

5.4.1 2DSH Near-Field

The light scrambling inside a multimode fibre is achieved by mode to mode coupling between the fibre propagation modes. Yet, the illumination pattern entering the fibre may be partially maintained in the output due to insufficient scrambling. One parameter that determines the scrambling efficiency is the fibre length. Figure 5.5 shows the NF scrambling performance for a short fibre with a length of 5 cm. The input scenes correspond to high contrast scenes with sharp transitions from dark to bright (Type-A scene) and bright to dark (Type-B scene) of the ALT slit illumination. Note that these kind of ALT transitions are impossible to be observed

by a push-broom spectrometer with non-infinitesimal FoV and integration time. Instead, the scene would be smeared out by the satellite motion. However, static scenes are conveniently used in experimental measurements and represent an upper bound for the scene heterogeneity. To the contrary, heterogeneous scenes in ACT are not smeared by the platform motion and may also create distortions in the ISRF stability, particularly in the presence of spectrometer smile (Caron et al., 2017).

Even though the fibre NF output for the short fibre seems visually uniform, the ALT cross section highlights the imperfect homogenization of the scene. The residual position information of the input scene remains as a prominent gradient in the fibre intensity output. This residual gradient impacts both, the ISRF shape and the centroid position. Note that the ripples on top of the gradients are due to measuring with a coherent light source combined with modal noise as a result of the limited excitation of fibre modes guided in the fibre.

The same experiment was repeated for the 100 cm long fibre. Here, the power exchange among the guided modes in the fibre is more efficient and clearly improves the homogeneity of the fibre NF output. As will be quantified in section 5.4.4, only small remnants of the input illumination heterogeneity remain at the fibre output. As depicted in fig. 5.6, there is no visually noticeable difference for the intensity distribution at the fibre output between the case of homogeneous and 50% fibre entrance illumination. Here, the fibre is illuminated with a 50% type-B scene and the corresponding cross section of the NF output is shown. From the comparison of the results for the 5 cm and 100 cm long fibres it can be concluded that the fibre length is a crucial parameter for the scrambling performance and hence a driver for the ISRF stability in the context of non-uniform scenes.

5.4.2 Near field impact on ISRF

To quantify the scrambling performance of the fibre in more detail, the influence of the fibre NF on the ISRF stability merit functions for the 100 cm long fibre is in the

Figure 5.5: Short fibre (5 cm) NF output intensity distribution for scene heterogeneity in ALT direction in the NIR (770 nm). The residual symmetry of the input illumination pattern is partly preserved through the fibre and is still visible as a gradient in the ALT output cross section. Adapted from Hummel et al. (2022).
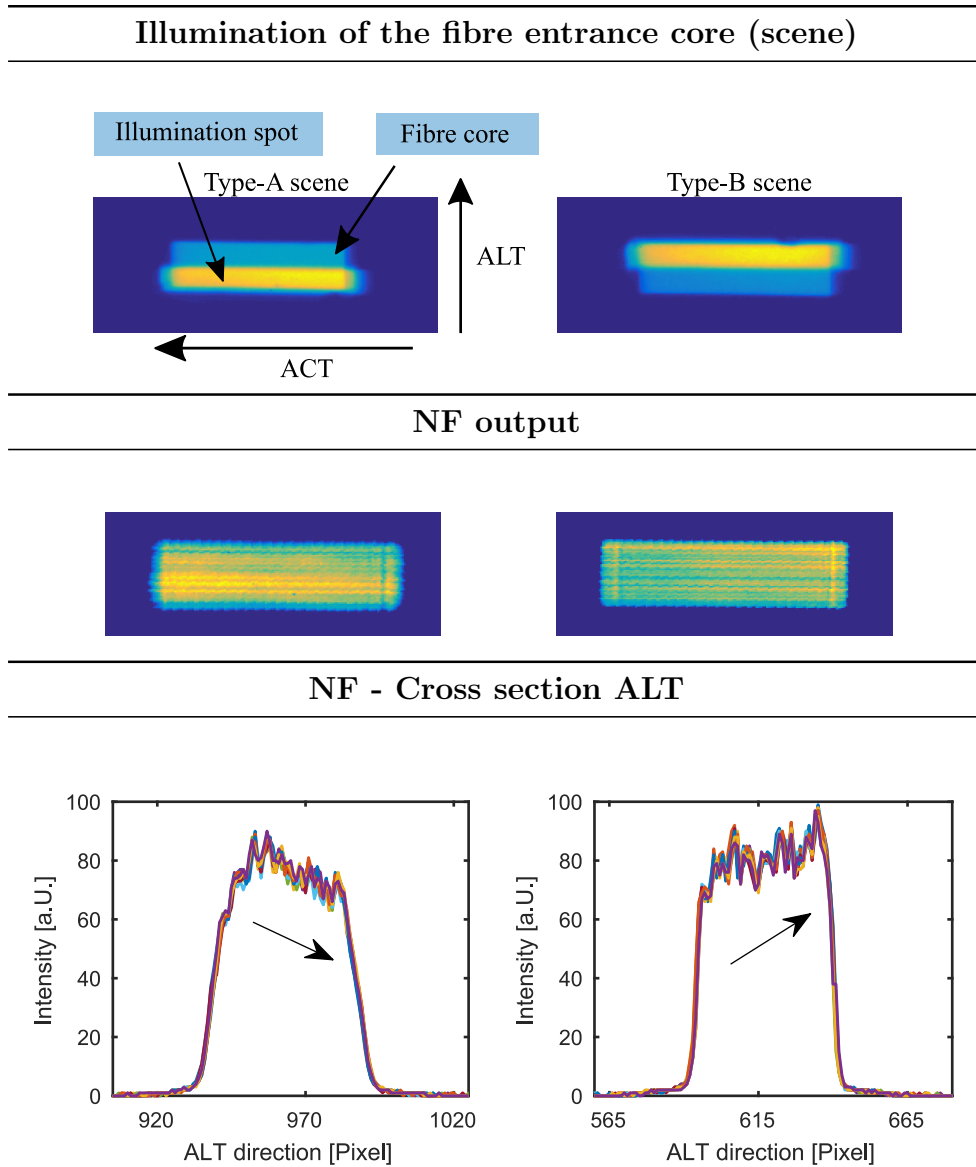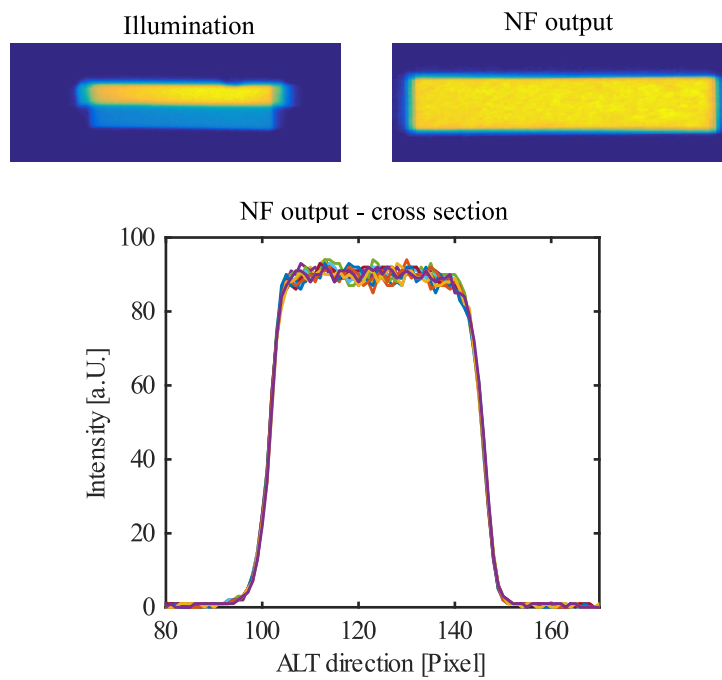
Figure 5.6: Long fibre (100 cm) NF output intensity distribution for scene hetero-geneity in ALT direction in the NIR (770 nm). The 100 cm long fibre yields very high scrambling performance and greatly desensitizes the fibre output from any given input illumination heterogeneity. Adapted from Hummel et al. (2022).

following investigated in the NIR. More precisely, to obtain the ISRF on the FPA, the measured fibre NF output is propagated through the subsequent spectrograph model.

To this end, the ISRF is calculated again as the convolution of the NF intensity after the fibre, a representative spectrograph PSF, and the pixel response of the detector. This routine is comparable to the approach as performed in section 4.3, with the difference that here, the NF image is experimentally acquired. As before, the 2D image of the slit on the FPA is collapsed along the ACT direction by summation, which leaves us with the 1D ISRF in spectral coordinates. The ISRF is then given as:

$$\widetilde{\text{ISRF}}(\lambda) = \text{Slit}(\lambda) \otimes \text{PSF}(\lambda) \otimes \text{Pixel}(\lambda) \tag{5.1}$$

$$\text{ISRF}(\lambda) = \frac{\widetilde{\text{ISRF}}(\lambda)}{\int \widetilde{\text{ISRF}}(\lambda) \, d\lambda} \tag{5.2}$$

where $\otimes$ is the convolution symbol, λ is the wavelength and representing the spectral dimension on the FPA, *Slit* the NF fibre output scaled to the FPA as a function of λ, PSF is the optical point spread function (PSF) of the spectrograph and *Pixel* is the detector response (boxcar). The ISRF intensity is given in arbitrary units. The PSF was generated by raytracing through a representative optical instrument model of the CO2M A/B1 study. To assess the stability of the ISRF, once again the figures of merit for the shape- and centroid-error as defined in eqs. (4.10) and (4.11) are used.

5.4.3   Data reduction and bench stability

A post-processing routine was used for all NF measurements performed in this section. For a typical measurement data point, a set of 20 raw images was acquired. Following the principle of first-order data reduction, corresponding dark images with equivalent exposure times were acquired with the camera shutter closed. After

creating a master dark image by averaging the obtained images, each raw light data image is subtracted by the master dark image. Then a mask of 300 pixels is placed around the barycenter of the nominal light image, corresponding to a homogeneous illumination of the fibre. The barycenter is needed to define a new coordinate system from which to measure deviations in the measurement series with respect to the homogeneous reference.

To verify the stability of the measurements, the mechanical and thermal variations

(a) Bench stability ISRF shape error.

(b) Bench stability ISRF centroid shift.
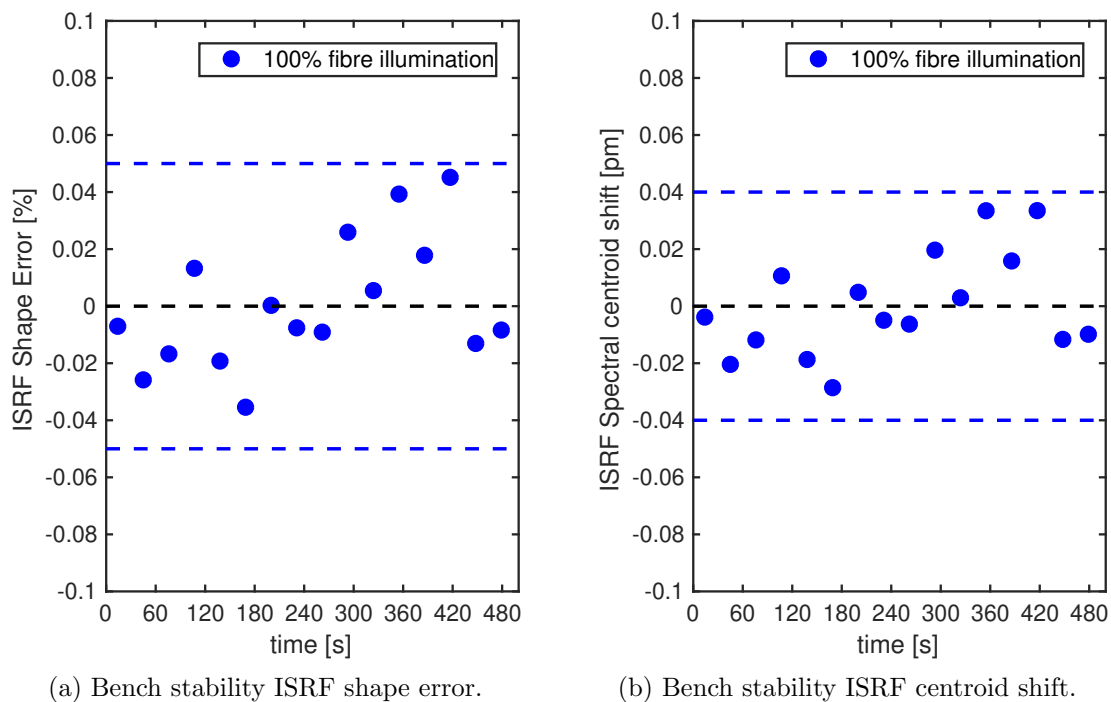
Figure 5.7: Measurement of the bench stability with respect to thermal and mechanical effects over a time period of 8 minutes. For all data points, a homogeneous illumination was injected into the fibre core. (a) shows the evolution of the ISRF shape error with respect to the first data point. (b) shows the evolution of the ISRF spectral centroid shift with respect to the first data point.

of the test bench were characterized. For the measurement, one data point was recorded every 15 seconds over a period of 8 minutes. The period of the measurement corresponds to the duration of a measurement series including some tolerance. For each data point, the change in the figures of merit, i.e. ISRF shape and centroid was calculated with respect to the first data point. For each data point, the fibre was

homogeneously illuminated and no changes were made to the test bench. Figure 5.7a
shows the result of the evolution of the ISRF shape error over a period of 8 minutes
and Figure 5.7b the corresponding ISRF spectral centroid shift. The respective
errors are always below $< 0.05\%$ shape error and <0.04 pm spectral centroid shift.
The bench limitations are small compared to the stability requirements of the ISRF
and the errors are assumed to be maximum errors in the following considerations.

5.4.4   Near-Field ISRF results

The ISRF figures of merit are calculatd for several type-A and type-B scenes, where
the fraction of the fibre illumination area is step-wise decreased, ranging from 100%
to 20%. Figure 5.8a shows the evolution of the ISRF shape and centroid error for
partial fibre illuminations relative to a full illumination which corresponds to a
homogeneous scene. The centroid shift on the FPA is given in spectral dimension,
i.e. representing the spectral shift of the ISRF centroid. Even for the extreme case
of only 20% fibre illumination with a sharp contrast, the fibre homogenizes the
contrast with high efficiency, leading to a maximum absolute ISRF shape error of
0.461%. This is well below the CO2M requirement of 1.5% shape error. One can
also observe very low sensitivity with regard to the input scene for the stability of
the centroid error. The maximum spectral centroid shift on the FPA for a 20%
partial fibre illumination is <0.25 pm, which easily satisfies the requirement of
2 pm. The residual centroid shift is dependent on the symmetry of the applied
input illumination. The centroid shift in opposite direction when the partial fibre
illumination is at the bottom (type-A scene) or top (type-B scene) of the fibre.
This is confirmed when comparing the shape difference between an ISRF for a
homogeneous scene and a heterogeneous scene of 20% fibre illumination as depicted
in fig. 5.8b. The shape difference inversion of the ISRF follows the inversion of
the ALT illumination symmetry of either bottom (left plot) or top (right plot)
illumination of the fibre entrance. These results indicate the extremely enhanced
scrambling capabilities of fibre-based SH. By using a 2DSH, almost any scene
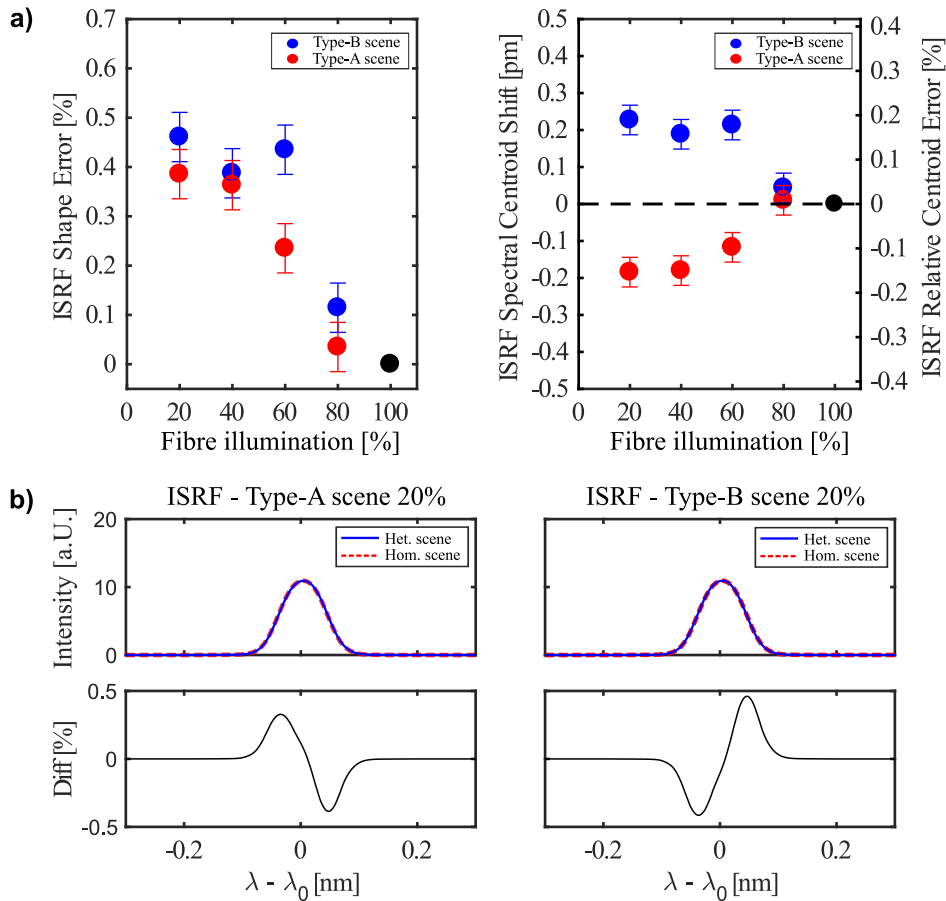
Figure 5.8: (a) ISRF shape and centroid error in the NIR for several high-contrast scenes for the 100 cm fibre. Red and blue data points correspond to fibre partial illumination fraction, moving from bottom-top and top-bottom, respectively. The reference for the relative error is the homogeneous illumination of the fibre entrance. (b) Shape difference between an ISRF of 20% fibre illumination starting at bottom (type-A scene) and top (type-B scene) respectively, and a homogeneous fibre illumination. The symmetry of the input illumination is still visible as asymmetric shape behaviours in the ISRF. Adapted from Hummel et al. (2022).

dependency of the slit illumination is eliminated. It shall also be noted that the performance is also particularly superior to the NF scrambling capabilities of the 1DSH as quantified in section 4.3. For a 50% CAL scene in the NIR, a classical slit would yield a ISRF shape error of 60.5%, compard to 8.685% for a 1DSH as implemented in Sentinel-5/UVNS and to $< 0.4\%$ (interpolated from fig. 5.8a) for a 100 cm long fibre-based 2DSH.

Besides the unprecedented NF homogenization, similar to the 1DSH, also the 2DSH modifies the spectrograph pupil intensity distribution as described in the next part.

5.4.5   2DSH Far-Field

The heritage of radial velocity (RV) measurements of ground-based telescopes indicate that the FF after the fibre depends on the input illumination of the fibre. Contrary to classical slits, this means that the telescope pupil intensity distribution is not preserved in the spectrograph pupil when using a fibre-based slit under the condition of non-uniform fibre illumination (Halverson et al., 2015; Feger et al., 2012). Figure 5.9 depicts the FF intensity distribution obtained with a 5 cm and 100 cm fibre. All measurements in this section were done with a circular $F/3.28$ telescope pupil and the FF was imaged at a distance of 6 cm from the fibre exit. Different input illumination symmetries were applied, in which a small illuminated rectangle was moved through the fibre input core in ACT direction. It was observed that for both fibre lengths, the FF intensity patterns have symmetric shapes with either a dip or a peak in the centre. The intensity profiles become flat when placing the illumination rectangle in the fibre centre. These findings have also been reported by other studies in the context of RV ground-based spectrographs (Halverson et al., 2015; Feger et al., 2012; Avila, 2012). In the presented study, this effect has been observed in both, the NIR (780 nm) and SWIR (1550 nm) wavelength. The amplitude of the peak/dip asymmetry is significantly stronger for the short fibres. This confirms the assumption that the mode-to-mode coupling increases with fibre length. The limited mode excitation due to the small excitation

Fibre input illumination	Short fibre (5 cm)	Long fibre (100 cm)
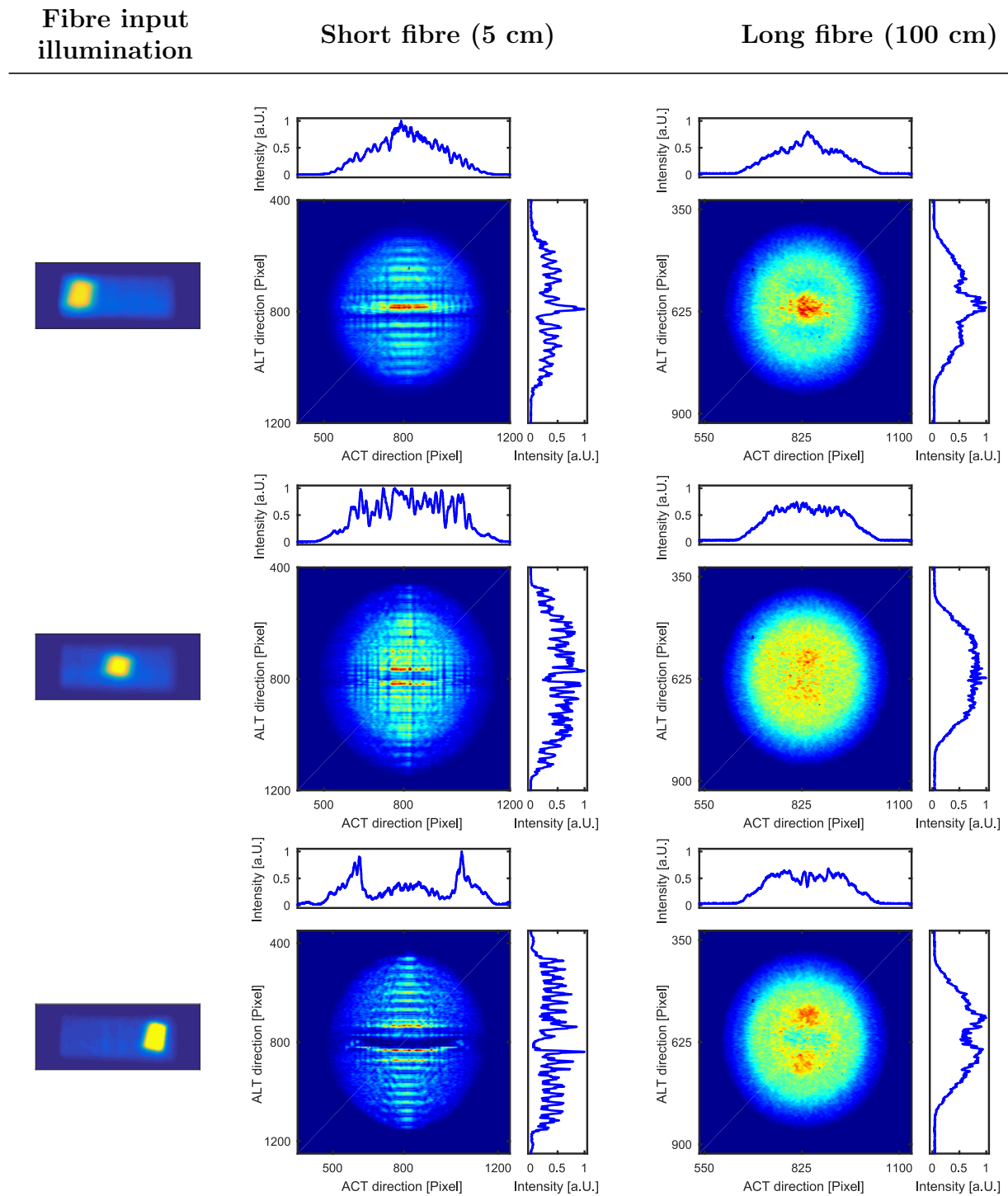
Figure 5.9: Fibre FF intensity distribution obtained in the NIR (770 nm) for a short- (5 cm) and long (100 cm) fibre for different input illumination symmetries. The FF intensity patterns have symmetric shapes with either a peak or a dip in the centre, depending on the location of the fibre input. Partial but symmetric fibre input illumination results in a flat but noisy FF due to limited modes (modal noise). The amount of mode-to-mode coupling as a function of fibre length is clearly visible in the FF patterns of the two tested fibres. Adapted from Hummel et al. (2022).

area at the fibre input core is compensated by small random variations of the optical and geometrical properties of the fibre. The root cause for these perturbations could be microscopic random bends or refraction fluctuations which are generated during the fibre manufacturing process. Due to the longer interaction length, the mode coupling mechanisms are stronger for longer fibres and therefore support the homogeneity of both, the NF- and, more prominently, the FF intensity distribution (Spronck et al., 2012).

5.4.6 Far-Field impact on ISRF

The impact of a non-uniform spectrograph pupil illumination on the ISRF stability is mainly driven by the scene-dependent weighting of the aberrations present in the spectrograph optics. Consequently, this results in a scene dependent optical PSF, which serves as a kernel for the ISRF, and therefore adds another error contribution to the ISRF. Note that this effect is independent of the NF error contribution and puts additional uncertainty to the ISRF knowledge. In order to quantify the FF impact on the ISRF for the CO2M model of Phase A/B1, a slightly different approach was followed than for the NF. The dip and peak FF intensity maps of long and short fibres as given in fig. 5.9 (first and third row, respectively) were propagated through the Airbus CodeV model to simulate the optical PSF. The ISRFs using these PSFs are compared to those for a homogeneous spectrograph pupil intensity distribution with respect to shape and centroid changes. This was done for three spatial field points and three spectral points on the FPA grid in each wavelength channel (NIR, SWIR-1, SWIR-2). In this way, an attempt was made to account for the fact that different areas of the detectors have different aberrations. This 3x3 grid covers the center and edge parts of each respective spectral band detector. For the analysis, only the FF effects were quantified and a homogeneous NF output of the fibre was assumed. Therefore, the outcome of the analysis corresponds only to ISRF errors due to PSF variation accounting for optical aberration and the spectrograph pupil intensity distribution. The results
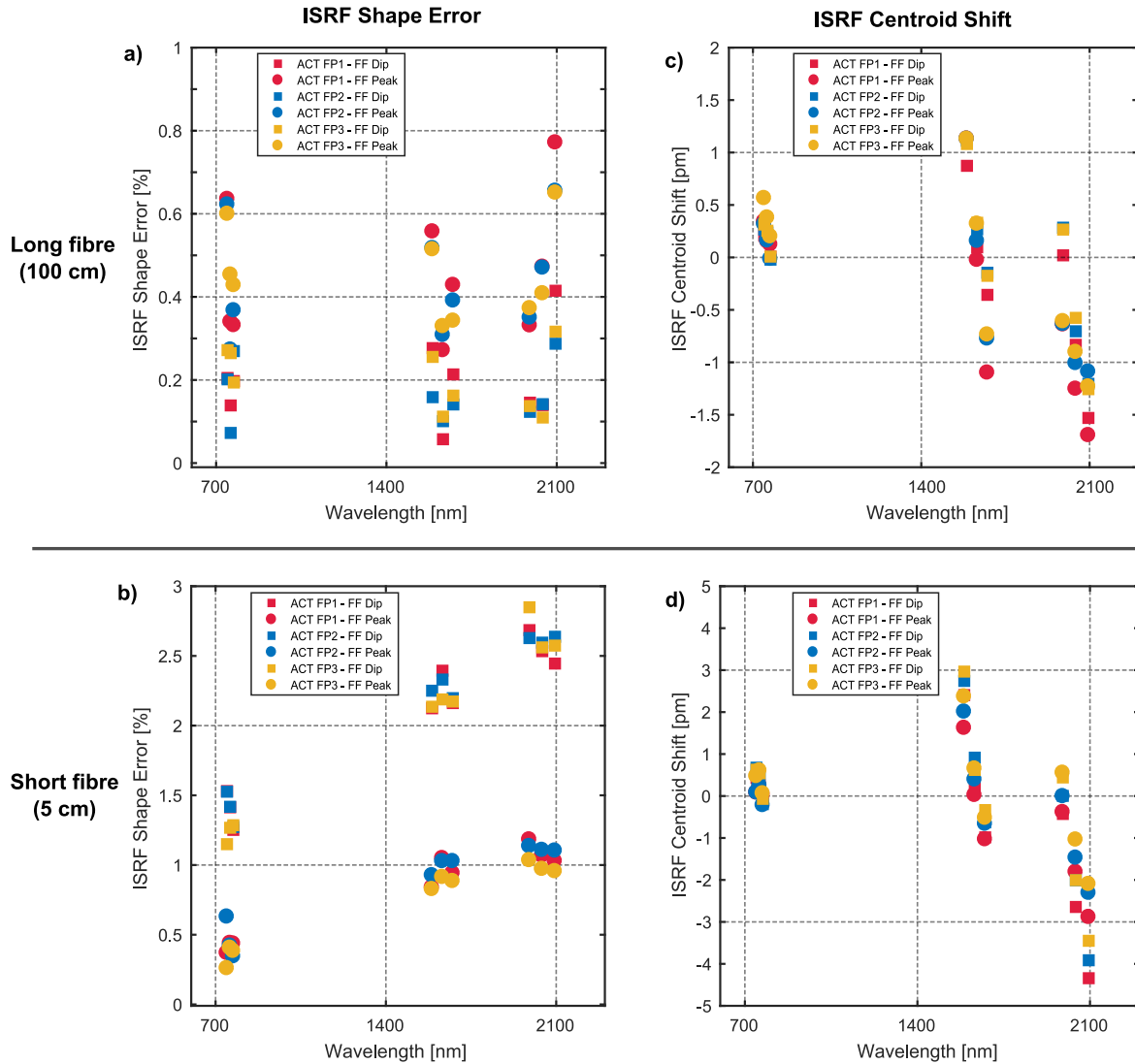
Figure 5.10: Impact of the modified spectrograph pupil illumination (FF) on the ISRF merit functions. The presented errors compare the difference of the ISRF shape and centroid for a homogeneous FF to the measured long and short fibres FFs, with either a dip (squares) or a peak (circles) in the center. The FF intensity maps serve as an input of the Airbus CodeV model for three spatial field points (ACT) and three spectral samples in each spectral channel (NIR, SWIR-1, SWIR-2). The three ACT and wavelength field points are positioned at the edges and center of the FPA of the respective wavelength band. FP1 corresponds to a left edge-, FP2 to a center- and FP3 to a right-edge field point of the FPA. (a) Depicts the ISRF shape error for the long fibre, (b) the ISRF shape error for the short fibre, (c) the ISRF centroid shift for the long fibre and (d) the ISRF centroid shift for the short fibre. Adapted from Hummel et al. (2022).

for the figures of merit are shown in fig. 5.10. The more distorted FF with respect to the intensity peak-to-valley amplitude variation of the short fibre directly leads to larger errors in the ISRF compared to the long fibre. The maximum ISRF shape error for the short fibre is 2.8% (see fig. 5.10b) compared to 0.78% (fig. 5.10a) for the long fibre. The result for the short fibre exceeds the ISRF shape requirement by almost a factor of 2. Relative to the requirements, the centroid shift for the short fibre is mainly affected in the SWIR-1 channel. It has a spectral shift of 2.95 pm which corresponds to 59% of the global centroid stability budget. The long fibre has the largest error contributor in the NIR with 28% of the overall budget corresponding to a centroid shift of 0.56 pm. Note that the associated shape and centroid errors are only caused by the FF variations and neglect heterogeneity in the NF. The NF errors, as characterized (for the long fibre) in section 5.4.4, do contribute to the total error in addition to the FF errors.

In general, the impact of the spectrograph pupil intensity is directly linked to the
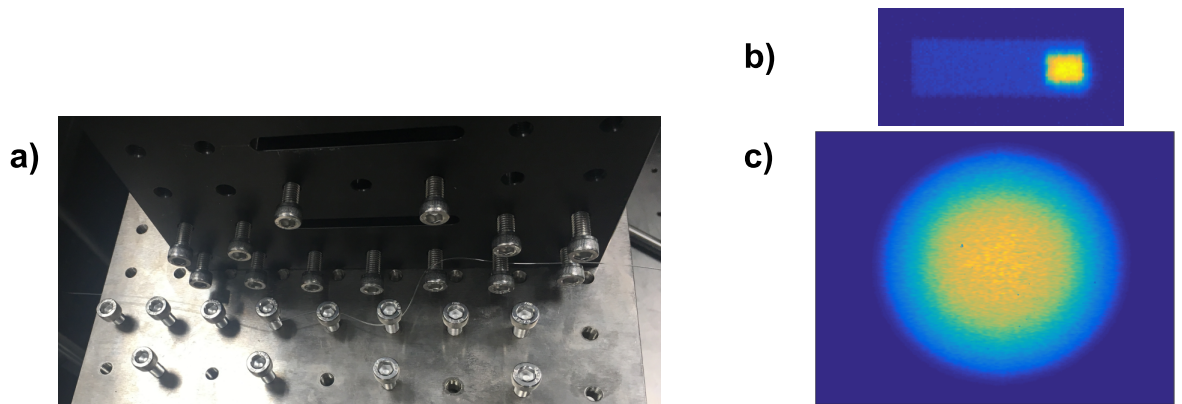
Figure 5.11: (a) Fibre bending scheme. The fibre is arranged in a sinusoidal shape with bending applied in the vertical and horizontal plane. (a) Fibre input illumination and (c) the corresponding fibre output FF intensity distribution after applying fibre bending. Measurements are shown as examples in the NIR, but were verified by measurements in the SWIR. Adapted from Hummel et al. (2022).

aberrations in the specific instrument. Therefore, it is not possible to generally quantify the impact on the ISRF. However, our results suggest that shorter fibres cause larger FF variations than longer fibres, resulting in a significant increase in

ISRF errors. Since the FF errors of the long fibre also account for 50% of the total ISRF shape error budget, a way to homogenize the FF was explored. To do so, a technique to induce appropriate mechanical stress on the fibre was investigated. This is done by applying small bending radii of the fibre in a sinusoidal shape and thereby stimulate the mode-to-mode coupling of the light propagating in the fibre. The initially finite number of traversing modes within the multi-mode fibre get rearranged into a more evenly distributed population of the possible propagation modes (see fig. 5.11a). The result is a stronger decorrelation of the fibre output, in particular of the FF, from fibre input illuminations. Figure 5.11b shows the fibre input illumination and fig. 5.11c the resulting FF intensity distribution for the 100 cm fibre. Compared to the previously observed strong variations, the FF is homogeneous and therefore independent of the fibre input. Hence, the spectrograph pupil illumination is stable also for heterogeneous scenes and does not affect the ISRF stability. The remaining ISRF errors after propagation by the aberration model are found to be negligible.

In conclusion, a sufficiently long fibre for a 2DSH is a necessary condition for efficiently homogenizing the fibre NF and FF output.

5.5   Focal ratio degradation

Another important property of a fibre is the conservation of system F# as it is, depending on the sizing of the collimator optics, a significant contributor to the optical transmission through the instrument and hence to the system's SNR. The so-called *focal ratio degradation* (FRD) is an unavoidable effect in optical multimode fibres and describes the change between the input and output F# of the light cone entering the fibres. The schematic principle is depicted in fig. 5.12. The causes for this effect have not yet been fully understood; candidates are imperfections of the fibre material, quality of the fibre end facet, microscopic deformations of the core shape, stress inside the fibre as well as micro- and macro bending of the fibre (Avila, 2012; G, 1998; Crause et al., 2008). All these effects eventually trigger physical

processes such as scattering, diffraction and modal diffusion of the light, which alter the output cone of the light exiting the fibre (Haynes et al., 2011). FRD has been extensively studied in on-ground spectrograph fibre links. The amplitude of the F# degradation depends on the working F# of the light input cone into the fibre. In general, faster F# are reported to show better FRD performance (Sutherland et al., 2016; Avila, 2012).   The FRD losses were tested for a circular $F/3.28$
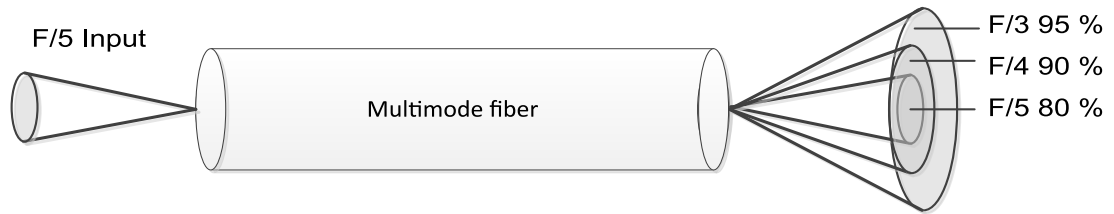

Figure 5.12:   Focal ratio degradation (FRD) effect in optical multimode fibres. The input F# gets degraded by scattering effects inside the fibre. Adapted from Hummel et al. (2022).

telescope pupil. In the Airbus CO2M A/B1 instrument design, the telescope pupil is oversized and the radiometric stop of the system is located on the spectrograph pupil plane. Therefore, to assess the impact of the FRD on the radiometry, we have to compare the flux collected by the spectrograph pupil without and with FRD. The ratio between these two fluxes is defined as the FRD loss in this paper. Figure 5.13 shows a typical FF illumination after the fibre for a homogeneous input scene with a $F/3.28$ telescope. The blue circle depicts the telescope pupil projected on the FF image without FRD. The red circle corresponds to $F/2.28$ and is used for an overall flux summation exiting the fibre ($F_{sum}\#$); it accounts for all possible FRD effects. The black rectangular shape with cut corners is the baseline for the spectrometer pupil aperture in our model. The FRD is computed as follows: the intensities of all pixels inside a $F/2.28$ cone (red circle in fig. 5.13) are summed up, which gives the total signal collected in the FF. By summing a larger area than the actual spectrograph pupil, any FRD effects can be included and all photons are counted. Without any FRD effects, the total intensity would be uniformly spread within the telescope pupil (blue circle). This homogeneous illumination
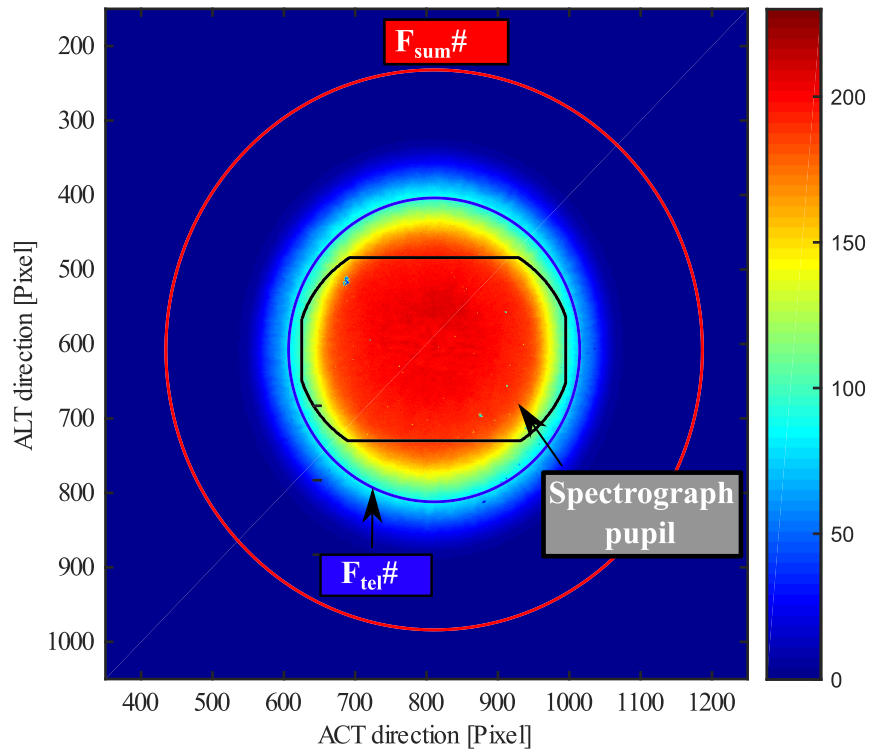
Figure 5.13:   Typical fibre output in the FF for a homogeneous input in the NIR with a circular $F/3.28$ telescope pupil. The black rectangle with rounded corners indicates the spectrograph pupil baseline of our model The blue circle is the telescope pupil corresponding to $F/3.28$ ($F_{tel}\#$). The larger red circle ($F_{sum}\#$) is the summation area to take possible FRD broadening into account ($F/2.28$). Adapted from Hummel et al. (2022).

would then be cut out by the spectrograph pupil (black shape) and represents the case of a classical slit. The FRD losses are quantified as the ratio between the pixel intensities in the black area assuming a homogeneous intensity distribution in the FF and the measured distribution.

The FRD losses were determined for the above described approach in the NIR and SWIR-1 wavelength band. Mechanical stress also is known to increase the magnitude of FRD losses. Therefore, different stress cases on the 100 cm fibre were tested. It was found that the major FRD contribution was generated by the used mount of the fibre front and end facet. The test scenarios included fibres attached with mechanical clamping mounts, a bent configuration for the FF homogeneity stability and fibres glued on a glass substrate (2DSH-bundle, two separate fibre-cores tested). FRD losses in the range of 2.1% to 8.8% were

Fibre configuration	NIR [780nm]	SWIR-1 [1550nm]
Straight fibre	$6.0\% \pm 1.0\%$	$8.8\% \pm 0.19\%$
Bent fibre	$6.75\% \pm 0.14\%$	$8.0\% \pm 1.40\%$
2DSH-bundle core 1	$2.05\% \pm 0.88\%$	-
2DSH-bundle core 2	$2.10\% \pm 1.24\%$	-

Table 5.2: Radiometric losses due to FRD for a 100 cm long fibre in several mount and stress conditions.

measured. The glued fibres of the 2DSH-bundle had the best FRD performance. Besides the gentle mounting, another reason for the superior performance could be the separate polishing and termination processes, which might have been more thorough in the 2DSH bundle pre-development. Both possibilities are in line with the findings by Allington-Smith et al. (2013), where the authors associate the primary generation of FRD to the fibre-ends configuration. They conclude, that minimized physical perturbations of the fibre-end improve the FRD performance. According to our measurements, applied stress by bending in the middle parts of the fibre link seems to have limited impact on the FRD and therefore seems

feasible in terms of radiometric losses. Despite several efforts to characterize FRD dependency on wavelength in theoretical models as well as in experiments, the issue remains open as several findings are inconsistent. A theoretical modal diffusion model by Gloge (1972) predicts FRD increasing with longer wavelength, which was confirmed by experimental studies from Carrasco and Parry (1994) and Poppett and Allington-Smith (2007). Other studies conducted by Murphy et al. (2008), Schmoll et al. (2003) and Crause et al. (2008) found no measurable wavelength dependency. Note that all of those studies were performed at UV-Vis and NIR wavelength regimes. In the presented measurements no convincing evidence for wavelength dependency between FRD in the NIR (780 nm) and SWIR-1 (1550 nm) wavelength channel was found. Table 5.2 summarizes the FRD results. It shall be stressed that they are linked to the spectrograph pupil stop shape of our model and the F# of the system.

In this study, the effect of the fibre length on FRD losses was not investigated. While theoretical prediction models again suggest an increase of FRD losses with fibre length (Gloge, 1972), several experimental studies have disproved this. Avila et al. (2006) and Poppett and Allington-Smith (2010) found no evidence for increasing FRD of longer fibres and conclude that within the experimental uncertainty, no length dependence is observed. If there is a dependency, it is a small one, which is especially the case for relatively short fibres as proposed for a 2DSH in spaceborne imaging spectrometers.

5.6 Conclusion

The preceding chapter presents an efficient fibre-based 2D-Slit homogenizer for high-precision spaceborne imaging spectrometers and continues the studies of Amann et al. (2019) and Guldimann and Minoglou (2016). Entrance slits based on waveguides were shown to be an effective design solution for the prospective European CO2M mission, meeting its demanding co-registration requirements as well as ISRF stability under extreme spatial variations in the Earth scene radiances. The present

work suggests that the fibre length is a crucial parameter for the power exchange among guided modes and therefore for the fibre homogenization efficiency. The short fibre of 5 cm length preserves the contrast of the input illumination pattern injected into the fibre-entrance as a prominent gradient in the output intensity distribution. The slope of the gradient is directly correlated to the position of the input illumination of the fibre. In contrast, the long fibre shows strongly enhanced scrambling performance. The mode coupling mechanisms evolve stronger for longer fibres and therefore increase the homogeneity after the fibre. Under the extreme case of 20% partial fibre illumination, the maximum uncertainty for the long fibre in the ISRF shape is $< 0.5\%$. For the centroid position we measured a maximum spectral shift of < 0.25 pm (NIR).

Contrary to classical slits, a fibre-fed slit induces scene-dependent spectrograph pupil illuminations. Together with geometrical optical aberrations present in the spectrograph, this leads to another source of ISRF instability, besides the slit illumination. Depending on the strength and type of aberrations, the error can significantly contribute to the global ISRF stability budget. For the aberrations present in the spectrometer design, the ISRF shape errors induced by the modified spectrograph pupil intensity distribution are quantified as 2.8% for the short fibre and 0.77% for the long fibre (CO2M requirement: 1.5%). The centroid error for the short fibre corresponds to 59% of the overall error budget (2.95 pm shift in SWIR-1, CO2M requirement: 5 pm) and 28% for the long fibre (0.56 pm shift in NIR, CO2M requirement: 2 pm). These results again highlight the poorer scrambling performance of the short fibre. In the presented specific instrument design, the short fibre does not provide the required performance to meet the system requirements. Since also the long fibre FF distortions create significant ISRF errors, accounting for almost half of the global error budget, a solution was proposed to recover the FF uniformity by inducing appropriate stress through bending of the fibre. By doing so, the traversing modes within the fibre get rearranged into a more evenly distributed population of the propagation modes, resulting in a homogenized NF and FF.

Even though the 2DSH has unprecedented homogenizing capabilities, a drawback is that the $F\#$ exiting the fibre is decreased compared to the initially injected telescope $F\#$. The transmission loss caused by this effect affects the radiometric performance in terms of SNR, but may also be compensated by appropriate sizing of the spectrometer optics. The transmission losses for the given model of the CO2M phase A/B1 study were quantified ranging from $2\% - 9\%$. A strong dependence of FRD losses on the fibre end-facet mounting scheme was observed. Gently gluing the fibre onto a glass-substrate using special adhesives and thorough fibre polishing minimizes the stress on the fibre and yields the best performance. The bending of the fibre in order to homogenize the FF seems to have limited impact on the FRD losses and therefore seems appropriate.

The presented results indicate that under extreme heterogeneity in the Earth scene radiances the 2DSH scrambling performance is superior compared to previous slit designs. In light of its other advantages, such as nearly perfect co-registration due to the cladding induced blind gaps between adjacent spatial samples, it is concluded that the presented slit design offers an adequate solution for future space-based imaging spectrometers to solve the issues caused by heterogeneous Earth scenes on the instrument spectral accuracy.

6 ISRF impact on DOAS Retrieval

In the previous chapters, the spectral stabilization capabilities of two SH techniques have been quantified in terms of several figures of merit of the ISRF. So far, the ISRF stability parameters have been the only measure used to quantify the impact of heterogeneous scenes. In this chapter, the resulting ISRF errors are translated into the respective retrieval accuracy of the NO_2 column density using simulated Sentinel-5/UVNS scenes as an example. In this context, the effect of 1DSH on the retrieval in the instrument UV-VIS channel is evaluated for two heterogeneous Earth scenes. Once the retrieval is performed with an instrument equipped with a SH and once with a classical slit. The retrieval algorithm is performed using Differential Optical Absorption Spectroscopy (DOAS), a method for determining the concentration and total amount of atmospheric trace gases from remote sensing instruments. This method is explained in section 6.1 and followed by an introduction to the Radiative Transfer Model (RTM) and the MYSTIC solver for the Radiative Transfer Equation (RTE) in section 6.2. This solver was used to calculate a 3D heterogeneous Earth radiance scene in the UV-VIS channel. In section 6.4, the arriving radiance spectrum at the Sentinel-5/UVNS instrument is propagated through the instrument up to FPA level. In the final section 6.5, the total column density of NO_2 is retrieved over several heterogeneous scenes for an instrument with a 1DSH and an instrument with a classical slit. Then, both cases are compared to the case of a perfectly symmetric ISRF that neglects any instrument imperfections with respect to heterogeneous scenes.

6.1 Differential Optical Absorption Spectroscopy

In this section, the main concepts of the Differential Optical Absorption Spectroscopy (DOAS) retrieval method are introduced. This technique will be used to evaluate the impact of heterogeneous scenes and the associated ISRF distortions on the retrieval accuracy of the slant column density (SCD) determination of NO_2 from an artificial Earth scene. The content of this section is primarily based on

the book of Stutz and Platt (2008) on the principles and applications of DOAS retrieval.

The DOAS method is used to determine the concentrations and total columns of atmospheric components in the UV, VIS and NIR wavelength bands. In the SWIR, the DOAS method has difficulty to account for the idiosyncrasies of the strong absorption features, and therefore usually either modifications are made to the DOAS method or other retrieval techniques are used (Frankenberg et al., 2005). The foundation of DOAS is the absorption of light by trace gas constituents in the atmospheric layers, following the *Lambert Beer's law* of absorption, which can be written as:

$$I\left(\lambda\right) = I_0 \ exp\left(-\sigma\left(\lambda, T\right) \cdot \int c\left(L\right) \cdot dL\right) \tag{6.1}$$

where $I\left(\lambda\right)$ is the intensity of a light path after passing through the atmosphere of thickness L, $I_0\left(\lambda\right)$ the initial intensity of the light and $c\left(L\right)$ the concentration of the absorber in units molecules per volume and $\sigma\left(\lambda, T\right)$ defines the absorption cross section of the species of interest at the wavelength λ and temperature T. The temperature dependence of $\sigma\left(\lambda, T\right)$ is usually dealt with by using the number density maximum of the climatological profile of the corresponding trace gases or by applying temperature corrections (Wenig et al., 2005; Burrows et al., 1999) and will be neglected for simplicity in the following. The absorption cross section of a trace gas is its ability to absorb incoming photons and is a characteristic property. The cross section is derived from laboratory measurements for each respective trace gas. Applying the natural logarithm at both sides of eq. (6.1) yields for the concentration:

$$\int c\left(L\right) dL = \frac{ln\left(\frac{I_0\left(\lambda\right)}{I\left(\lambda\right)}\right)}{\sigma\left(\lambda\right)} = \frac{D}{\sigma\left(\lambda\right)\cdot} \tag{6.2}$$

where the expression

$$D = ln\left(\frac{I_0\left(\lambda\right)}{I\left(\lambda\right)}\right) \tag{6.3}$$

is referred to as the optical density. The concentration c of a trace gas along the

light path L is often given as SCD, defined as:

$$SCD = \int c\left(L\right)\,dL \tag{6.4}$$

For atmospheric measurements based on satellite remote sensing, in particular, the initial intensity I_0 of light and the specific contribution of Mie- and Rayleigh scattering is unknown, which makes the solution of eq. (6.2) impossible at first sight. At this point, the innovative approach of differential spectroscopy is applied, which will make use of changes in the absorption at different wavelengths. In order to remove the dependence of the initial intensity I_0 when measuring the concentration c, the idea is to exploit that light at different wavelengths encounters different absorption strengths.

To do so, we first expand the Lambert-Beer's law by other contributing light interaction parameters besides absorption such as Rayleigh and Mie extinction as well as instrumental parameters. Furthermore, we will include multiple absorbers in the atmosphere which is a more realistic scenario. Then eq. (6.1) transforms to:

$$I\left(\lambda\right) = I_0\left(\lambda\right)\,exp\left[\int_0^L \left(\sum_i \left(-\sigma_i\left(\lambda\right)\cdot c_i\left(L\right)\right) - \epsilon_R\left(\lambda, L\right) - \epsilon_M\left(\lambda, L\right)\right)dL\right]\cdot A\left(\lambda\right)$$
$$\tag{6.5}$$

where $\epsilon_R\left(\lambda, L\right)$ is the Rayleigh extinction coefficient, $\epsilon_M\left(\lambda, L\right)$ is the Mie extinction coefficient, which are both dependent on the specific position in the atmosphere, and $A\left(\lambda\right)$ summarizes all instrument effects. The index i defines the number of species. The DOAS method will make use of the fact that Rayleigh- and Mie scattering as well as instrument effects show very smooth spectral characteristics. To the contrary, the absorption cross section of certain trace gases have very distinct narrow-band spectral structures. It is thus possible to separate slow and fast varying spectral structures as:

$$\sigma_i\left(\lambda\right) = \sigma_{i0}\left(\lambda\right) + \sigma_i'\left(\lambda\right) \tag{6.6}$$

where $\sigma_{i0}(\lambda)$ denotes the part which varies slowly with wavelength and $\sigma_i'(\lambda)$ the fast varying part. This separation is the central trick of the DOAS method, which therefore restricts the application to trace gases with narrow band structures (typical widths of the absorption structures are $<10\,\text{nm}$).

Inserting eq. (6.6) into eq. (6.5) gives:

$$
\begin{aligned}
I(\lambda) =& I_0(\lambda) \cdot exp\left[\int_0^L \left(\sum_i \left(-\sigma_i'(\lambda) \cdot c_i(L)\right)\right) dL\right] \\
&\cdot exp\left[\int_0^L \left(\sum_i \left(-\sigma_{i0}(\lambda) \cdot c_i(L)\right) - \epsilon_R(\lambda, L) - \epsilon_M(\lambda, L)\right) dL\right] \cdot A(\lambda)
\end{aligned}
$$
(6.7)

where the first exponential function contains all the fast absorbing interactions of the light with the trace gas and the second exponential function combines the slow varying absorption features. In a next step, the intensity in absence of differential absorption is defined as:

$$
I_0'(\lambda) = I_0(\lambda) \cdot exp\left[-L\left(\sum_i \left(\sigma_{i0}(\lambda) \cdot c_i\right) - \epsilon_R(\lambda, L) - \epsilon_M(\lambda, L)\right)\right] \cdot A(\lambda) \quad (6.8)
$$

Substituting $\sigma_i'(\lambda)$ for $\sigma_i(\lambda)$ in eq. (6.2) and considering that $\sigma_i'(\lambda)$ and $\sigma_i(\lambda)$ are universal properties of the corresponding species and can be determined in laboratory experiments, the differential optical density can be defined by analogy with eq. (6.3) as follows:

$$
D' = ln\frac{I_0'(\lambda)}{I(\lambda)} = \int_0^L \sum_i \sigma_i'(\lambda) \cdot c_i \, dL
$$
(6.9)

This section summarized the basic principle of the DOAS method.

6.2 Radiative Transfer Modelling of inhomogeneous scenes

To determine the performance of 1DSH in terms of retrieval accuracy, an artificial heterogeneous earth scene is generated. This section describes the basic theory of *radiative transfer modelling (RTM)* used to simulate the propagation of the photon

path through the atmosphere and to derive the spectrum entering the instruments onboard the satellite. During the path through the atmosphere, the radiation is affected by several phenomena, such as scattering and absorption by molecules, aerosol particles as well as cloud droplets and particles. The formulation of the interaction between radiation and matter in the atmosphere was first formulated by Chandrasekhar (1960) and is given by the *radiative transfer equation (RTE)*:

$$\underbrace{\frac{dL}{ds}}_{(1)} = \underbrace{-\beta_{ext}\,L}_{(2)} + \underbrace{\frac{\beta_{sca}}{4\pi}\int_{4\pi} p\left(\Omega',\Omega\right)L\left(\Omega'\right)\,d\Omega'}_{(3)} + \underbrace{\beta_{abs}\,B_{Planck}\left(T\right)}_{(4)} \qquad (6.10)$$

here, (1) describes the change of radiance L over the light path s. The other side of the equation summarizes all considered effects, which alter the photon path. (2) denotes the fraction of radiance that is vanished out of the direction of the beam and is determined by the extinction coefficient β_{ext}, which in turn is given as the sum of the absorption β_{abs} and scattering coefficient β_{sca}. (3) accounts for photons that are scattered into the direction of the beam, which is given by the scattering phase function $p\left(\Omega',\Omega\right)$. The scattering phase function calculates the probability of a photon approaching from direction $\Omega' = (\theta', \phi')$ being scattered into the direction of the beam $\Omega = (\theta, \phi)$, where θ is the polar angle and ϕ the azimuth angle. The resulting photon added to the beam is given by the radiance $L\left(\Omega'\right)$. This formulation of the RTE does not include inelastic scattering. Finally, (4) provides added photons into the beam direction, which are thermally emitted by a blackbody with temperature T. With eq. (6.10), it is theoretically possible to calculate radiance as a function of location and direction at any arbitrary point in the atmosphere. However, the equation is an integro-differential equation, and solving the RTE is a challenging task. In fact, there is no analytical solution even for the simplest scattering problems.

One possible solution to treat the RTE is to use the Monte Carlo technique. This approach is part of the *libRadtran* software package (Emde et al., 2016), which will be used in this thesis to simulate a heterogeneous albedo Earth scene. In this

RTE solver, individual photons are tracked through the atmosphere by calculating their random paths and accounting for scattering and absorption events from the time they enter the atmosphere to the time they enter the observing instrument. As we consider heterogeneous Earth scenes induced by albedo variations on the ground, we have to treat this problem as a 3D radiative transfer problem. One of the most comprehensive tools to simulate such problems is the Monte Carlo code *MYSTIC*. In the following, the basic principles of MYSTIC are introduced. For a detailed description, the reader is referred to Mayer (2009, 1999); Emde et al. (2011).

Monte Carlo solver MYSTIC

The source of photons considered for remote sensing applications in the solar band is the sun. Therefore, the aim of the Monte Carlo method is to determine the path of each photon through the atmosphere. The photon's path can end either when it is absorbed by an atmospheric constituent, when it is absorbed by the surface, or when the photon leaves the atmosphere at the top, which is called top of atmosphere (TOA). After an initial position and direction of the photon is determined, the travel of the photon is performed taking into account all effects. The probability for survival of a photon along the path is given by the Lambert-Beer's law according to:

$$p_{sur}(\tau) = exp(-\tau) \tag{6.11}$$

where the optical thickness τ is the integral of the volume extinction coefficient along the photon path s:

$$\tau = \int_0^s \beta_{ext}(s') \ ds' \tag{6.12}$$

Here, β_{ext} is again the extinction coefficient. At the same time, it can be shown that the probability for photon extinction is equivalent to the probability for the photon to survive by considering the probability that the photon becomes extinct

between τ and $\tau + d\tau$:

$$p_{ext} d\tau = p_{sur}\left(\tau\right) - p_{sur}\left(\tau + d\tau\right) = -\frac{dp_{sur}}{d\tau} d\tau \tag{6.13}$$

which yields:

$$p_{ext} = p_{sur} = exp\left(-\tau\right) \tag{6.14}$$

In a next step, we formulate the cumulative probability density function for photon extinction and apply Von Neumanns Golden Rule of Sampling (Von Neumann, 1947). The cumulative probability density function is given as:

$$P_{ext}\left(\tau\right) = \int_0^\tau p_{ext}\left(\tau'\right) d\tau' = 1 - exp\left(-\tau\right) \tag{6.15}$$

The advantage of the formulation using the cumulative probability density function is that it is now equally likely that τ falls in the interval $P\left(\tau\right) \in [0, 0.1]$ or $P\left(\tau\right) \in [0.5, 0.6]$. Both cases will occur with 10% probability. By inverting $P_{ext}\left(\tau\right)$, the length of a path cell segment in units of optical thickness is calculated as:

$$\tau\left(P_{ext}\right) = P_{ext}^{-1}\left(\rho\right) = -ln\left(1 - \rho\right) \tag{6.16}$$

where ρ is a random number between 0 and 1. This result represents the random optical thickness that the photon travels before it becomes extinct, i.e., before the photon encounters a process that changes its direction or position. The physical position of location until the randomly generated optical thickness is reached is given by integrating the extinction coefficient over the photon travelling length l in terms of atmospheric cell segments i:

$$\tau = \sum_{cells} l_i \cdot k_{ext,i} \tag{6.17}$$

Two processes can take place at the extinction point. The photon can either be absorbed or scattered. After drawing a random number $\rho \in [0, 1]$, the photon is

scattered if $\rho \leq \frac{\beta_{sca}}{\beta_{ext}}$ and absorbed if $\rho > \frac{\beta_{abs}}{\beta_{ext}}$. After absorption, the photon is vanished and the tracking stops. In case of scattering, the new direction needs to be determined. The approach is to treat scattering effects separately, depending on the scattering source. Scattering by aerosols and clouds is approximated using the Henyey-Greenstein (HG) phase function p_{HG} and scattering by molecules uses the Rayleigh phase function:

$$p_{rayleigh}(\theta) = \frac{3}{4}\left(1 + cos^2\theta\right)$$
$$p_{HG}(\theta) = \frac{1 - g^2}{\left(1 + g^2 - 2g\ cos\theta\right)^{\frac{3}{2}}} \tag{6.18}$$

where g is the asymmetry parameter which describes the distribution of forward and backward scattering. The probability which of the two processes take place is given by $\frac{\beta_{sca,mol}}{\beta_{sca}}$ for Rayleigh scattering and $\frac{\beta_{sca,aer}}{\beta_{sca}}$ for molecular aerosol scattering. Solving eq. (6.18) for the scattering angles θ yields:

$$cos\theta_{Rayleigh} = u - \frac{1}{u}$$
$$\text{with } u = \sqrt[3]{-q + \sqrt{1 - q^2}} \tag{6.19}$$
$$\text{and } q = 4\rho - 2$$

for the Rayleigh scattering angle θ and:

$$\cos\theta_{HG} = \frac{1}{2g}\left[1 + g^2 - \frac{g^2 - 1}{2g\rho - g - 1}\right] \tag{6.20}$$

for the HG scattering angle θ_{HG}. The two examples of interactions given are the only two that are analytically solvable. In addition, there are other processes to be considered, such as real Mie scattering for cloud droplets. In such cases, pre-calculated lookup tables are used to calculate the phase function. The possible photon interactions will be repeated infinitely, until the point, where the photon is either absorbed, leaves the model domain of the TOA or the photon hits the ground. The latter will cause the photon to interact with the ground before the

previously described processes start again. The surface interaction is in our case responsible for the creation of heterogeneous Earth scene radiance. When a photon arrives at the ground, it can either be absorbed or scattered. The exact ratios depend on the ground conditions, in our case specifically on the albedo. For the characterization of the reflection function the $BRDF\left(\theta_i, \phi_i, \theta_0, \phi_0\right)$ (bi-directional reflectance distribution function) is applied, which determines the new direction (θ_0, ϕ_0) as a function of the incidence angles (θ_i, ϕ_i). Here, we assume the surface to be Lambertian, which scales the $BRDF$ by the surface albedo value. Further, MYSTIC uses the concept of the so called photon weights. Instead of letting the photons absorb on the surface at an albedo not equal to 1, each photon is reflected and weighted by the respective probability of reflection, that is, the albedo value. This allows for a faster converging to the results as non of the photons will be lost half way through the atmosphere. The determination of the random direction at the surface is straightforward for the azimuth angle, which is done by drawing a random number between 0° and 360°. For the zenith angle, we have to consider a Lambertian surface which scatters constant radiance in all directions. The Lamber's cosine law states that the radiance observed from a Lambertian surface is proportional to the cosine of the angle θ between the observer line of sight and the surface normal. Including a normalization factor, the probability density is given by

$$p\left(\theta\right) = 2cos\theta \tag{6.21}$$

and the corresponding cumulative probability density:

$$P\left(\theta\right) = \int_0^\theta p\left(\theta'\right) sin\theta' d\theta' = 2 \cdot \int_0^\theta cos\theta' sin\theta' d\theta' \tag{6.22}$$

This summarizes the fundamental principles of the MYSTIC RTM solver. In fact, MYSTIC uses a variety of additional tricks and efficient algorithms to make the calculation of high-resolution TOA spectra with sufficient photon statistics possible. A summary of additional features such as the local or directional estimate

techniques, backward Monte Carlo approach and the ALIS method are described by Mayer (2009) and Emde et al. (2011).
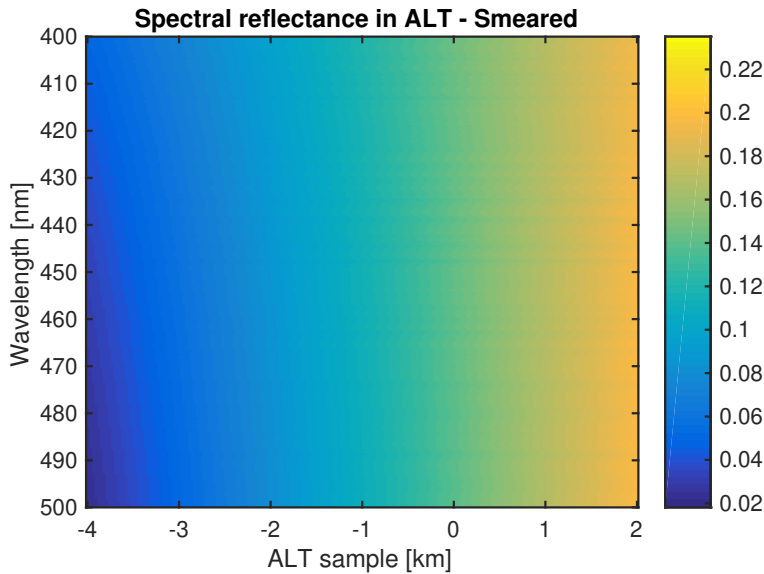
6.3   Simulated heterogeneous Earth scene

In this section, the parameters of the heterogeneous Earth scene radiance are described and further, the generation of the corresponding TOA spectrum received by the instrument is explained. For the RTM simulation and the subsequent NO_2 retrieval, a wavelength range in the visible spectrum from $400-500$ nm was considered. Besides the US-standard atmosphere (Anderson et al., 1986), a polluted NO_2 profile is used. Further, the following cross-section of the atmospheric constituents are used: NO_2 (Vandaele et al., 1998), O_3 (Serdyuchenko et al., 2014), O_4 (Thalman and Volkamer, 2013) and water vapor (Rothman et al., 2010). For the irradiance, the high-resolution extraterrestrial spectrum by Chance and Kurucz (2010) is used. The heterogeneous Earth scene is designed such that it has a sharp transition from low to high albedo in the middle of the scene boundary. The albedo value of the dark part is set to 0.05, while for the bright part, albedo values of 0.3 (scene 1) and 0.8 (scene 2) is considered. This would correspond to an extreme scenario that could represent the transition from vegetation to snow fields in the UV-VIS. The complete scene covers a length of 40 km in ALT and it is assumed that the scene is homogeneous in ACT direction. The size of a single spatial sample is 1 km and the spectral resolution of the spectra is 10 pm. In order to cover different viewing and solar constellations, the following parameter space is used: Instrument viewing angle (umu): $0°, 20°, 60°$, Solar zenith angle (sza): $20°, 40°, 60°, 80°$ and Solar azimuth angle (saa): $0°, 180°$. The simulation was made for every parameter combination for scene 1 and scene 2 (in total 48 cases). The RTE is solved via the MYSTIC Monte Carlo solver as described in section 6.2. The simulations were performed by Claudia Emde (personal correspondence, 2021) and provided for this study.

Figure 6.1a shows a generated scene with $umu = 0°$, $sza = 20°$, $saa = 0°$,
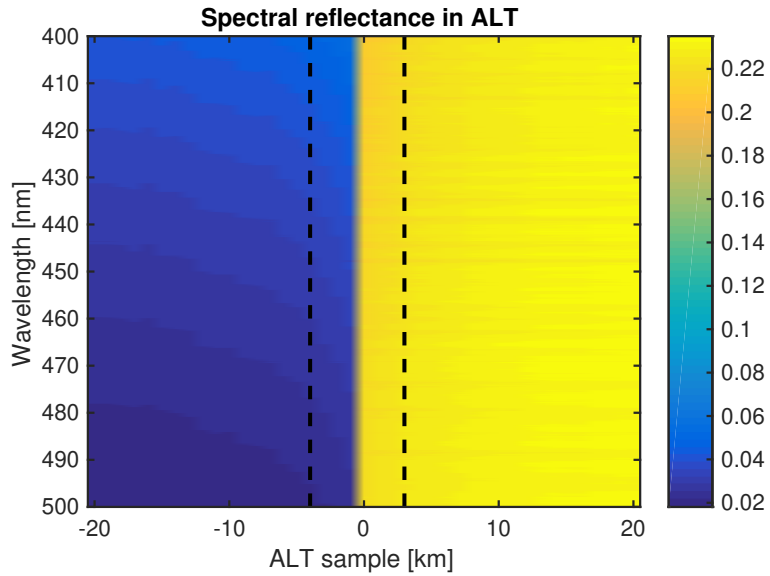
(a) Scene reflectance with albedo step in the center increasing from 0.05 to 0.8.

(b) Scene reflectance after platform motion.

Figure 6.1: (a) Heterogeneous Earth scene reflectance in ALT with a sudden albedo transition in the center. The image was generated for $umu = 0°$, $sza = 20°$, $saa = 0°$, $albedo_{dark} = 0.05$ and $albedo_{bright} = 0.8$. The dashed lines show the respective slit projection onto the scene, corresponding to a width of 7 km. (b) shows the slit input after accounting for the platform motion by means of a boxcar convolution.

$albedo_{dark} = 0.05$ and $albedo_{bright} = 0.8$ in terms of reflectance and spatial ALT direction. The figure also indicates the considered SSD at the region of the albedo step. The SSD of Sentinel-5/UVNS in ALT is 7 km. The smearing of the scene due to the motion of the platform during the integration time is accounted for by convolving the on-ground scene with the motion boxcar of the SSD. This converts the dynamic scan of the scene of the push-broom principle into an effective static scene that will be fed into the instrument. The resulting reflectance of the scene is depicted in fig. 6.1b. The respective remaining scene contrast will serve as an input for the 1DSH and the subsequent instrument propagation of Sentinel-5/UVNS.

6.4 Sentinel-5/UVNS instrument propagation

The propagation of the spectrum and the corresponding heterogeneous slit illumination through the Sentinel-5 instrument was performed using the first-order 1DSH performance model as described in section 4.3. To this end, additional second-order spectrometer effects are neglected. At the end of the propagation through the instrument, one would actually have to convolve the spectrum for each wavelength sampling point with a corresponding individual ISRF. In the 1DSH model, one has to determine a separate TRF for each wavelength, which corresponds to a large computational effort. To reduce the calculation time, only 30 TRFs between 400 and 500nm in equidistant wavelength intervals are calculated. The ISRF for all wavelengths between the TRF interpolation points are determined using a linear interpolation of the ISRFs of two neighboring TRFs according to:

$$ISRF_{\lambda_i}(\lambda) = \epsilon \ ISRF_{\lambda_j}(\lambda) + (1 - \epsilon) \ ISRF_{\lambda_{j+1}}(\lambda) \qquad (6.23)$$

where λ_i is the wavelength sampling data point i of the spectrum between 400 and 500 nm, λ_j is the wavelength at the TRF sampling point j and ϵ is the linear

interpolation factor according to:

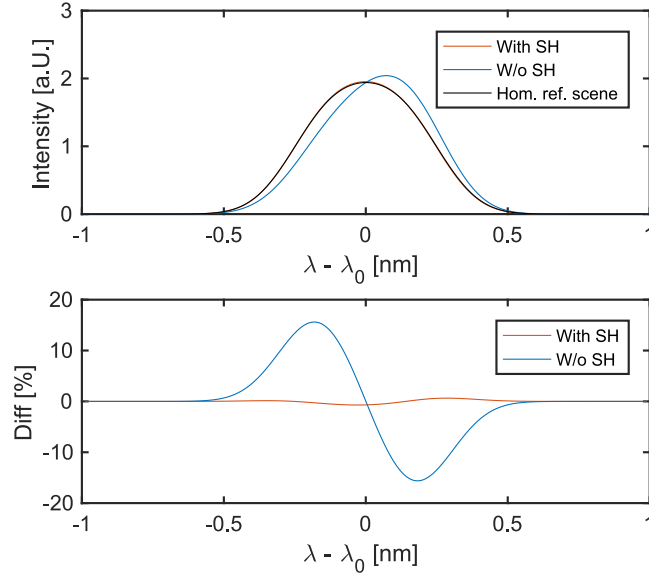$$\epsilon = \frac{\lambda_{j+1} - \lambda_i}{\lambda_{j+1} - \lambda_j} \tag{6.24}$$

Figure 6.2: ISRF shape error comparison for heterogeneous Earth radiance scene 2 generated in MYSTIC for $umu = 0°$, $sza = 20°$, $saa = 0°$, $albedo_{dark} = 0.05$ and $albedo_{bright} = 0.8$ at $\lambda = 400\,\text{nm}$. Without SH, the scene would lead to a maximum ISRF shape error of 15.6% and 0.30% with SH.

In order to obtain a static effective spectrum after the integration time in addition to the static slit illumination, the spectra from the MYSTIC simulation are summed for each ALT sample in the SSD and then averaged ($SSD = 7km$, Spatial ALT sample $= 1km$). Then, each wavelength data point λ_i of the spectrum is multiplied by the corresponding $ISRF_{\lambda_i}$ as calculated in eq. (2.4). Note that each individual $ISRF_{\lambda_i}$ is given over the complete spectrum in normalized form and therefore, this approach is equivalent to a convolution. To quantify the effects of the SH on the spectrum compared to a classical slit, this routine is performed once with and once without SH. Figure 6.2 shows a corresponding ISRF and the associated ISRF shape error with respect to a homogeneous slit illumination at $\lambda = 400\,\text{nm}$. The ISRF errors vary within the spectral band due to the intraband

Figure of merit	With SH		Without SH	
	$\lambda = 400\,\text{nm}$	$\lambda = 500\,\text{nm}$	$\lambda = 400\,\text{nm}$	$\lambda = 500\,\text{nm}$
ISRF shape error [%]	0.3	0.5	15.6	21.0
ISRF FWHM error [%]	0.002	0.003	5.4	9.0
ISRF centroid drift [nm]	$8.5 \cdot 10^{-4}$	$1.4 \cdot 10^{-3}$	$3.5 \cdot 10^{-2}$	$4.7 \cdot 10^{-2}$

Table 6.1: ISRF errors created by the heterogeneous MYSTIC scene with respect to a homogeneous slit illumination. The ISRF figures of merit were calculated at the edge wavelengths of the spectral band at $\lambda = 400\,\text{nm}$ and $\lambda = 500\,\text{nm}$. The differences between the two wavelength points are due to intraband variability of the scene heterogeneity as well as the SH performance.

variability of the heterogeneity of the scene as well as the SH homogenization performance. As discussed in section 4.3, the SH performance is better at shorter wavelengths. Table 6.1 shows the ISRF errors of the edge wavelength points of the spectral band.

In the following, the ISRF stability parameters at instrument level, often also called level-1b data, are to be translated for corresponding errors in the retrieval data of the targeted molecular species (level-2 data). In this study, we focus on NO_2 total column retrieval using the DOAS method.

6.5 Results and Discussion

As discussed in previous sections, the key impact that heterogeneous scenes have on the radiance spectrum is that albedo gradients on the ground produce different spectra recorded by the instrument. The only difference is the change of the response function of the spectrometer, i.e. the ISRF. Here, the ISRF errors discussed previously are translated into radiometric changes in the spectrum, and finally a flow down to the level-2 chemical species retrieval errors is made. Figure 6.3a shows a spectrum for $umu = 0°$, $sza = 20°$, $saa = 0°$, $albedo_{dark} = 0.05$ and $albedo_{bright} = 0.8$, as recorded by the instrument after sensor integration time.

The radiance spectrum was convolved with a representative ISRF of the Sentinel-5/UVNS model, which assumed the same heterogeneous scene but homogeneous slit illumination, representing the ideal case and neglecting any instrument effects due to heterogeneous scenes. This case serves as a reference for the optimal case and thus the ground truth in the following. Figure 6.3b shows the corresponding absolute radiometric differences caused by heterogeneous slit illumination in the radiance spectrum, once for the case with and once without SH. As can be seen, the radiometric deviations from the optimal case are by several magnitudes smaller with a SH. Furthermore, it can be seen that the spectral ISRF error leads to a radiometric error that fluctuates around zero. The peak amplitude of the radiometric deviation depends very much on the exact shape of the absorption line in the spectrum while the ISRF error is almost constant over the wavelength range of the spectrum. This is the reason why spectral performance is usually defined in terms of the stability of the ISRF rather than the radiometric error of the spectrum.

The key question that arises is what impact these radiometric differences have on the level-2 retrieval product. The retrieved SCDs in this section were received by Ka Lok Chan (personal correspondence, 2022). The sensitivity of the DOAS retrieval is very much dependent on the structure of the radiometric deviation of the reference spectrum (see fig. 6.3b). The quality of the retrieval can be described in terms of two parameters. First, the absolute deviation of the retrieved SCD is compared to the reference. A deviation from the reference indicates that there are structures in the radiometric differences that resemble the absorption cross sections of NO_2. Second, the DOAS fitting error is reflected in the fitting error of the polynomial cross sections. If only the fitting error increases while the absolute SCD is similar to the reference, it means that the influence of radiometric differences is similar to random noise. Figures 6.4 and 6.5 show the retrieved SCD values and fit errors for NO_2 for different observation angle ($umu \in [cos(1), cos(0.93), cos(0.5)]$), solar zenith angle ($sza \in [20°, 40°, 60°, 80°]$), solar azimuth angle ($saa \in [0°, 180°]$) and for two different albedo contrasts, ($albedo_{bright} \in [0.3, 0.8]$) respectively for the case with and without SH. In addition, the retrieved SCD values are plotted for the
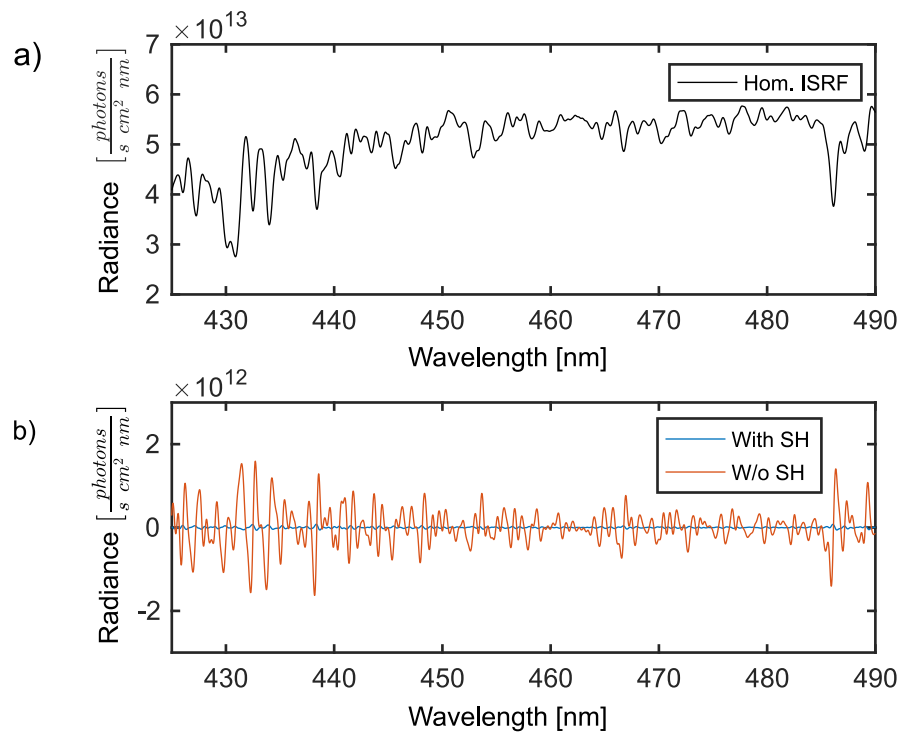
Figure 6.3: (a) Radiance spectrum as seen by the instrument, assuming a homogeneous slit illumination and thus a homogeneous and symmetrical ISRF and neglecting all instrument effects. This spectrum will serve as a reference for comparison. (b) Radiometric differences with respect to an ideal radiance spectrum due to heterogeneous slit illumination caused by heterogeneous ground albedo. Clearly, the radiometric deviation has a lower amplitude when employing a SH.
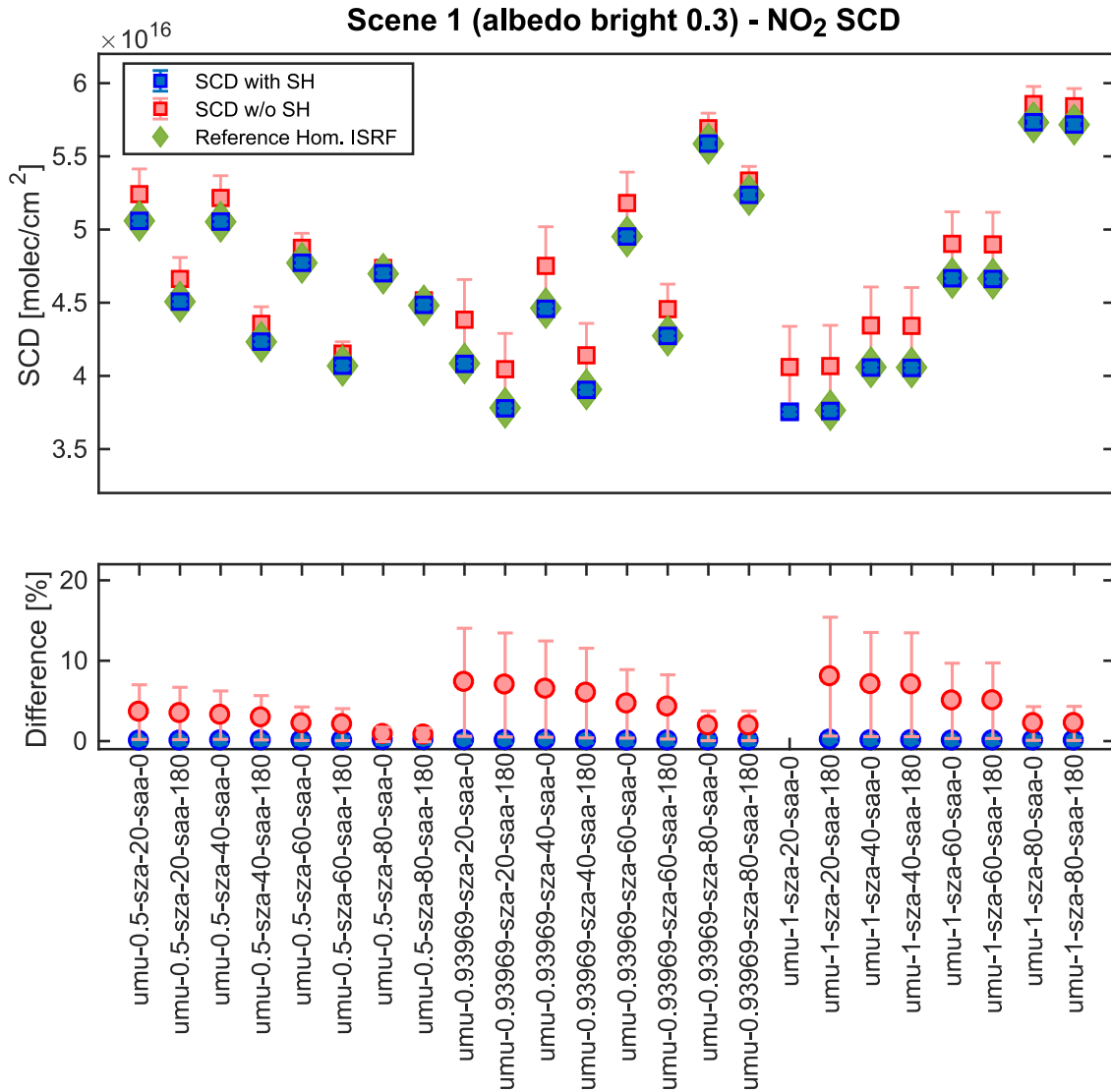
Figure 6.4:   Results of the retrieved SCD for scene 1 ($albedo_{bright} = 0.3$). The figure depicts the respective SCD values for several scene configurations for the case with SH, without SH and the ideal reference case. In addition, the relative difference between the ideal case and the cases with and without SH are calculated. 1/24 data points yields unphysical results which are therefore discarded.

Figure 6.5:   Results of the retrieved SCD for scene 2 ($albedo_{bright} = 0.8$). The figure depicts the respective SCD values for several scene configurations for the case with SH, without SH and the ideal reference case. In addition, the relative difference between the ideal case and the cases with and without SH are calculated. 3/24 data points yields unphysical results which are therefore discarded.
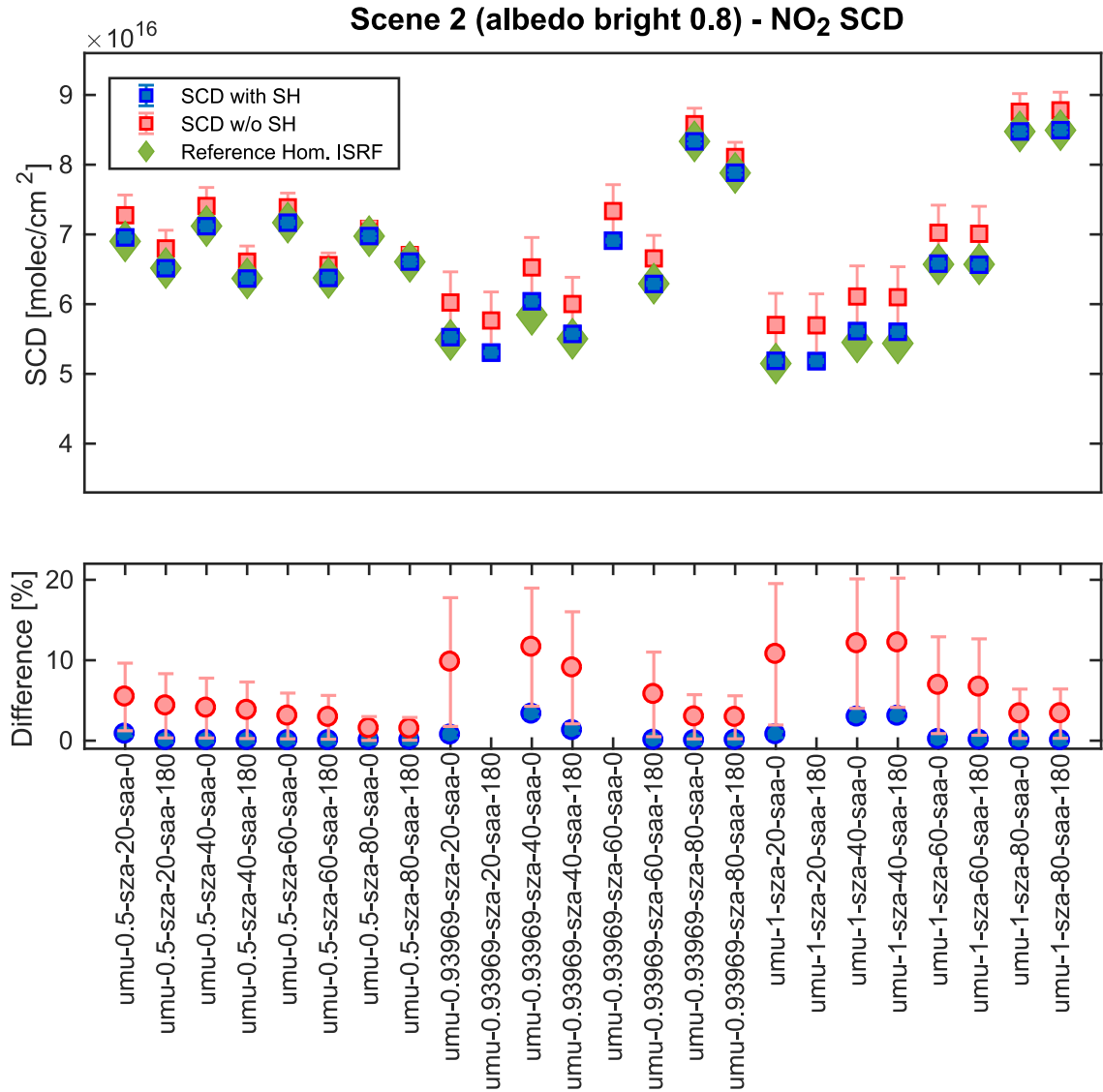
case of a perfectly constant homogeneous ISRF, which serves as a reference. The SCD values without SH yield large deviations from the ideal reference case with errors of $0.76\% - 8\%$ for scene 1 and $1.47\% - 12.17\%$ for scene 2. As expected, the errors generally increase with scene contrast. Further, the fit errors are significant with uncertainties of several percent. Both, the large absolute SCD deviation as well as the large fit errors suggest that the heterogeneous scenes produce random noise on the spectrum as well as structures similar to the absorption lines of NO_2. Contrary, the SCD values for the case with SH are very close to the optimal reference case even for extreme scene contrasts. The SCD errors are in the range of $0.0031\% - 0.13\%$ for scene 1 and $0.0074\% - 3.30\%$ for scene 2. The fit errors have a negligible magnitude. It should be noted that a few scene observation cases (4/48) appear in the retrieval results that provide very large deviation for both cases, with and without SH and are out of the plotting range. As the errors provide unphysical errors of several magnitudes and there are no apparent correlations to effects considered in the study, they are attributed to anomalies in the retrieval process. Monte Carlo simulations are always prone to noise, and since DOAS focuses on the narrow structures, random noise structures can occasionally lead to large uncertainties.

From these results it can be concluded that the SH significantly improves the retrieval SCD accuracy and fit errors under the effect of extreme heterogeneous scenes. It should be emphasized that these scenes represent extreme and probably rare scenarios and therefore limit the results to worst case scenarios. To get a more general overview of the enhanced retrieval accuracy, the method presented here could be extended to larger scene areas as performed by Richter et al. (2018). They investigated the NO_2 retrieval errors due to heterogeneous scenes over the Pacific region in the context of the OMI mission. A similar approach could be made to investigate the enhanced retrieval by using a SH over a region comparable in terms of size.

The homogenization capability of the SH is particularly good in the UV-VIS band due to the interference effects appearing in the SH TRF. For this reason, the

presented NO_2 retrieval in the wavelength channel $400-500\,nm$ is a regime in which the SH provides particularly good improvements for the ISRF stability and consequently also for the retrieved SCD. In other higher wavelength bands, such as SWIR, poorer homogenization of the SH is expected as quantified in section 4.3. The retrieval accuracy is also dependent on the specific trace gas under observation. For example, the retrieval of CO_2 in the SWIR has a completely different setting. In the SWIR wavelength regime, absorption bands are stronger and created by many chemical species including the highly variable H_2O. Aside from the need to use retrieval algorithms other than DOAS, the effects of spectral ISRF distortions on the acquired spectrum have significantly different effects on the retrieval accuracy.

7 Conclusion

In this work, new hardware solutions to mitigate the effects of heterogeneous scenes on the spectral accuracy of spaceborne imaging spectrometers were theoretically investigated and experimentally validated. Heterogeneous scenes lead to non-uniform slit illumination, which in turn leads to a distortion in the ISRF. Since the ISRF provides a direct link between the radiative transfer model of the retrieval algorithm and the spectra measured by the instrument, bias in the ISRF results in immediate uncertainty in the retrieval. The effect on the spectra is a quasi-random radiometric error, often referred to as pseudo-noise. For previous missions, the effect has already been detected and fixed with the help of software solutions. In this case, temporal oversampling of the data is used to draw conclusions about the inhomogeneity of the scene, which are then corrected by software algorithms. While this approach works well in the UV-VIS wavelength range, it fails particularly in the SWIR where the absorption bands are strong and generated by too many chemical species, especially the highly variable H_2O. Future Earth Observation missions, especially those where the ratio of slit footprint to smear distance is close to one, will use a new hardware solution called slit homogenizer. In this thesis, two slit homogenizer concepts are investigated and characterized.

Sentinel-5/UVNS is the first instrument to use a 1D-Slit homogenizer (1DSH) that scrambles the contrast of the scene in along-track direction (ALT). Here, an end-to-end theoretical performance prediction model is presented that for the first time incorporates second-order spectrometer effects such as far-field intensity variations in the spectrometer pupil. The 1DSH homogenizes the scene contrast almost perfectly in shorter wavelengths (UV, VIS). The performance of the 1DSH is limited only by interference effects. In higher wavelength bands (NIR, SWIR), depending on the degree of scene inhomogeneity, these interference effects lead to substantial remaining contrasts. For an artificial 50% stationary slit illumination in the NIR, the theoretical model predicts a remaining ISRF shape error of 8.7%, while no SH would yield a respective shape error of 60.5%. Further, the 1DSH does not

homogenize the across-track direction (ACT) contrast of the scene. In combination with spectrometer smile and keystone, this leads to another unmitigated error source. Another effect is that the spectrometer pupil intensity distribution is scene dependent. An attempt to quantify the resulting spectral ISRF errors due to aberrations in the spectrometer has been presented and quantified in this work. In the context of the Sentinel-5/UVNS mission, the errors are small compared to the near-field homogenization obtained. However, for missions other than Sentinel-5/UVNS, this must be re-evaluated depending on the observed scenes and geometrical spectrometer aberrations of the specific mission.

The upcoming CO_2 monitoring mission (CO2M) will use a fibre-based 2D-Slit homogenizer (2DSH) concept. Fibre-based 2DSH have some advantages over the mirror based 1DSH. First, the scrambling performance is almost perfect, even at arbitrarily high scene contrasts. In the NIR, a 40% stationary slit illumination will induce an ISRF error of $< 0.4\%$, which is a significant improvement compared to the 1DSH. Second, the 2DSH also homogenizes the scenes in ACT, allowing a relaxation of the requirements on keystone and smile of the spectrometer. Especially for the measurement of anthropogenic CO_2 emitted from point sources, it is important to have high precision co-registration schemes between the individual wavelength channels. By design, a fibre-based 2DSH provides a nearly perfect co-registration scheme due to the blind gaps on the detector between individual spatial samples caused by the fibre cladding. One drawback that the 2DSH shares with the 1DSH is the scene dependent variations of the intensity distribution in the spectrometer pupil. This thesis provides a quantification of the induced spectral errors and also suggests a solution to mitigate the effect by suitable fibre bending.

Finally, the example of the 1DSH was used to investigate how the achieved spectral ISRF stabilization over heterogeneous scenes improves the retrieval of the NO_2 slant column density (SCD) in the context of the Sentinel-5/UVNS mission. For two extreme contrast scenes, it was investigated how the accuracy of the absolute NO_2 column density and the induced uncertainty change for the case of a classical slit and for the cases where a 1DSH is used. It was found that the measured

NO_2 SCDs with a classical slit deviated from the reference by $0.76 - 12.7\%$ with additional uncertainty of several percent. Contrary, using a 1DSH reduces the SCD errors to $0.003 - 3.3\%$ with negligible uncertainty.

This thesis can serve as a solid basis for future investigations. An important measurement not included in this work is the experimental validation of the 1DSH performance model, in particular the measurement of the TRFs for different wavelengths. Also, the impact on the retrieval for further chemical species aside from NO_2 could be studied. Of particular interest are measurements in the SWIR region, which is more challenging in terms of absorption lines depth than the UV-VIS band studied in this work. In addition, software corrections are not feasible in this wavelength channel, which makes the technique of the SH even more important. So far, no instrument has been launched that uses a SH. However, if the predicted performance and advantages are confirmed in operational missions, a SH has the potential to become a standard component in any future high-resolution spaceborne imaging spectrometer.

References

Allington-Smith, J., Dunlop, C., Murray, G., and Lemke, U.: End effects in optical fibres, Monthly Notices of the Royal Astronomical Society, 436, doi: 10.1093/mnras/stt1842, 2013.

Amann, S., Duong-Ederer, Q., Haist, T., Sierk, B., Guldimann, B., and Osten, W.: Characterization of fiber-based slit homogenizer devices in the NIR and SWIR, in: International Conference on Space Optics — ICSO 2018, edited by Sodnik, Z., Karafolas, N., and Cugny, B., vol. 11180, pp. 2276 – 2286, International Society for Optics and Photonics, SPIE, doi: 10.1117/12.2536147, 2019.

Anderson, G. P., Clough, S. A., Kneizys, F. X., Chetwynd, J. H., and Shettle, E. P.: AFGL atmospheric constituent profiles (0-120 km)., Tech. Rep. AFGL-TR-86-0110, Air Force Geophys. Lab., 1986.

Avila, G.: FRD and scrambling properties of recent non-circular fibres, in: Ground-based and Airborne Instrumentation for Astronomy IV, edited by McLean, I. S., Ramsay, S. K., and Takami, H., vol. 8446, pp. 1437 – 1443, International Society for Optics and Photonics, SPIE, doi: 10.1117/12.927447, 2012.

Avila, G., Singh, P., and Albertsen, M.: Photometrical scrambling gain and focal ratio degradation in fibers for astronomical instruments, in: Ground-based and Airborne Instrumentation for Astronomy, edited by McLean, I. S. and Iye, M., vol. 6269, pp. 1821 – 1829, International Society for Optics and Photonics, SPIE, doi: 10.1117/12.671417, 2006.

Beirle, S., Lampel, J., Lerot, C., Sihler, H., and Wagner, T.: Parameterizing the instrumental spectral response function and its changes by a super-Gaussian and its derivatives, Atmospheric Measurement Techniques, 10, 581–598, doi: 10.5194/amt-10-581-2017, 2017.

Berlich, R. and Harnisch, B.: Radiometric assessment method for diffraction effects in hyperspectral imagers applied to the earth explorer 8 mission candidate flex,

in: International Conference on Space Optics — ICSO 2014, edited by Sodnik, Z., Cugny, B., and Karafolas, N., vol. 10563, pp. 1475 – 1483, International Society for Optics and Photonics, SPIE, doi: 10.1117/12.2304079, 2017.

Bovensmann, H., Burrows, J. P., Buchwitz, M., Frerick, J., Noël, S., Rozanov, V. V., Chance, K. V., and Goede, A. P. H.: SCIAMACHY: Mission Objectives and Measurement Modes, Journal of the Atmospheric Sciences, 56, 127–150, doi: 10.1175/1520-0469(1999)056⟨0127:SMOAMM⟩2.0.CO;2, 1999.

Burrows, J., Hölzle, E., Goede, A., Visser, H., and Fricke, W.: SCIA-MACHY—scanning imaging absorption spectrometer for atmospheric chartography, Acta Astronautica, 35, 445 – 451, doi: https://doi.org/10.1016/0094-5765(94)00278-T, earth Observation, 1995.

Burrows, J. P., Weber, M., Buchwitz, M., Rozanov, V., Ladstätter-Weißenmayer, A., Richter, A., DeBeek, R., Hoogen, R., Bramstedt, K., Eichmann, K.-U., Eisinger, M., and Perner, D.: The Global Ozone Monitoring Experiment (GOME): Mission Concept and First Scientific Results, Journal of the Atmospheric Sciences, 56, 151–175, doi: 10.1175/1520-0469(1999)056⟨0151:TGOMEG⟩2.0.CO;2, 1999.

Caron, J., Sierk, B., Bezy, J.-L., Loescher, A., and Meijer, Y.: The CarbonSat candidate mission: radiometric and spectral performances over spatially heterogeneous scenes, in: International Conference on Space Optics — ICSO 2014, edited by Sodnik, Z., Cugny, B., and Karafolas, N., vol. 10563, pp. 1019 – 1027, International Society for Optics and Photonics, SPIE, doi: 10.1117/12.2304186, 2017.

Caron, J., Kruizinga, B., and Vink, R.: Slit homogenizers for Earth observation spectrometers: overview on performance, present and future designs, in: International Conference on Space Optics — ICSO 2018, edited by Sodnik, Z., Karafolas, N., and Cugny, B., vol. 11180, pp. 402 – 417, International Society for Optics and Photonics, SPIE, doi: 10.1117/12.2535957, 2019.

Carrasco, E. and Parry, I. R.: A method for determining the focal ratio degradation of optical fibres for astronomy, 271, 1, 1994.

Chance, K. and Kurucz, R.: An improved high-resolution solar reference spectrum for earth's atmosphere measurements in the ultraviolet, visible, and near infrared, 111, 1289–1295, doi: 10.1016/j.jqsrt.2010.01.036, 2010.

Chandrasekhar, S.: Radiative Transfer, Dover Books on Intermediate and Advanced Mathematics, Dover Publications, URL `https://books.google.de/books?id= CK3HDRwCT5YC`, 1960.

Crause, L., Bershady, M., and Buckley, D.: Investigation of focal ratio degradation in optical fibres for astronomical instrumentation - art. no. 70146C, 7014, doi: 10.1117/12.791041, 2008.

Emde, C., Buras-Schnell, R., and Mayer, B.: ALIS: An efficient method to compute high spectral resolution polarized solar radiances using the Monte Carlo approach, Journal of Quantitative Spectroscopy and Radiative Transfer, 112, 1622–1631, doi: 10.1016/j.jqsrt.2011.03.018, 2011.

Emde, C., Buras-Schnell, R., Kylling, A., Mayer, B., Gasteiger, J., Hamann, U., Kylling, J., Richter, B., Pause, C., Dowling, T., and Bugliaro, L.: The libRadtran software package for radiative transfer calculations (version 2.0.1), 9, 1647–1672, doi: 10.5194/gmd-9-1647-2016, 2016.

EOP PIO, E.: Sentinel-5 UVNS Phase A/B1 Reference Spectra, 2011.

ESA, E. M. S. D.: CO2M Mission Requirement Document (MRD), 2020.

Fahey, D. and Hegglin, M.: Twenty Questions and Answers About the Ozone Layer: 2010 Update, Scientific Assessment of Ozone Depletion: 2010, 72 pp., World Meterological Organization, 2011.

Farman, J. C., Gardiner, B. G., and Shanklin, J. D.: Large losses of total ozone

in Antarctica reveal seasonal ClO_x/NO_x interaction, nature, 315, 207–210, doi: 10.1038/315207a0, 1985.

Feger, T., Brucalassi, A., Grupp, F. U., Lang-Bardl, F., Holzwarth, R., Hopp, U., and Bender, R.: A testbed for simultaneous measurement of fiber near and far-field for the evaluation of fiber scrambling properties, in: Ground-based and Airborne Instrumentation for Astronomy IV, edited by McLean, I. S., Ramsay, S. K., and Takami, H., vol. 8446, pp. 1278 – 1291, International Society for Optics and Photonics, SPIE, doi: 10.1117/12.925624, 2012.

Frankenberg, C., Platt, U., and Wagner, T.: Iterative maximum a posteriori (IMAP)-DOAS for retrieval of strongly absorbing trace gases: Model studies for CH_4 and CO_2 retrieval from near infrared spectra of SCIAMACHY onboard EN-VISAT, Atmospheric Chemistry and Physics, 5, 9–22, doi: 10.5194/acp-5-9-2005, 2005.

G, A.: Results on Fiber Characterization at ESO, in: Fiber Optics in Astronomy III, edited by Arribas, S., Mediavilla, E., and Watson, F., vol. 152 of *Astronomical Society of the Pacific Conference Series*, p. 44, 1998.

Gerilowski, K., Tretner, A., Krings, T., Buchwitz, M., Bertagnolio, P., Belemezov, F., Erzinger, J., Burrows, J., and Bovensmann, H.: MAMAP - A new spectrometer system for column-averaged methane and carbon dioxide observations from aircraft: Instrument description and performance analysis, Atmospheric Measurement Techniques, 4, doi: 10.5194/amt-4-215-2011, 2011.

Gloge, D.: Optical Power Flow in Multimode Fibers, Bell System Technical Journal, 51, 1767–1783, doi: https://doi.org/10.1002/j.1538-7305.1972.tb02682.x, 1972.

Goodman, J. W.: Introduction to Fourier optics, vol. 1, 2005.

Goodwin, E. and Wyant, J.: Field guide to interferometric optical testing, Bellingham, Wash. : SPIE Press, 2006.

Gross, H.: Handbook of Optical Systems, Volume 1, Fundamentals of Technical Optics, Handbook of Optical Systems, Volume 1, Fundamentals of Technical Optics, by Herbert Gross, pp. 848. ISBN 3-527-40377-9. Wiley-VCH , April 2005., -1, 2005.

Guldimann, B. and Minoglou, K.: Smart slit assembly for high-resolution spectrometers in space, in: Photonic Instrumentation Engineering III, edited by Soskind, Y. G. and Olson, C., vol. 9754, pp. 57 – 66, International Society for Optics and Photonics, SPIE, URL `https://doi.org/10.1117/12.2209336`, 2016.

Halverson, S., Roy, A., Mahadevan, S., Ramsey, L., Levi, E., Schwab, C., Hearty, F., and MacDonald, N.: An efficient, compact and versatile fiber double scrambler for high precision radial velocity instruments, The Astrophysical Journal, 806, 61, doi: 10.1088/0004-637x/806/1/61, 2015.

Hamidouche, M. and Lichtenberg, G.: In-Flight Retrieval of SCIAMACHY Instrument Spectral Response Function, Remote Sensing, 10, doi: 10.3390/rs10030401, URL `https://www.mdpi.com/2072-4292/10/3/401`, 2018.

Haynes, D., Withford, M., Dawes, J., Lawrence, J., and Haynes, R.: Relative contributions of scattering, diffraction and modal diffusion to focal ratio degradation in optical fibres, Monthly Notices of the Royal Astronomical Society, 414, 253 – 263, doi: 10.1111/j.1365-2966.2011.18385.x, 2011.

Hu, H., Hasekamp, O., Butz, A., Galli, A., Landgraf, J., Aan de Brugh, J., Borsdorff, T., Scheepmaker, R., and Aben, I.: The operational methane retrieval algorithm for TROPOMI, Atmospheric Measurement Techniques, 9, 5423–5440, doi: 10.5194/amt-9-5423-2016, 2016.

Hummel, T., Coatantiec, C., Gnata, X., Lamour, T., Riviere, R., Riviere, C., Krauser, J., Weise, D., and Wenig, M.: Experimental validation of a 2D-slit homogenizer for space based imaging spectrometers, in: International Conference on Space Optics — ICSO 2020, edited by Cugny, B., Sodnik, Z., and Karafolas,

N., vol. 11852, pp. 254 – 262, International Society for Optics and Photonics, SPIE, 2021a.

Hummel, T., Meister, C., Keim, C., Krauser, J., and Wenig, M.: Slit homogenizer introduced performance gain analysis based on the Sentinel-5/UVNS spectrometer, Atmospheric Measurement Techniques, 14, 5459–5472, doi: 10.5194/amt-14-5459-2021, 2021b.

Hummel, T., Coatantiec, C., Gnata, X., Lamour, T., Rivière, R., Meister, C., Stute, A., Krauser, J., Weise, D., and Wenig, M.: A fibre-based 2D-slit homogenizer concept for high-precision space-based spectrometer missions, CEAS Space Journal, doi: 10.1007/s12567-021-00419-8, 2022.

III, B., Crowell, S., Rayner, P., Kumer, J., O'Dell, C., O'Brien, D., Utembe, S., Polonsky, I., Schimel, D., and Lemen, J.: The Potential of the Geostationary Carbon Cycle Observatory (GeoCarb) to Provide Multi-scale Constraints on the Carbon Cycle in the Americas, Frontiers in Environmental Science, 6, doi: 10.3389/fenvs.2018.00109, 2018.

IPCC: Climate Change 2021: The Physical Science Basis. Contribution of Working Group I to the SixthAssessment Report of the Intergovernmental Panel on Climate Change, Cambridge University Press. InPress., 2021.

Irizar, J., Melf, M., Bartsch, P., Koehler, J., Weiss, S., Greinacher, R., Erdmann, M., Kirschner, V., Albinana, A. P., and Martin, D.: Sentinel-5/UVNS, in: International Conference on Space Optics — ICSO 2018, edited by Sodnik, Z., Karafolas, N., and Cugny, B., vol. 11180, pp. 41 – 58, International Society for Optics and Photonics, SPIE, doi: 10.1117/12.2535923, 2019.

Kleipool, Q., Ludewig, A., Babif, L., Bartstra, R. W., Braak, R., Dierssen, W., Dewitte, P.-J., Kenter, P., Landzaat, R., Leloux, J., Loots, E., Meijering, P., van der Plas, E., Rozemeijer, N. C., Schepers, D., Schiavini, D., Smeets, J.,

Vacanti, G., Vonk, F., and Veefkind, P.: Pre-launch calibration results of the TROPOMI payload on-board the Sentinel-5 Precursor satellite, 2018.

Kuhlmann, G., Brunner, D., Broquet, G., and Meijer, Y.: Quantifying CO_2 emissions of a city with the Copernicus Anthropogenic CO_2 Monitoring satellite mission, Atmospheric Measurement Techniques, 13, 6733–6754, doi: 10.5194/amt-13-6733-2020, URL `https://amt.copernicus.org/articles/13/6733/2020/`, 2020.

Landgraf, J., aan de Brugh, J., Scheepmaker, R., Borsdorff, T., Hu, H., Houweling, S., Butz, A., Aben, I., and Hasekamp, O.: Carbon monoxide total column retrievals from TROPOMI shortwave infrared measurements, Atmospheric Measurement Techniques, 9, 4955–4975, doi: 10.5194/amt-9-4955-2016, 2016.

Levelt, P. F., Joiner, J., Tamminen, J., Veefkind, J. P., Bhartia, P. K., Stein Zweers, D. C., Duncan, B. N., Streets, D. G., Eskes, H., van der A, R., McLinden, C., Fioletov, V., Carn, S., de Laat, J., DeLand, M., Marchenko, S., McPeters, R., Ziemke, J., Fu, D., Liu, X., Pickering, K., Apituley, A., González Abad, G., Arola, A., Boersma, F., Chan Miller, C., Chance, K., de Graaf, M., Hakkarainen, J., Hassinen, S., Ialongo, I., Kleipool, Q., Krotkov, N., Li, C., Lamsal, L., Newman, P., Nowlan, C., Suleiman, R., Tilstra, L. G., Torres, O., Wang, H., and Wargan, K.: The Ozone Monitoring Instrument: overview of 14 years in space, Atmospheric Chemistry and Physics, 18, 5699–5745, doi: 10.5194/acp-18-5699-2018, 2018.

Mahajan, V.: Optical Imaging and Aberrations: Ray geometrical optics, no. Teile 1-2 in Optical Imaging and Aberrations, SPIE Optical Engineering Press, URL `https://books.google.de/books?id=Jg1JW4kWD1UC`, 1998.

Mayer, B.: I3RC phase 1 results from the MYSTIC Monte Carlo model, 1999.

Mayer, B.: Radiative transfer in the cloudy atmosphere, European Physical Journal, 1, 75–99, doi: 10.1140/epjconf/e2009-00912-1, 2009.

Meister, C., Bauer, M., Keim, C., and Irizar, J.: Sentinel-5/UVNS instrument: the principle ability of a slit homogenizer to reduce scene contrast for earth observation spectrometer, in: SPIE Proceedings Vol.10423, Sensors, Systems, and Next-Generation Satellites XXI; 104231E, doi: 10.1117/12.2278619, 2017.

Munro, R., Lang, R., Klaes, D., Poli, G., Retscher, C., Lindstrot, R., Huckle, R., Lacan, A., Grzegorski, M., Holdak, A., Kokhanovsky, A., Livschitz, J., and Eisinger, M.: The GOME-2 instrument on the Metop series of satellites: instrument design, calibration, and level 1 data processing - an overview, Atmospheric Measurement Techniques, 9, 1279–1301, doi: 10.5194/amt-9-1279-2016, 2016.

Murphy, J., MacQueen, P., Hill, G., Grupp, F., Kelz, A., Palunase, P., Roth, M., and Fry, A.: Focal Ratio Degradation and Transmission in VIRUS-P Optical Fibers - art. no. 70182T, Proceedings of SPIE - The International Society for Optical Engineering, 7018, doi: 10.1117/12.788411, 2008.

Nivitanont, J., Crowell, S. M. R., O'Dell, C., Burgh, E. B., Mcgarragh, G. R., O'Brien, D., and Moore, B.: Characterizing the Effects of Inhomogeneous Scene Illumination on the Retrieval of Greenhouse Gases from a Geostationary Platform, 2019.

Noël, S., Bramstedt, K., Bovensmann, H., Gerilowski, K., Burrows, J. P., Standfuss, C., Dufour, E., and Veihelmann, B.: Quantification and mitigation of the impact of scene inhomogeneity on Sentinel-4 UVN UV-VIS retrievals, Atmospheric Measurement Techniques, 5, 1319–1331, doi: 10.5194/amt-5-1319-2012, 2012.

Noll, R. J.: Zernike polynomials and atmospheric turbulence∗, J. Opt. Soc. Am., 66, 207–211, doi: 10.1364/JOSA.66.000207, URL `http://www.osapublishing.org/abstract.cfm?URI=josa-66-3-207`, 1976.

Pepe, F., Mayor, M., Rupprecht, G., Avila, G., Ballester, P., Beckers, J.-L., Benz, W., Bertaux, J.-L., Bouchy, F., Buzzoni, B., Cavadore, C., Deiries, S., Dekker, H., Delabre, B., D'Odorico, S., Eckert, W., Fischer, J., Fleury, M., George, M.,

and Penny, A.: HARPS: ESO's coming planet searcher. Chasing exoplanets with the La Silla 3.6-m telescope, The Messenger, 110, 9–14, 2002.

Pepe, F. A., Cristiani, S., Lopez, R. R., Santos, N. C., Amorim, A., Avila, G., Benz, W., Bonifacio, P., Cabral, A., Carvas, P., Cirami, R., Coelho, J., Comari, M., Coretti, I., Caprio, V. D., Dekker, H., Delabre, B., Marcantonio, P. D., D'Odorico, V., Fleury, M., García, R., Linares, J. M. H., Hughes, I., Iwert, O., Lima, J., Lizon, J.-L., Curto, G. L., Lovis, C., Manescau, A., Martins, C., Mégevand, D., Moitinho, A., Molaro, P., Monteiro, M., Monteiro, M., Pasquini, L., Mordasini, C., Queloz, D., Rasilla, J. L., Rebordão, J. M., Tschudi, S. S., Santin, P., Sosnowska, D., Spanò, P., Tenegi, F., Udry, S., Vanzella, E., Viel, M., Osorio, M. R. Z., and Zerbi, F.: ESPRESSO: the Echelle spectrograph for rocky exoplanets and stable spectroscopic observations, in: Ground-based and Airborne Instrumentation for Astronomy III, edited by McLean, I. S., Ramsay, S. K., and Takami, H., vol. 7735, pp. 209 – 217, International Society for Optics and Photonics, SPIE, doi: 10.1117/12.857122, 2010.

Poppett, C. and Allington-Smith, J.: Fibre systems for future astronomy: Anomalous wavelength-temperature effects, Monthly Notices of the Royal Astronomical Society, 379, 143 – 150, doi: 10.1111/j.1365-2966.2007.11922.x, 2007.

Poppett, C. L. and Allington-Smith, J. R.: The dependence of the properties of optical fibres on length, Monthly Notices of the Royal Astronomical Society, 404, 1349–1354, 2010.

Richter, A., Hilboll, A., Sanders, A., Peters, E., and Burrows, J. P.: Inhomogeneous scene effects in OMI NO2 observations, in: EGU General Assembly Conference Abstracts, EGU General Assembly Conference Abstracts, p. 9630, 2018.

Rothman, L., Gordon, I., Barber, R., Dothe, H., Gamache, R., Goldman, A., Perevalov, V., Tashkun, S., and Tennyson, J.: HITEMP, the high-temperature molecular spectroscopic database, 111, 2139–2150, doi: 10.1016/j.jqsrt.2010.05. 001, 2010.

Saleh, B. and Teich, M.: Fundamentals of Photonics, Wiley Series in Pure and Applied Optics, Wiley, URL `https://books.google.de/books?id=rcqKDwAAQBAJ`, 2019.

Schmoll, J., Roth, M., and Laux, U.: Statistical Test of Optical Fibers for Use in PMAS, the Potsdam Multi-Aperture Spectrophotometer, Publications of the Astronomical Society of the Pacific, 115, doi: 10.1086/375696, 2003.

Serdyuchenko, A., Gorshelev, V., Weber, M., Chehade, W., and Burrows, J. P.: High spectral resolution ozone absorption cross-sections – Part 2: Temperature dependence, 7, 625–636, doi: 10.5194/amt-7-625-2014, 2014.

Sierk, B., Bézy, J.-L., Lóscher, A., and Meijer, Y.: The European CO2 Monitoring Mission: observing anthropogenic greenhouse gas emissions from space, in: International Conference on Space Optics — ICSO 2018, edited by Sodnik, Z., Karafolas, N., and Cugny, B., vol. 11180, pp. 237 – 250, International Society for Optics and Photonics, SPIE, doi: 10.1117/12.2535941, 2019.

Sierk, B., Fernandez, V., Bézy, J.-L., Meijer, Y., Durand, Y., Courrèges-Lacoste, G. B., Pachot, C., Löscher, A., Nett, H., Minoglou, K., Boucher, L., Windpassinger, R., Pasquet, A., Serre, D., and te Hennepe, F.: The Copernicus CO2M mission for monitoring anthropogenic carbon dioxide emissions from space, in: International Conference on Space Optics — ICSO 2020, edited by Cugny, B., Sodnik, Z., and Karafolas, N., vol. 11852, pp. 1563 – 1580, International Society for Optics and Photonics, SPIE, 2021.

Somkuti, P., O'Dell, C., McGarragh, G., Crowell, S., Burgh, E., Adamkovics, M., and Crisp, D.: Latest instrument and algorithm developments from the GeoCarb mission, in: EGU General Assembly Conference Abstracts, EGU General Assembly Conference Abstracts, pp. EGU21–8948, 2021.

Spronck, J., Fischer, D., and Kaplan, Z.: Use and Limitations of Single- and Multi-Mode Optical Fibers for Exoplanet Detection, doi: 10.5772/28621, 2012.

Stürmer, J., Stahl, O., Schwab, C., Seifert, W., Quirrenbach, A., Amado, P., Ribas, I., Reiners, A., and Caballero, J.: CARMENES in SPIE 2014. Building a fibre link for CARMENES, vol. 9151, p. 915152, doi: 10.1117/12.2056541, 2014.

Stutz, J. and Platt, U.: Differential Optical Absorption Spectroscopy, Springer Berlin Heidelberg, URL `https://www.ebook.de/de/product/6703866/jochen_stutz_ulrich_platt_u_platt_differential_optical_absorption_spectroscopy.html`, 2008.

Sutherland, A. P., Stuermer, J., Miller, K. R., Seifahrt, A., and Bean, J. L.: Characterizing octagonal and rectangular fibers for MAROON-X, in: Advances in Optical and Mechanical Technologies for Telescopes and Instrumentation II, edited by Navarro, R. and Burge, J. H., vol. 9912, pp. 1582 – 1591, International Society for Optics and Photonics, SPIE, doi: 10.1117/12.2231707, 2016.

Thalman, R. and Volkamer, R.: Temperature dependent absorption cross-sections of O2–O2 collision pairs between 340 and 630 nm and at atmospherically relevant pressure, 15, 15 371, doi: 10.1039/c3cp50968k, 2013.

Thibos, L. N., Applegate, R. A., Schwiegerling, J. T., and and, R. W.: Standards for Reporting the Optical Aberrations of Eyes, in: Vision Science and its Applications, p. SuC1, Optical Society of America, doi: 10.1364/VSIA.2000.SuC1, 2000.

Tyson, R. K.: Principles and Applications of Fourier Optics, 2053-2563, IOP Publishing, Bristol, UK, doi: 10.1088/978-0-750-31056-7, 2014.

UNO: United Nations: Montreal Protocol on Substances that Deplete the Ozone Layer - Adjustments and Amendment, International Legal Materials, 32, 874–887, doi: 10.1017/S0020782900016338, 1993.

van Hees, R. M., Tol, P. J. J., Cadot, S., Krijger, M., Persijn, S. T., van Kempen, T. A., Snel, R., Aben, I., and Hoogeveen: Determination of the TROPOMI-SWIR instrument spectral response function, Atmospheric Measurement Techniques, 11, 3917–3933, doi: 10.5194/amt-11-3917-2018, 2018.

Vandaele, A., Hermans, C., Simon, P., Carleer, M., Colin, R., Fally, S., Mérienne, M., Jenouvrier, A., and Coquart, B.: Measurements of the NO2 absorption cross-section from 42 000 cm-1 to 10 000 cm-1 (238–1000 nm) at 220 K and 294 K, 59, 171–184, doi: 10.1016/s0022-4073(97)00168-4, 1998.

Veefkind, J., Aben, I., McMullan, K., Förster, H., de Vries, J., Otter, G., Claas, J., Eskes, H., de Haan, J., Kleipool, Q., van Weele, M., Hasekamp, O., Hoogeveen, R., Landgraf, J., Snel, R., Tol, P., Ingmann, P., Voors, R., Kruizinga, B., Vink, R., Visser, H., and Levelt, P.: TROPOMI on the ESA Sentinel-5 Precursor: A GMES mission for global observations of the atmospheric composition for climate, air quality and ozone layer applications, Remote Sensing of Environment, 120, 70–83, doi: https://doi.org/10.1016/j.rse.2011.09.027, the Sentinel Missions - New Opportunities for Science, 2012.

Von Neumann, J.: Los Alamos Science, p. 135, Letter from von Neumann to Ulam, 1947.

Voors, R., Dirksen, R., Dobber, M., and Levelt, P.: OMI In-Flight Wavelength Calibration and the Solar Reference Spectrum, 2006a.

Voors, R., Dobber, M., Dirksen, R., and Levelt, P.: Method of calibration to correct for cloud-induced wavelength shifts in the Aura satellite's Ozone Monitoring Instrument, Appl. Opt., 45, 3652–3658, doi: 10.1364/AO.45.003652, 2006b.

Wenig, M., Jähne, B., and Platt, U.: Operator representation as a new differential optical absorption spectroscopy formalism, 44, 3246, doi: 10.1364/ao.44.003246, 2005.

WHO: WHO global air quality guidelines, Air quality and health, Environment, Climate Change and Health, 2021.

Acknowledgements

At this point, I would like to express my deepest gratitude to all the people who have supported, motivated and cheered me up over the past three years, making this work possible for me in the first place.

First and foremost, I would like to thank Prof. Mark Wenig for giving me the opportunity to work in his group and the opportunity to work on an exciting research project with a lot of freedom.

I am grateful to Christian Meister for his continuous support, the many discussions at late hours, sometimes even during your vacations and for giving me the chance to pursue my own ideas which often required a good amount of patience.

Special thanks to Corneli Keim. Her honest feedback and help has been invaluable to me, and I am grateful that she always had an open ear for questions and was always ready to take time for my problems.

Many thanks to Jasper Krauser for making my time at Airbus possible and for always motivating and inspiring me for new topics and ideas.

In addition, I would like to thank other important people who helped me in scientific or organizational matters at many points to the success of the work. These include especially: Dennis Weise, Andreas Stute, Juan Irizar, Xavier Gnata, Pierangelo Marenaci, Rémi Rivière, Tobias Lamour, Claude Coatantiec and Bernd Sierk.

I also would like to thank all other colleagues at Airbus who made the time in the office so pleasant, in particular, Florian Richter, Paul Koschmieder, Markus Trost (breakfast buddy #1), Max Kaiser (breakfast buddy #2), Fabian Müller, Christos Papadopoulos, Max Hörmann and Sebastian Bäumler (special thanks for the thorough proofreading).

But above all, I am deeply grateful to Nairy, Günter, Patrik, Sebastian, Felix, Chiara und Gudrun for their encouragement and support throughout this journey. Thank you for always being there for me.